

Design and Analysis of a Thermolysis Reactor for Scaled-Up  
Copper-Chlorine Hydrogen Production Cycle

by

Tomasz Wajda

A Thesis Submitted in Partial Fulfillment  
of the Requirements for the Degree of Master of Applied Science

in

The Faculty of Engineering and Applied Science, Mechanical Engineering

University of Ontario Institute of Technology

December 2017

© Tomasz Wajda, 2017

---

*Page intentionally left blank.*

---

## ABSTRACT

Alternative hydrogen production methods are being explored with the goal of finding efficient and economical process. The copper-chlorine (Cu-Cl) cycle for hydrogen production has been the focus of the Clean Energy Research Laboratory (CERL) at the University of Ontario Institute of Technology (UOIT). The Cu-Cl cycle has lower thermal energy requirements compared to other methods and utilizes waste heat from power plants and/or some industrial processes. The cycle includes the electrolysis, hydrolysis and thermolysis reaction steps. Decomposition of copper oxychloride ( $\text{CuO}\cdot\text{CuCl}_2$ ) occurs in the thermolysis reactor between  $480^\circ\text{C}$  and  $530^\circ\text{C}$ . A thermolysis reactor design is presented here with the purpose of scaling it up for a pilot plant of the Cu-Cl process. Transient thermal simulations were conducted with 2.0kg of cuprous chloride ( $\text{CuCl}$ ), single and dual heating sources, and 1, 2 and 4  $\text{Wm}^{-2}\text{K}^{-1}$  internal surface convection rates. The dual heater configuration provided the required temperature distribution to allow decomposition to occur. Experimental data with dual heat sources showed that surface temperatures reached  $531^\circ\text{C} \pm 14.0^\circ\text{C}$ . Faster heating was observed with granular  $\text{CuCl}$  in comparison to solidified  $\text{CuCl}$ , because the material was allowed to mix in the reactor while it was melted. Simulations with 10.35kg  $\text{CuCl}$  confirmed adequate surface temperatures for decomposition at low convection rates. Fouling in the phase separation section was observed: XRD analysis showed that the bottom was crystallized  $\text{CuCl}$  while the upper section was a mixture of predominately  $\text{CuCl}_2$  dihydrate and  $\text{CuCl}$ . The vapor production was due to temperatures exceeding  $530^\circ\text{C}$  at the  $\text{CuCl}$ -crucible interface.

---

## ACKNOWLEDGEMENTS

I would like to express my gratitude to Dr Kamiel Gabriel for his guidance and patience in preparation of this thesis. This gratitude is also extended to the entire CERL team for their assistance with experimentation.

Additionally, I am grateful for the support and encouragement from family and friends, in particular my Mom, Dad, Jacob and Elizabeth. Collectively, they kept me focused on completing my research throughout all of the events in the last several months.

Financial support for this research was provided by Canadian Nuclear Laboratories and Ontario Research Fund.

---

# TABLE OF CONTENTS

|  |      |
|--|------|
| Abstract .....   | iii  |
| Acknowledgements .....                                 | iv   |
| Table of Contents .....                                | v    |
| List of Figures .....                                  | viii |
| List of Tables .....                                   | xii  |
| Nomenclature .....                                     | xiii |
| 1 Introduction .....                                   | 1    |
| 1.1 Background and Rationale .....                     | 1    |
| 1.2 Objectives and Scope of Work.....                  | 4    |
| 1.3 Outline of Thesis .....                            | 5    |
| 2 Literature Review.....                               | 6    |
| 2.1 The Cu-Cl Hydrogen Production Cycle .....          | 6    |
| 2.1.1 Hydrogen Production .....                        | 6    |
| 2.1.2 Three-Step Cu-Cl Hydrogen Production Cycle ..... | 7    |
| 2.1.3 Hydrogen Storage.....                            | 8    |
| 2.2 Thermolysis Reactor .....                          | 10   |
| 2.3 Slurry Bubble Column Heat Transfer.....            | 20   |
| 2.4 Thermolysis Cycle Integration .....                | 22   |
| 2.5 Summary .....                                      | 24   |
| 3 Thermolysis Process .....                            | 25   |

---

|       |  |    |
|-------|--|----|
| 3.1   | Thermolysis Reactor Experimental Setup .....         | 25 |
| 3.1.1 | Mechanical Assembly .....                            | 25 |
| 3.1.2 | User Interface and Control Systems .....             | 27 |
| 3.1.3 | Vapor and Pressure Control .....                     | 32 |
| 3.1.4 | Load Cells .....                                     | 33 |
| 3.1.5 | Temperature Control .....                            | 34 |
| 3.1.6 | Reactor Tilt Control .....                           | 36 |
| 3.1.7 | Overview of Thermolysis Reactor Operation .....      | 36 |
| 3.2   | Thermolysis Reactor Mass Flow.....                   | 37 |
| 3.2.1 | Reactor Effluent Gas Scrubber.....                   | 38 |
| 3.2.2 | Gas Entrainment.....                                 | 41 |
| 3.2.3 | Reactor Corrosion .....                              | 47 |
| 3.3   | Procedure for ANSYS Thermal Simulations .....        | 49 |
| 3.3.1 | Simulation Model and Solver Setup.....               | 50 |
| 3.3.2 | Mesh Sensitivity Analysis .....                      | 53 |
| 3.4   | Procedure for Heating a Sample of ISO HEAT 493 ..... | 55 |
| 3.5   | Procedure for Heating a Sample of CuCl.....          | 56 |
| 3.6   | Summary .....  | 57 |
| 4     | Results and Discussion.....                          | 58 |
| 4.1   | Thermal Simulations .....                            | 58 |
| 4.1.1 | Temperature Distribution with 2.0kg CuCl .....       | 59 |
| 4.1.2 | Temperature Distribution with 10.35kg .....          | 66 |

---

---

|       |  |    |
|-------|--|----|
| 4.1.3 | Reduced Temperature Set-Point with 2.0kg CuCl .....              | 71 |
| 4.1.4 | Surface Temperature Distributions and Reduced Reactor Size ..... | 72 |
| 4.1.5 | Summary .....  | 74 |
| 4.2   | Thermolysis Reactor Experiments- ISO-HEAT 493.....               | 74 |
| 4.3   | Thermolysis Reactor Experiments - CuCl .....                     | 78 |
| 4.4   | Scrubber pH Analysis .....                                       | 80 |
| 4.5   | XRD Analysis of Crystalline Formation in Phase Separator .....   | 81 |
| 4.6   | Uncertainty Analysis in Experimental Measurements .....          | 84 |
| 4.7   | Recommendations for Thermolysis Reactor Design.....              | 88 |
| 4.8   | Summary .....  | 90 |
| 5     | Conclusion and Future Work.....                                  | 91 |
| 5.1   | Conclusion .....   | 91 |
| 5.2   | Future Work .....  | 93 |
|       | Appendix 1 – Python Source Code for Temperature Controller.....  | 94 |
|       | References .....   | 96 |

---

## LIST OF FIGURES

|   |    |
|---|----|
| Figure 1: System schematic of the three-step Cu-Cl cycle [7].   | 3  |
| Figure 2: Relative volumetric and gravimetric energy densities [25].  | 10 |
| Figure 3: CuCl melting temperatures and crystalline structures [30].  | 12 |
| Figure 4: Equilibrium vapor pressure of CuCl at various temperatures [34].  | 14 |
| Figure 5: Oxygen partial pressure with varying temperature [35].  | 15 |
| Figure 6: Thermal conductivity of CuCl between 100K and 480K [36].  | 16 |
| Figure 7: Heat capacity of CuCl between 100K and 480K [36].   | 18 |
| Figure 8: Gibbs free energy of $\text{CuO} \cdot \text{CuCl}_2$ / $\text{CuO}$ at varying temperatures [40].                  | 19 |
| Figure 9: Four flow regimes of liquid-gas flows [43].   | 20 |
| Figure 10: Thermolysis reactor experimental setup.  | 26 |
| Figure 11: Thermolysis reactor controls system diagram.   | 27 |
| Figure 12: Assembled thermolysis control panel: VFD (Right), User Interface (Center), and Fusing and Switching Panel (Right). | 28 |
| Figure 13: Hydraulic control system: electric and fluidic interface.  | 29 |
| Figure 14: User interface control schematic.  | 30 |
| Figure 15: Thermal control electrical schematic.  | 31 |
| Figure 16: Heating devices for crucible: band heater assembled on inverted crucible (Left) and Heating tape (Right).          | 35 |
| Figure 17: Key features of the thermolysis reactor.   | 42 |

---

|  |    |
|--|----|
| Figure 18: Drag coefficient for droplets, observed and theoretical [53].   | 45 |
| Figure 19: Terminal velocity and minimum phase separator diameter as a function of particle size, gas flow $0.6\text{m}^3 \text{h}^{-1}$ , liquid flow $0.002\text{m}^3 \text{h}^{-1}$ , $101.3 \text{Pa}$ , $773\text{K}$ . | 46 |
| Figure 20: Three methods for extraction of mist entrained in a gas flow [51].  | 47 |
| Figure 21: Material corrosion resistance ranges dependent on presence of chlorides, and oxidizing or reducing compounds [56].  | 49 |
| Figure 22: Key components in ANSYS transient thermal simulation.   | 50 |
| Figure 23: 2D model of thermolysis reactor used in $2.0\text{kg}$ ANSYS transient thermal simulation. Red triangles indicate simulation temperature probe locations.   | 51 |
| Figure 24: Simulation model mesh configurations at $1.5\text{mm}$ , $2.0\text{mm}$ and $5.0\text{mm}$ element sizes.   | 55 |
| Figure 25: Temperature distribution inside the crucible with a band heater and $2.0 \text{ kg CuCl}$ , $0.5 \text{ W m}^{-2}\text{K}^{-1}$ surface convection coefficient.   | 59 |
| Figure 26: Temperature distribution inside the crucible with a band heater and $2.0 \text{ kg CuCl}$ , $1 \text{ W m}^{-2}\text{K}^{-1}$ surface convection coefficient.   | 60 |
| Figure 27: Temperature distribution inside the crucible with a band heater and $2.0 \text{ kg CuCl}$ , $2 \text{ W m}^{-2}\text{K}^{-1}$ surface convection coefficient.   | 60 |
| Figure 28: Temperature distribution inside the crucible with a band heater and $2.0 \text{ kg CuCl}$ , $4 \text{ W m}^{-2}\text{K}^{-1}$ surface convection coefficient.   | 61 |
| Figure 29: Temperature distribution inside the crucible with dual heaters and $2.0 \text{ kg CuCl}$ , $1 \text{ W m}^{-2}\text{K}^{-1}$ surface convection coefficient.  | 62 |

---

---

|  |    |
|--|----|
| Figure 30: Temperature distribution inside the crucible with dual heaters and 2.0 kg CuCl, 2 W m <sup>-2</sup> K <sup>-1</sup> surface convection coefficient.....   | 62 |
| Figure 31: Temperature distribution inside the crucible with dual heaters and 2.0 kg CuCl, 4 W m <sup>-2</sup> K <sup>-1</sup> surface convection coefficient.....   | 63 |
| Figure 32: Bottom-center temperature at 2.0kg CuCl at 0.5, 1.0, 2.0 and 4.0 Wm <sup>-2</sup> K <sup>-1</sup> .....   | 65 |
| Figure 33: Wall-CuCl top surface interface temperatures with 2.0kg CuCl at 0.5, 1.0, 2.0 and 4.0 Wm <sup>-2</sup> K <sup>-1</sup> . ....                             | 65 |
| Figure 34: Temperature distribution inside the crucible with dual heaters and 10.35 kg CuCl, 1 W m <sup>-2</sup> K <sup>-1</sup> surface convection coefficient..... | 67 |
| Figure 35: Temperature distribution inside the crucible with dual heaters and 10.35 kg CuCl, 2 W m <sup>-2</sup> K <sup>-1</sup> surface convection coefficient..... | 68 |
| Figure 36: Temperature distribution inside the crucible with dual heaters and 10.35 kg CuCl, 4 W m <sup>-2</sup> K <sup>-1</sup> surface convection coefficient..... | 68 |
| Figure 37: Single heater temperature rise, 2.0 kg CuCl.....  | 69 |
| Figure 38: Dual heater temperature rise, 2.0 kg CuCl.....  | 70 |
| Figure 39: Dual heater temperature rise, 10.35 kg CuCl.....  | 70 |
| Figure 40: Modified dual heater with 530°C set point, 2.0kg CuCl 1.0 Wm <sup>-2</sup> K <sup>-1</sup> . ....   | 71 |
| Figure 41: CuCl top surface temperature distribution with 2.0kg. ....  | 72 |
| Figure 42: CuCl top surface temperature distribution with 10.35kg. ....  | 73 |
| Figure 43: Single heater temperature rise, 2.0 kg granular ISO HEAT 493. ....  | 76 |
| Figure 44: Single heater temperature rise, 2.0 kg solid ISO HEAT 493. ....   | 78 |

---

---

|  |    |
|--|----|
| Figure 45: Comparison of surface temperatures between simulations and experimental data, single heat source at surface center, 2.0 kg CuCl. ...    | 79 |
| Figure 46: Comparison of heat up temperature between simulation and experimental data, dual heat source, 2.0 kg CuCl.....                          | 80 |
| Figure 47: Orientation of X-ray source, sample and detector during XRD analysis.....   | 81 |
| Figure 48: XRD analysis of sample from phase separator side wall.....  | 83 |
| Figure 49: XRD analysis of sample from phases separator top cover.....   | 84 |
| Figure 50: Surface and depth temperature gradient used for positional error estimate for thermocouples, from simulated temperature distribution. . | 87 |
| Figure 51: Phase separator interior scaling. ....  | 89 |

---

## LIST OF TABLES

|   |    |
|---|----|
| Table 1: Chemical reaction for each stage of the Cu-Cl hydrogen production cycle. ....  | 2  |
| Table 2: CuCl specific heat capacity as a function of temperature [37].....   | 17 |
| Table 3: Estimated Thermolysis production rates at 100g per day of H <sub>2</sub> .....   | 23 |
| Table 4: Species properties in thermolysis reactor during full conversion.....  | 38 |
| Table 5: Cl <sub>2</sub> gas removed from gas stream. ....  | 41 |
| Table 6: CuCl thermal properties used in thermal simulations. ....  | 52 |
| Table 7: ANSYS solver and model settings. ....  | 52 |
| Table 8: Details of mesh independence study for 1.5mm, 2.0mm, 5.0mm, 7.0mm and 10.0mm maximum element sizes.....                  | 54 |
| Table 9: Simulation convection coefficients and surface temperatures, 2.0kg CuCl, single (1-4) and dual heating (5-7) zones. .... | 64 |
| Table 10: Simulation convection coefficients and surface temperatures, 10.35 kg CuCl, dual heaters (8-10). ....                   | 69 |
| Table 11: Instrument Precision and Bias limits for sensors, ADC modules, and combined sensor and modules.....                     | 86 |

---

## NOMENCLATURE

### Variables and Symbols

|                    |                              |
|--------------------|------------------------------|
| $\alpha$           | reactor tilt angle, degrees  |
| $B$                | bias limit                   |
| $^{\circ}\text{C}$ | temperature, Celsius         |
| $C_D$              | coefficient of drag          |
| $d$                | phase separator diameter, mm |
| $J$                | energy, Joule                |
| $k$                | thermal conductivity, W/mK   |
| $K$                | temperature, Kelvin          |
| $K_a$              | acid dissolution constant    |
| $K_b$              | base dissolution constant    |
| $l$                | length, meters               |
| $m$                | mass, kilograms              |
| $m$                | distance unit, meter         |
| $\text{mol}$       | moles of substance           |
| $P$                | pressure                     |
| $P$                | precision limit              |
| $\text{Pa}$        | pressure unit, Pascal        |
| $\text{pH}$        | hydrogen ion activity        |
| $\text{pOH}$       | hydroxide ion activity       |
| $\rho$             | density                      |
| $Q_g$              | gas flow rate                |
| $R$                | gas constant                 |
| $R$                | function                     |
| $\text{Re}$        | Reynolds number              |

---

|          |                        |
|----------|------------------------|
| T        | temperature            |
| t        | time                   |
| <i>U</i> | uncertainty            |
| V        | volume, m <sup>3</sup> |
| v        | variable in <i>R</i>   |
| W        | power, Watts           |
| Z        | gas compressibility    |

### **Subscripts**

|    |         |
|----|---------|
| aq | Aqueous |
| g  | Gas     |
| s  | Solid   |

### **Chemical compounds**

|                                       |                                       |
|---------------------------------------|---------------------------------------|
| Cl <sub>2</sub>                       | Chlorine                              |
| CO <sub>2</sub>                       | Carbon Dioxide                        |
| CuCl                                  | Copper (I) Chloride, Cuprous Chloride |
| CuCl <sub>2</sub>                     | Copper (II) Chloride, Cupric Chloride |
| CuCl <sub>2</sub> · 2H <sub>2</sub> O | Cupric Chloride Dihydrate             |
| CuO · CuCl <sub>2</sub>               | Copper Oxychloride                    |
| CuO                                   | Copper Oxide                          |
| H <sub>2</sub>                        | Hydrogen                              |
| NaHCO <sub>3</sub>                    | Sodium Hydrogen Carbonate             |
| NaOH                                  | Sodium Hydroxide                      |
| O <sub>2</sub>                        | Oxygen                                |

# 1

## INTRODUCTION

### 1.1 BACKGROUND AND RATIONALE

Hydrogen has numerous applications including an energy alternative for transportation, and a reactant in industrial processes, among others. A hydrogen production method that is both economical and environmentally sustainable is, therefore, of interest to many industrial and commercial sectors. Examples of methods currently used for hydrogen production include steam methane reforming, electrolysis, and coal gasification. Unfortunately, these methods are either costly, or produce unwanted byproducts such as carbon dioxide gas ( $\text{CO}_{2(g)}$ ). Furthermore, significant energy is consumed during the operation of these processes. Since 2007, the Clean Energy Research Laboratory (CERL) at University of Ontario Institute of Technology (UOIT) has been engaged in the research of a hybrid hydrogen production cycle that utilizes copper-chloride salts and waste heat to drive the water-splitting reaction. The copper-chloride (Cu-Cl) cycle is very promising in becoming one of the most economic and environmentally friendly methods to produce hydrogen [1]. To reduce greenhouse gas (GHG) emissions, many governments have enacted measures to tax emissions. These regulations make it possible for the commercial sector to investigate other methods for fuel generation. In cases where the industrial process produces significant waste heat (e.g. a cement plant, nuclear reactor), a hydrogen co-generation plant may be feasible and an economical means to offset regulatory obligations [2] [3]. Recent interest into hydrogen fuel production by aviation and aerospace sectors will

also encourage efficient production methodologies to be implemented commercially [4] [5], while reducing equipment cost. Additionally, global energy consumption is expected to increase 1.4% over the next 20 years [6], and hydrogen will play an important role in keeping GHG emissions under control by becoming a clean alternative to conventional fuels.

The Cu-Cl cycle consists of three main steps: electrolysis, hydrolysis and thermolysis. The chemical reaction and temperature range for the cycle phases are outlined in Table 1. Each step has an optimal temperature range which ensures that complete or near complete reactions occur, with the highest temperature present in the thermolysis reactor. Hydrogen is released in electrolysis from a cuprous chloride (CuCl) and hydrochloric acid solution. The addition of heat is the main reaction driver in the hydrolysis and thermolysis reactors. In the hydrolysis reactor, steam converts dissolved cupric chloride (CuCl<sub>2</sub>) into the double salt copper oxychloride (CuO • CuCl<sub>2</sub>) and hydrogen chloride gas (HCl<sub>(g)</sub>). In the thermolysis reactor CuO • CuCl<sub>2</sub> is broken down into CuCl and oxygen gas (O<sub>2(g)</sub>). The copper compounds in the Cu-Cl cycle may also be found naturally. Anhydrous CuCl has a mineral form of nantokite. Anhydrous CuCl<sub>2</sub> is known as tolbachite and hydrous CuCl<sub>2</sub> (i.e. CuCl<sub>2</sub> • 2H<sub>2</sub>O) is eriochalcite. CuO • CuCl<sub>2</sub> has a mineral form of melanothallite, and it is commonly referred to as copper oxychloride. A process-schematic for the complete Cu-Cl cycle is shown in Figure 1.

Table 1: Chemical reaction for each stage of the Cu-Cl hydrogen production cycle.

| Stage        | Chemical Reaction  | Temperature |
|--------------|--|-------------|
| Electrolysis | $2\text{CuCl}_{(\text{aq})} + 2\text{HCl}_{(\text{aq})} + V \rightarrow 2\text{CuCl}_{2(\text{aq})} + \text{H}_{2(\text{g})}$                        | 30-90°C     |
| Hydrolysis   | $2\text{CuCl}_{2(\text{s})} + \text{H}_2\text{O}_{(\text{g})} + Q \rightarrow \text{CuO} \cdot \text{CuCl}_{2(\text{s})} + 2\text{HCl}_{(\text{g})}$ | 340-400°C   |
| Thermolysis  | $\text{CuO} \cdot \text{CuCl}_{2(\text{s})} + Q \rightarrow 2\text{CuCl}_{(\text{molten})} + \frac{1}{2}\text{O}_{2(\text{g})}$                      | 450-530°C   |

aq – aqueous, s – solid, g – gaseous, V – electrical energy, Q – thermal energy



## 1.2 OBJECTIVES AND SCOPE OF WORK

The objective of this thesis is to examine the temperature distribution of heated mass of CuCl in the thermolysis reactor to determine if conditions are adequate for CuO•CuCl<sub>2</sub> decomposition. The thermolysis reactor was analyzed using results from thermal simulations and experiments. Then, suggestions for future thermolysis reactor designs were included based on the findings.

This work builds on the previous research that was done at CERL by scaling up the reactor for future experiments. Previous experimentation demonstrated that test tubes and small crucibles provided favorable results [8] [9]. The new design of the thermolysis reactor should be capable of supporting hydrogen production at the rate of 100g per day and integrating it into the Cu-Cl cycle workflow.

Design requirements for the thermolysis reactor consider the cycle integration and process control. The main components of the reactor's system are: thermal controller, hydraulic system to enable tilting, and the gas discharge handling system. Each of these components was described in detail within the following sections.

Simulated temperature distribution in the reactor was investigated using a transient thermal model, and then by comparing the results to data obtained from several experiments using a newly designed apparatus. The transient thermal analysis produced a thermal profile for the reactor during start-up and operation at an equilibrium.

Testing in the thermolysis reactor was first conducted with an industrial quenching salt and then with CuCl. The quenching salt was used to verify operability of the experimental setup. It was selected because of the high operating temperature limit (i.e. 899°C), low vapor pressure, and low corrosive properties. Experiments with CuCl were conducted after the thermolysis reactor verification testing was completed.

Synthesis of the  $\text{CuO} \cdot \text{CuCl}_2$  in significant quantities was not yet completed at CERL during the writing of this thesis. Therefore,  $\text{CuO} \cdot \text{CuCl}_2$  decomposition performance of the reactor will not be included in this thesis.

### 1.3 OUTLINE OF THESIS

Chapter 2 contains a literature review of the existing research of the Cu-Cl cycle, and the thermolysis reactor is presented. Summary of the previous research at CERL involving the thermolysis reactor was included to justify the present research. Chapter 2 also reviews cycle integration, which is the major focus for pilot-plant development and thermolysis reactor design.

In Chapter 3, the components of the thermolysis reactor experimental design are described. The chapter addresses the constraints imposed on the design, assumptions, and a detailed description of each subsystem.

Test results from the simulations and experiments are presented in Chapter 4. Single heater and dual heater configurations were examined to quantify temperature distribution in the thermolysis reactor. Additionally, a comparison of simulations and experimental data was explored.

Finally, Chapter 5 contains concluding remarks and suggestions for further studies related to the Cu-Cl cycle and the thermolysis reactor.

# 2

## LITERATURE REVIEW

### 2.1 THE CU-CL HYDROGEN PRODUCTION CYCLE

#### 2.1.1 HYDROGEN PRODUCTION

Numerous thermochemical cycles for hydrogen production have been previously evaluated and considered for coupling to a nuclear reactor or industrial process [10]. Among these hydrogen production methods, the Cu-Cl cycle emerged as one of the lowest technical risk cycles, and provides a progressive opportunity for integration into existing industrial infrastructure. Earlier comparative studies and lab-scale testing conducted at the Argonne National Laboratory (ANL) indicated that the three-step Cu-Cl cycle met the selection criteria; namely: the maximum temperature for the Cu-Cl was the lowest compared to other cycles, and a simulated cycle efficiency of approximately 40% lower heating value (LHV) was attainable [11] [12]. The LHV is the net heat of combustion, which is obtained by subtracting the heat of water vaporization from the gross heating value. These simulations were conducted with an H<sub>2</sub> production rate of 125 MT per day, which required an input of 210 MW of thermal energy and 87.8 MW of electrical energy.

Regarding the environmental impact of existing hydrogen production technologies, Suleman *et al.* compared hydrogen production processes such as natural gas reforming or gasification (i.e. steam methane reforming), electrolysis utilizing electricity from wind and photovoltaics, diaphragm cells, membrane cells, and mercury cells [13]. The life cycle assessment for

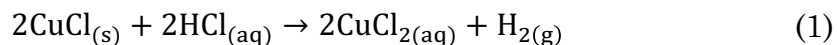
environmental impact as conducted by the Center of Environmental Science of Leiden University (CML) was utilized to evaluate each technology. The study showed that hydrogen production employing renewable sources of energy had the least overall impact on the environment, while natural gas reforming had the highest negative impact. Unfortunately, natural gas reforming is the most common method of hydrogen generation worldwide. Hence, production of large amounts of hydrogen to meet escalating demands of transportation and power industries carries with it significant environmental concerns [14]. Alternative commercial hydrogen production methods are required to curb the environmental impact and to accommodate growing energy needs. A nuclear-coupled Cu-Cl cycle does not require any fossil fuels to produce hydrogen and has extremely low impact on the environment. The simulated production efficiencies also surpass electrolysis-only methods, which are about 24% efficient [3].

Thermal requirements for the Cu-Cl cycle are the lowest compared to other thermochemical hydrogen production cycles. The Cu-Cl cycle has a maximum temperature of approximately 530°C [15]. A low-temperature cycle is more likely to be combined with existing nuclear reactors or can utilize waste heat from industrial source, since equipment with operating temperatures near 530°C is more available in industrial processes. Thus, the path to implementing the Cu-Cl cycle for cogeneration of captive hydrogen (i.e. hydrogen used on site) appears as a leader. In addition, the energy attributed to hydrogen generation will improve the efficacy of the reactor, or industrial process, and reduce overall operating cost.

### 2.1.2 THREE-STEP CU-CL HYDROGEN PRODUCTION CYCLE

The current adaptation of the Cu-Cl cycle consists of three steps: electrolysis, hydrolysis and thermolysis. The net reactant is water and the net products are H<sub>2</sub> and O<sub>2</sub> gases. The CuCl salt is continuously reused in the cycle.

During electrolysis,  $\text{CuCl}_2$  is formed at the anode and  $\text{H}_{2(\text{g})}$  at the cathode. The use of  $\text{CuCl}$  as a catalyst is justified by the reduction of terminal voltages compared to conventional electrolysis. Development in proton exchange membranes (PEM) has improved the efficacy of electrolysis [16] [17]. Using this method,  $\text{H}_{2(\text{g})}$  is readily produced at a current density of approximately  $0.5 \text{ A cm}^{-2}$  and a standard oxidation potential of  $-E^\circ = 0.5 \text{ V}$ , compared to  $1.23\text{V}$  without a PEM [18]. The governing chemical reaction during the electrolysis step is shown in equation (1). Because electricity is required to release  $\text{H}_{2(\text{g})}$ , the Cu-Cl cycle is considered a hybrid thermochemical cycle.



Production of  $\text{CuO} \cdot \text{CuCl}_2$  occurs in the hydrolysis reactor. After elevating the temperature between  $340^\circ\text{C}$  and  $400^\circ\text{C}$ , the aqueous  $\text{CuCl}_2$  is injected into a vessel and converted to  $\text{CuO} \cdot \text{CuCl}_2$  [19]. Ferrandon *et al.* showed that the preferred nozzle design utilizes an ultrasonic injector with a heated gas to reach the required conversion temperature with an ideal  $\text{H}_2\text{O}$  to Cu ratio of 15 to 20 [20].



The final step in the Cu-Cl cycle, thermolysis, is where conversion of  $\text{CuO} \cdot \text{CuCl}_2$  into  $\text{CuCl}$  and  $\text{O}_2$  gas occurs. A detailed description of this step is included in subsequent sections of the literature review.

### 2.1.3 HYDROGEN STORAGE

Storing  $\text{H}_{2(\text{g})}$  is required to utilize the gas in transportation or chemical processing. There are two currently utilized methods of accomplishing this: physical and chemical storage. Physical storage usually requires compression and liquefaction of pure hydrogen. Compression pressures range between 200 and 350 bar. Research into higher compression pressures near 700 bar is

ongoing to increase storage capacity [21]. Structural problems in containment devices become problematic considering the potential hydrogen leakage and explosion.

An alternative to compressed  $H_{2(g)}$  storage is a physisorption process which relies on weak interactions between the hydrogen molecules and a porous material. Carbon materials [22], nanoporous polymers [23] and zeolites (i.e. hydrated aluminosilicates of sodium, potassium, barium and calcium) [24] are examples of these materials. The large surface area that these structures offer can store substantial amounts of  $H_{2(g)}$ . Under nominal conditions the storage capacity is low, in the range 7% by weight at  $-196^{\circ}\text{C}$ . Noticeably, the trouble with this form of storage is the temperature required to sustain the volumetric concentration.

Chemical storage of hydrogen may offer the best balance between safety and storage capacity compared to physical methods. An ideal storage method is fully reversible and allows quick access to the stored hydrogen. Dalebrook *et al.* summarized several metal hydrides as suitable  $H_2$  carriers. Figure 2 compares conventional to solid chemical hydrogen storage methods [21]. Compressed storage offers the highest gravimetric density, but as mentioned earlier, the high compression and volatility of the gas make it difficult to transport and store for long durations. Here, gravimetric density is defined as the ratio of the mass of  $H_{2(g)}$  stored to the mass of the storage mechanism. Similarly, the gravimetric energy density is the ratio of energy of  $H_{2(g)}$  stored to the mass of the storage vessel.

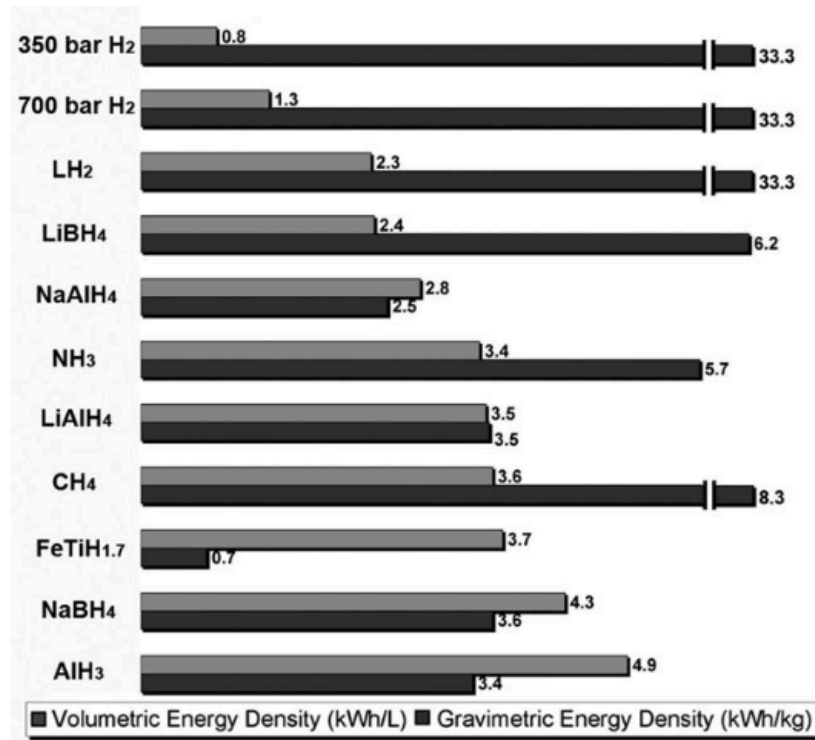


Figure 2: Relative volumetric and gravimetric energy densities [25].

In some cases, liquid storage may be preferred especially if the H<sub>2(g)</sub> is used in a chemical process [26]. The hydrogenation of CO<sub>2</sub> into formic acid is of interest due to its application in fuel cells and industrial processes [27]. Hydrogen released in the Cu-Cl cycle is of very high purity and requires minimal filtering downstream of the electrolysis step, which allows it to be easily stored or used in chemical processes.

## 2.2 THERMOLYSIS REACTOR

The thermolysis reactor serves a single purpose in the Cu-Cl cycle: it decomposes CuO • CuCl<sub>2</sub> into molten CuCl and O<sub>2(g)</sub> with the addition of heat. Thermolysis does, however, require a narrow range of operational characteristics to maintain an efficient decomposition. That is, the process can easily produce unwanted products if the environmental settings deviate from the nominal composition, temperature and pressure ranges.

An alternative method to simulate the thermolysis reaction is by mixing anhydrous  $\text{CuCl}_2$  with  $\text{CuO}$ , which produces molten  $\text{CuCl}$  and oxygen gas [28]. Combining these substances has the same net effect as  $\text{CuO} \cdot \text{CuCl}_2$  decomposition. However, the interfacial heat transfer and subsequent release of gas from the  $\text{CuO} \cdot \text{CuCl}_2$  granules may not be properly simulated since the decomposition reaction will occur throughout the reactor and not just on the  $\text{CuCl} \cdot [\text{CuO} \cdot \text{CuCl}_2]$  interface. Additionally, if an unbalanced mixture – either locally or globally – is processed in the thermolysis reactor, gas species will be released with the discharged oxygen [29]. The probability of creating unwanted gas species is reduced by decomposing  $\text{CuO} \cdot \text{CuCl}_2$  granules into molten  $\text{CuCl}$ . Maintaining an internal thermolysis reactor pressure in the range 1-2 bar was also key in maintaining a forward-driven decomposition process.

The  $\text{CuCl}$  melting profile is shown in Figure 3.  $\text{CuCl}$  has two transitions through crystalline states during heating. The first transition is from solid to solid phase occurs at  $412^\circ\text{C}$ . The structure changes from a cubic to beta-hexagonal. To complete the melt, the beta-hexagonal solids become liquid at  $423^\circ\text{C}$ . The change in microstructures leading up to a 100% liquid phase has a direct impact on the enthalpy per mole, which is reduced as this occurs.

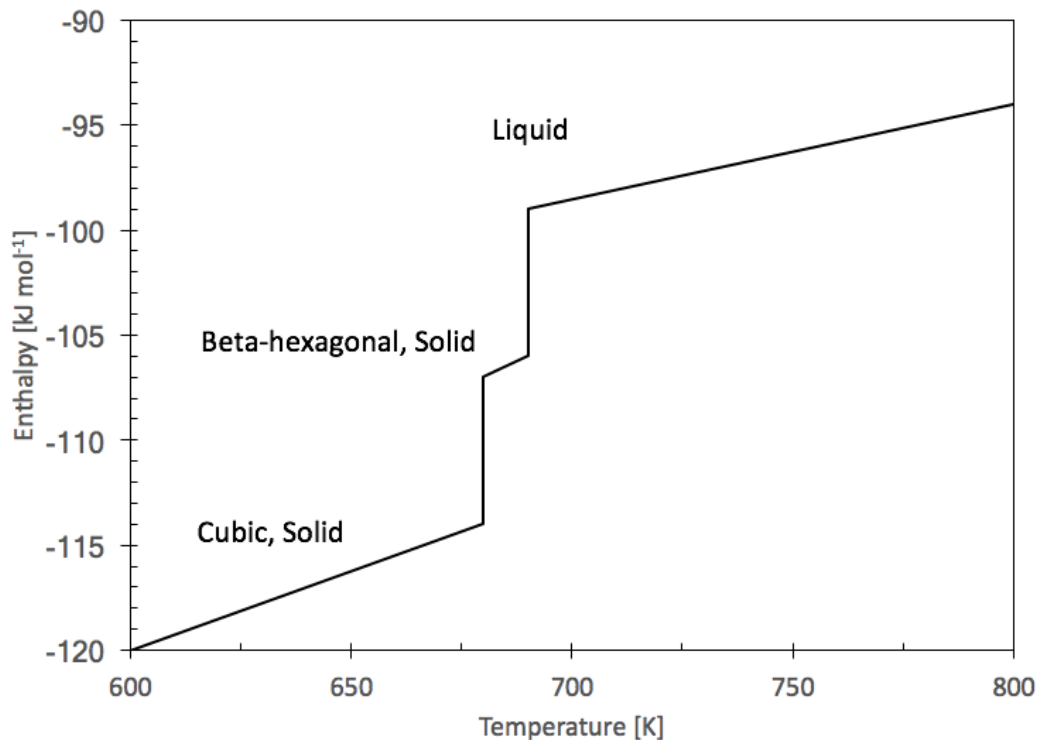
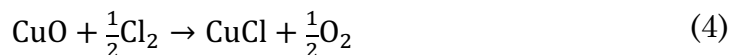


Figure 3: CuCl melting temperatures and crystalline structures [30].

Decomposition of  $\text{CuO} \cdot \text{CuCl}_2$  was proposed to occur in two steps by Serban *et al.* [31]. Serban *et al.* conducted experiments, which utilized a mixture of molar equivalent CuO and  $\text{CuCl}_2$  as the reactants to produce CuCl and  $\text{O}_2$ .



It was observed that completion of the decomposition reaction was limited by the availability of  $\text{CuCl}_2$ , or more likely, the availability of  $\text{Cl}_2$  in the mixture. Serban *et al.* noted that the remaining solid phase was pure CuCl, which inferred that minimal byproducts were formed during decomposition and excess  $\text{Cl}_2$  gas was not identified in the effluent gas stream. If the effluent gases included  $\text{Cl}_2$ , then the pH of the downstream scrubber would have also reduced.

Using mass spectroscopy, Lewis *et al.* determined the rate of decomposition to be 25 minutes at  $530^\circ\text{C}$  [32]. Marin decomposed samples of 50g and 100g at 1.0

bar, and at average temperature ranges of 490°C to 560°C [28]. As the temperature was increased the rate of O<sub>2(g)</sub> production was increased, where up to 95% of the O<sub>2(g)</sub> was released within the first 60 minutes. Decomposition was observed at average CuO•CuCl<sub>2</sub> temperatures as low as 450°C. For a scaled reactor, Abdulrahman proposed a more conservative residence time of 120 minutes to improve the conversion efficiency [33].

Using Dalton's law for partial pressures and the ideal gas law, the pressure of a gas mixture in the thermolysis reactor may be determined as defined by the following equations.

$$P_{\text{Total}} = P_1 + P_2 + \dots + P_n \quad (5)$$

$$P_n = n_n \frac{RT}{V} \quad (6)$$

The species of vapours and gases inside the thermolysis reactor are oxygen, cuprous chloride, copper oxychloride, and possibly cupric chloride and chlorine. These equations can be used to determine the proportionate contribution of each of the species to the overall pressure within the reactor. The two main gases in the system are O<sub>2(g)</sub> and CuCl vapour, because CuO•CuCl<sub>2</sub> quickly decomposes upon entry into the chamber and the remaining substances should only be present in trace amounts.

Ghandehariun *et al.* showed through simulations that molten CuCl will begin to develop a higher partial pressure in the reactor as the temperature is elevated [34]. The CuCl partial pressure is shown to increase exponentially beyond 500°C, as seen in Figure 4. Marin observed a higher loss of CuCl when temperatures exceeded 540°C during CuO•CuCl<sub>2</sub> decomposition at 1.0 bar [28].

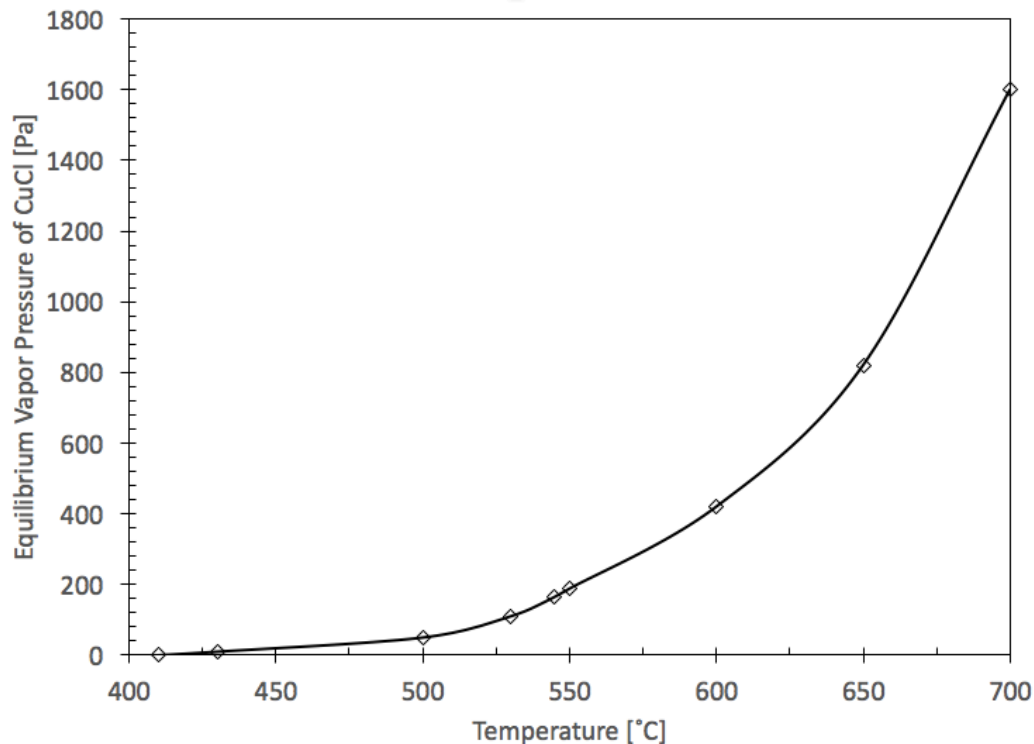


Figure 4: Equilibrium vapor pressure of CuCl at various temperatures [34].

Ghandehariun hypothesized that to suppress the partial pressure of CuCl in the reactor, the reactor pressure should be increased. However, CuCl vapor cannot be completely eliminated otherwise the operational pressure of the reactor would be excessively high, and expensive to construct and operate.

As  $\text{CuO} \cdot \text{CuCl}_2$  decomposes, the oxygen begins to contribute to the partial pressure of the reactor. Daggupati *et al.* considered the role of temperature on the partial pressure of oxygen during the decomposition process [35]. The release of  $\text{O}_2$  begins at temperatures as low as  $380^\circ\text{C}$  but at very low rates. Above  $500^\circ\text{C}$  the decomposition rate is much faster, resulting in a high  $\text{O}_2$  partial pressure. The simulated partial pressures are seen in Figure 5.

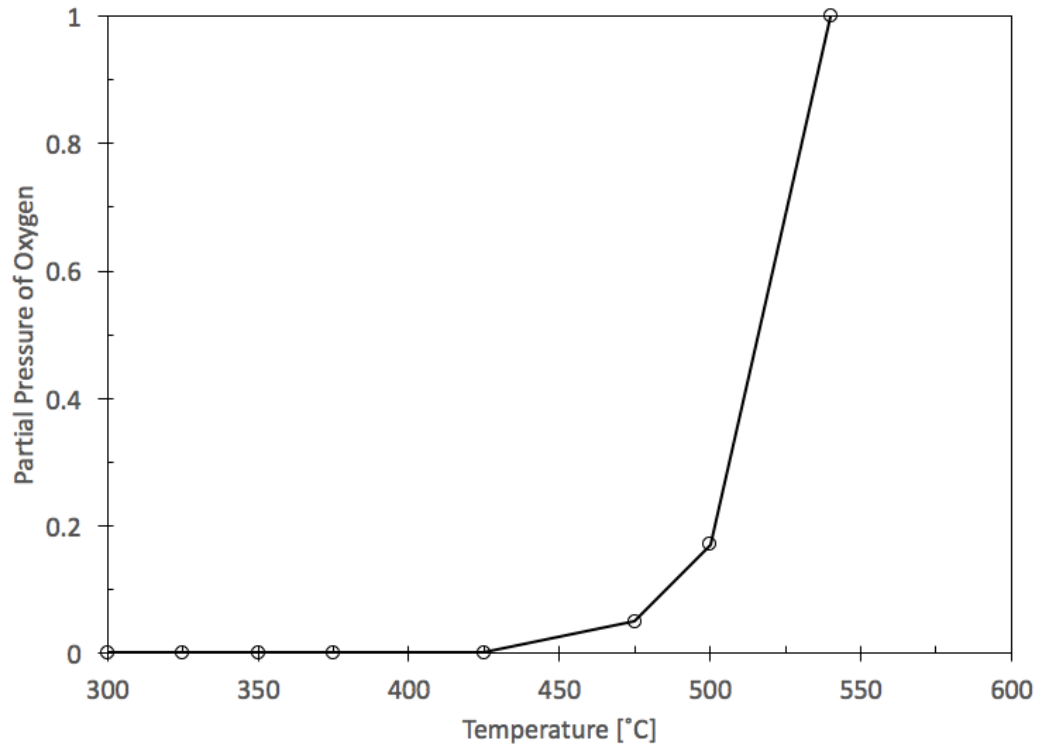


Figure 5: Oxygen partial pressure with varying temperature [35].

A reactor temperature may be optimized to allow the highest oxygen formation without the burden of extreme CuCl vapors. The greatest increase in O<sub>2</sub> production occurs above 500°C, and almost doubles at 525°C in comparison.

Thermal properties of cuprous chloride at various temperatures and pressures, have been previously examined by Slack and Andersson [36]. The thermal conductivity of the CuCl was tested for temperatures between 100K to 480K at pressures ranging from 100 kPa to 2.7 GPa. It was determined experimentally using the transient hot-wire method, whereby a coiled heating wire and thermocouple were pressed between two discs of CuCl. Then, the assembly was heated or cooled and the temperature gradient data was used to determine the thermal conductivity. Figure 6 demonstrates the pressure and temperature effects on thermal conductivity of CuCl.

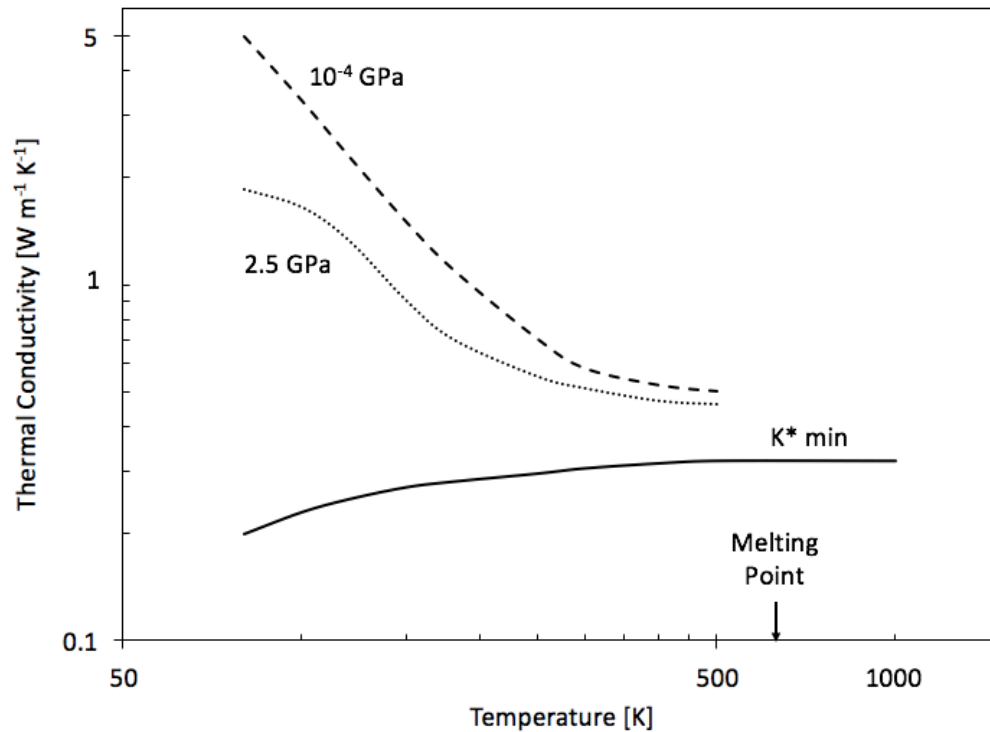


Figure 6: Thermal conductivity of CuCl between 100K and 480K [36].

Figure 6 also shows the theoretical minimum thermal conductivity, which is  $0.313 \text{ Wm}^{-1}\text{K}^{-1}$ . Heat capacity of CuCl was also calculated by Slack and Anderssen [36]. Figure 7 shows the calculated heat capacity per mole of CuCl. The heat capacity quickly increases from 0K to 150K and then begins to plateau at a value near  $50 \text{ Jmol}^{-1}\text{K}^{-1}$ . The recent data of the specific heat capacity in the range of  $25^\circ\text{C}$  to  $527^\circ\text{C}$  is found in Table 2. The two sets of data agree over the overlapping range, however, the data tabulated by Moscow State University is extended well into the liquid region [37].

Table 2: CuCl specific heat capacity as a function of temperature [37].

| Temperature [°C] | Specific Heat Capacity [J mol <sup>-1</sup> °C <sup>-1</sup> ] |
|------------------|--|
| 25               | 52.550   |
| 127              | 52.585   |
| 227              | 55.154   |
| 327              | 58.402   |
| 412              | 61.916-65.005 (Transition)                                     |
| 423              | 79.000-79.000 (Transition)                                     |
| 427              | 63.710   |
| 527              | 63.495   |

Data by Slack and Anderssen [36] demonstrated the effects of temperature and pressure on thermal conductivity and heat capacity. Increasing the temperature of a CuCl sample to the melting point reduced the thermal conductivity, whilst the heat capacity increased and stabilized at a value. Increasing the pressure reduced the thermal conductivity CuCl at the same temperature. The thermal properties of CuCl are needed for a complete understanding of the role of heat transfer within the reactor, as well as simulations.

Thermolysis reactor configurations were explored by Wang *et al.* [38]. Vertical and horizontal reactor orientations may be used for the thermolysis process. Heat is transferred to the CuO • CuCl<sub>2</sub> from the molten CuCl in the reactor. As this occurs, oxygen gas will be formed and is assumed to leave the reactor. However, some gas hold-up is expected and the three-phase mixture will swell. A vertical reactor is more suitable to prevent unreacted material from leaving the system. Furthermore, the residence time in the reactor is longer in a vertical system since the molten salt must flow around the baffle, preventing any aggregated granules from leaving the reactor.

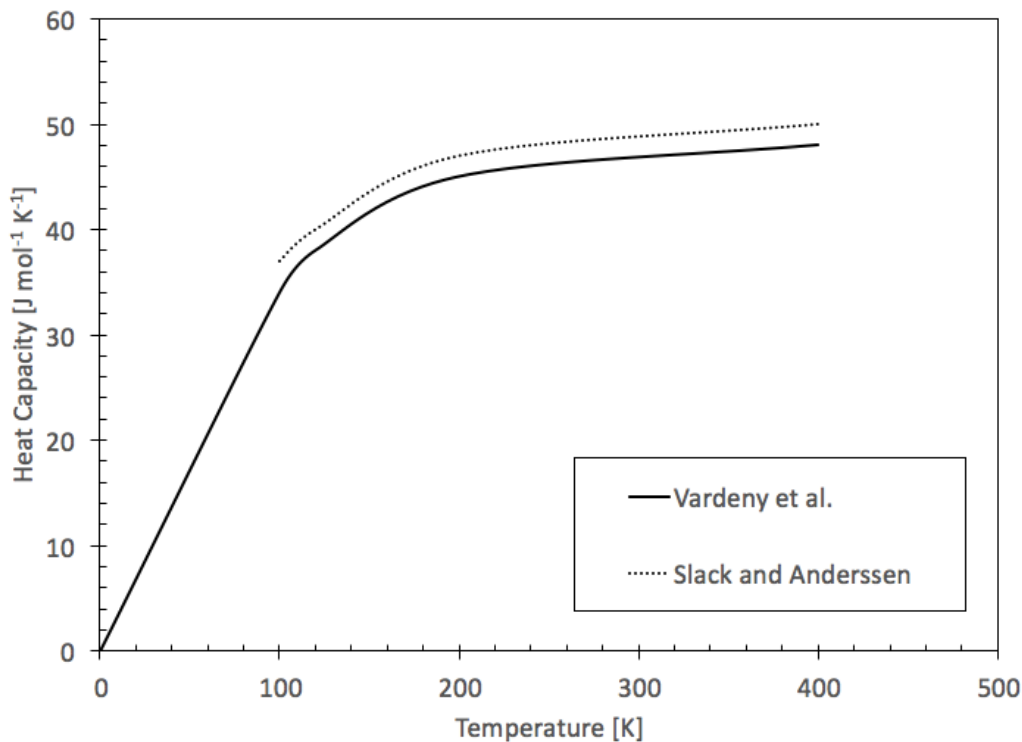


Figure 7: Heat capacity of CuCl between 100K and 480K [36].

Reducing impurities entering the reactor will aid in limiting the production of  $\text{Cl}_2$  gas [39]. Some impurities will enter the reactant stream from the hydrolysis process. That is, unreacted  $\text{CuCl}_2$  will allow the formation of excess  $\text{Cl}_2$  in the thermolysis reactor. The additional  $\text{Cl}_2$  gas leaving the reactor will be sequestered in the scrubber, however it will also hasten the corrosion rate of the apparatus.

Manipulating the temperature and pressure within the reactor allows some control over the impurities formed within the reactor. Naterer *et al.* considered the Gibbs energies associated with the forward decomposition reactions and related them to reactor temperature and pressure combinations [40]. Figure 8 summarizes the decomposition of  $\text{CuO} \cdot \text{CuCl}_2$ , and the formation of  $\text{CuCl}_2$  and  $\text{CuCl}$  as byproducts of excess  $\text{Cl}_2$  in the system.

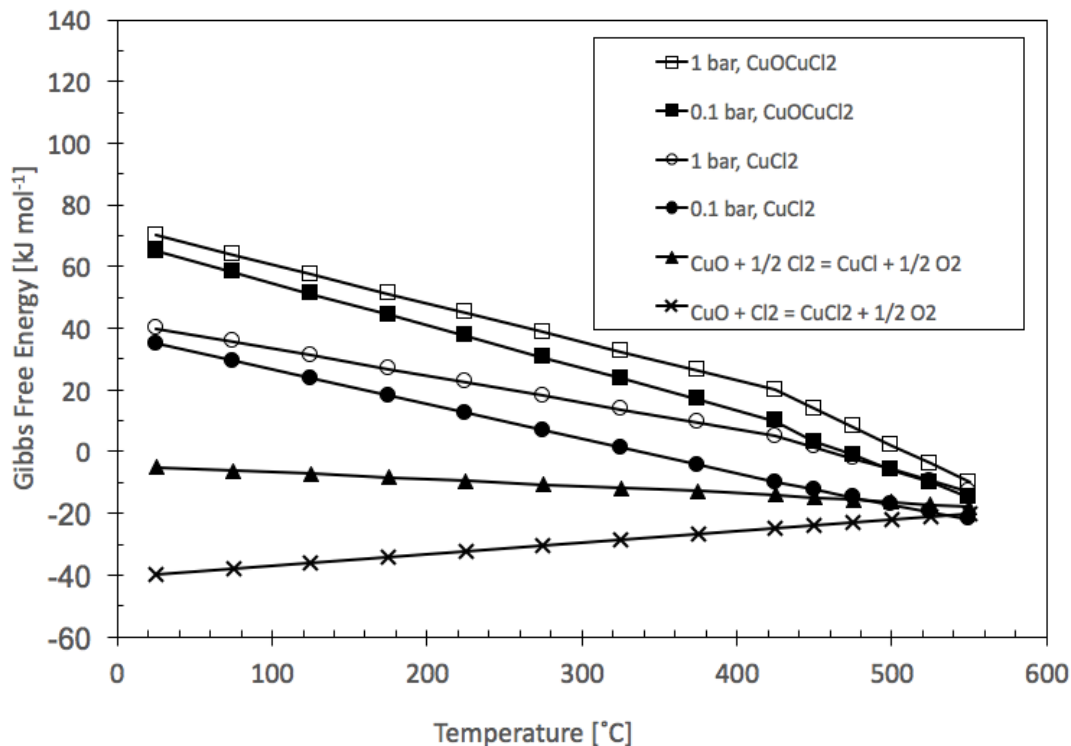


Figure 8: Gibbs free energy of  $\text{CuO} \cdot \text{CuCl}_2$   $\text{CuO}$  at varying temperatures [40].

Generally, the Gibbs energy is reduced for the decomposition of  $\text{CuO} \cdot \text{CuCl}_2$  as the pressure is reduced from 1 bar to 0.1 bar. A Gibbs energy below zero indicates that the decomposition occurs spontaneously. Although the decomposition may occur at a lower temperature with a reduced pressure, it does complicate the process. Mainly, the equipment required to operate at this pressure may be costly and reducing the pressure will increase  $\text{CuCl}$  vapors. Thus, maintaining a pressure of 1 bar in the reactor will be satisfactory to reduce impurities and maintain the forward decomposition reaction.

The heat of reaction for the  $\text{CuO} \cdot \text{CuCl}_2$  decomposition is  $129.2 \text{ kJ/mol}^{-1}$  of  $\text{H}_2$  [32]. Upon reaching the decomposition temperature, this additional heat is required to allow the reaction to proceed. Due to the poor heat transfer rate of  $\text{CuCl}$ , localized decomposition near heated surfaces will, therefore, occur sooner. Abdulrahman *et al.* analyzed the thermal resistance in jacketed reactors and internally heated reactors, and showed that internal heating surfaces may be required depending on the reactor size [41] [42].

### 2.3 SLURRY BUBBLE COLUMN HEAT TRANSFER

When granules of  $\text{CuO} \cdot \text{CuCl}_2$  are added to the molten  $\text{CuCl}$  in the thermolysis reactor a solid-liquid phase interaction is observed. Since the density of  $\text{CuO} \cdot \text{CuCl}_2$  is greater than molten  $\text{CuCl}$  it is expected to sink upon hitting the surface. Once decomposition temperatures are attained,  $\text{O}_2$  gas is released from the granule, which adds another phase to the reactor. A three-phase mixture is commonly referred to as a slurry bubble column. Heat transfer within the slurry bubble column is dependent on the ratio of liquid, solid and gaseous phases.

There are four flow regimes in gas-liquid vertical columns: bubble flow, slug flow, churn flow and annular flow. These regimes are seen in Figure 9. The regime is related to the gas mass flow,  $Q_G$ . The ratio of gas to liquid is typically represented by the void fraction. The four regimes represent an increasing void fraction.

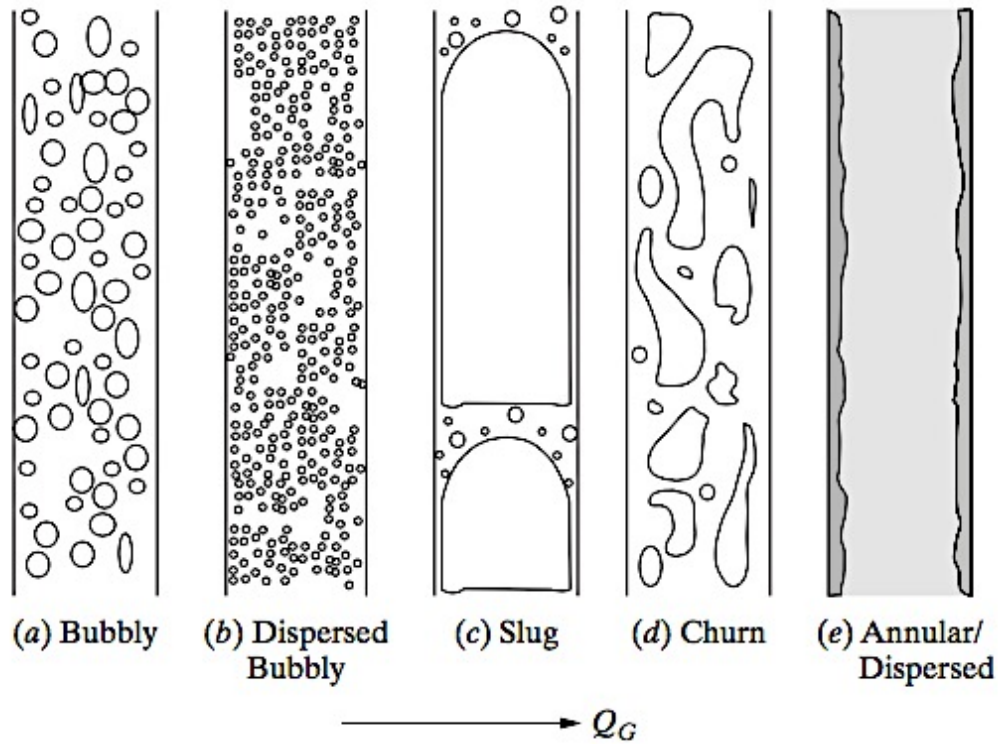


Figure 9: Four flow regimes of liquid-gas flows [43].

Within the bubble flow regime, interactions between discrete bubbles are limited and the liquid phase is continuous. Both, bubbly and dispersed bubbly are included in this regime. Increasing the volumetric flow rate of gas transitions the flow into slug flow, as spherical bubbles turn into Taylor bubbles which are characterized by rounded tops and a diameter nearly equal to the internal diameter of the pipe. Further increase of gas disrupts the Taylor bubbles into an active and mixing churn flow. Finally, an annular flow is formed at high rates of gas flow. The liquid phase is moved upward along the walls of the pipe.

The addition of a solid phase to the mix has an impact on when the four regimes occur. Solid particles are added to break up the gas phase in the slurry bubble column keeping the mixture in the bubble flow domain at higher superficial gas velocities [44]. In the thermolysis reactor, the solid phase will release a gas phase as it descends through the liquid phase. The rate of descent, size of the particle, and rate of gas released all contribute to regime seen in the reactor.

Abdulrahman conducted experiments in a water-helium-alumina slurry bubble column to determine the transition velocity and direct contact heat transfer [45] [46]. The usage of a water-helium-alumina mixture allowed steady state analysis at varying superficial velocities, column heights and solid mixtures. The experiments were conducted with static column heights of 45cm, 55cm and 65cm, at a diameter of 15cm and a gas sparger at the bottom of the column. Transition velocity decreased as the solids concentration was increased from 0% to 10%. Similarly, volumetric heat transfer rate was decreased with increased solids concentration from 0% to 10%.

Wu *et al.* showed that heat transfer was improved with increased superficial gas velocities at 1 bar [47]. However, increasing the column pressure reduced the heat transfer rates. Wu and Al-Dahhan also investigated the effects of up to 25% solids on heat transfer and observed that high solid loads increased

heat transfer in the reactor [48]. Furthermore, small solid loads in the slurry bubble column reactor (i.e. less than 10% solids by volume) had almost identical heat transfer rates to exclusively liquid-gas systems. Both studies also showed that heat transfer near the walls is lower than in center because of reduced interactions between bubbles and the surrounding three phase mixture. Therefore, low solid content may not have a significant effect on heat transfer in the thermolysis reactor. Additionally, the released gas from the decomposition reaction will improve heat transfer within the reactor by agitating the mixture.

#### 2.4 THERMOLYSIS CYCLE INTEGRATION

Process integration is critical to the Cu-Cl cycle, as most stages are being optimized independently at a lab scale. Material and heat flow between neighboring stages requires careful design consideration and analysis. Granules entering the thermolysis reactor are a fine powder, however, aggregation of the particles is possible according to Naterer *et al.* [39]. A varying particle size will have different terminal velocities entering the molten CuCl and fluctuating times to decompose. The height of the reactor will also be dependent on the terminal velocity and buoyancy of the granules. To maintain consistency a maximum size must be established to satisfy the dwell time within the reactor.

Transporting  $\text{CuO} \cdot \text{CuCl}_2$  into the reactor may be done through an auger system or gas-delivery system [38]. The auger system will feed  $\text{CuO} \cdot \text{CuCl}_2$  from above the molten CuCl. This transport method is very robust and easily scalable. As the granules fall into the reactor, however, the effluent  $\text{O}_{2(g)}$  will be moving upward, possibly entraining some solids in the gas phase.

A gas-delivery system proposed by Wang *et al.* may feed the granules in from below the CuCl, if it uses a heated gas [38]. This method enables the CuCl to be vigorously mixed to improve heat transfer – akin to a slurry bubble column

reactor. The additional  $O_{2(g)}$  in the system may interfere with the decomposition process limiting the effectiveness of this method of transport. Startup of the reactor may also be compromised since the delivery mechanism will require all salts to be melted prior to injection of the high temperature – and possibly high pressure –  $O_{2(g)}$ .

A summary of transport rates to and from the thermolysis reactor is shown in Table 3. The quantities shown represent the necessary moles and masses to maintain a production of 100g of  $H_2$  per day. The values were calculated using net stoichiometric equations in the Cu-Cl cycle.

Table 3: Estimated Thermolysis production rates at 100g per day of  $H_2$ .

| <b><math>H_2</math> Production</b> | <b><math>CuO \cdot CuCl_2</math></b> | <b><math>CuCl</math></b> | <b><math>O_2</math></b> |
|------------------------------------|--------------------------------------|--------------------------|-------------------------|
| 49.6 mol                           | 49.6 mol                             | 99.2 mol                 | 24.8 mol                |
| 100 g                              | 10615 g                              | 9822 g                   | 793.7 g                 |

An observation from the transport rates suggests that cycle integration will be arduous when moving very large quantities of  $CuO \cdot CuCl_2$  and  $CuCl$ . Currently, a method of how the reactants will be transported between reactors has not been finalized and several competing systems have been suggested by Naterer *et al.* [39]. Energy consumed during transport may influence the overall cycle efficiency, given that the mass factor between  $H_2$  and  $CuO \cdot CuCl_2$  is approximately 1:100.

Material leaving the thermolysis reactor must run through a heat exchanger to reuse the heat elsewhere in the cycle, thus improving the cycle's energy efficiency. Naterer *et al.* considered an apparatus whereby molten  $CuCl$  is poured through a tube with an annular cooling gas flowing in the upward direction [40]. The main heat transfer mechanism is direct convection. Ideally, the molten salt entering the tube will phase change into a solid and cool further prior to exiting the tube. The length of the tube, diameter, coolant gas

temperature, coolant gas flow rate and CuCl flow rate must be determined experimentally, ultimately to estimate the effective heat transfer rate.

Alternatively, the molten CuCl may be poured into a water bath or HCl solution [39]. Here the dominant heat transfer method is direct conduction into the liquid. Heat may be removed at a much faster rate due to local phase change of the liquid at the interfacial boundary. In this case, the liquid and salt solution may be directly fed into the electrolysis reactor.

## 2.5 SUMMARY

This literature review has shown that existing research is mainly focused on the chemical and physical mechanisms behind each step of the Cu-Cl cycle. Furthermore, the reactor designs were intended for convenient analysis of the decomposition reaction. That is, scaling of the reactor for production or integration to surrounding systems was not a design priority. Suggestions for larger reactors are limited, and as a result of analytical studies.

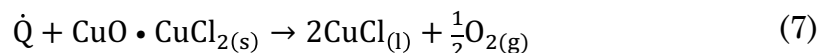
There is a gap in research pertaining to reactor design and its impact on the temperature profile at the surface of the CuCl. The proposed research will strive to bridge this gap by examining the temperature profile of CuCl and show a thermolysis reactor design that will sustain decomposition. In addition, the design of the reactor will include consideration for integration.

# 3

## THERMOLYSIS PROCESS

### 3.1 THERMOLYSIS REACTOR EXPERIMENTAL SETUP

In the final step of the Cu-Cl cycle – the thermolysis reaction –  $\text{CuO} \cdot \text{CuCl}_2$  formed in hydrolysis is broken down into molten CuCl and oxygen gas. The governing net chemical reaction in this step is given below:



There are four key requirements for the thermolysis reactor design. First, this endothermic process relies on a sufficient supply of heat into the reactor to elevate the content's temperature up to approximately 530°C and, therefore, an adequate heating system is needed. Secondly, the vapors formed in the reactor must be evacuated during decomposition. Thirdly, keeping cycle integration in mind, the crucible must transfer – fully or partially – molten CuCl into the quench vessel as decomposition occurs. Lastly, the device must be controlled and monitored remotely from a safe area, preferably outside of the experimental enclosure. Combined, these four items constitute the main requirements of the reactor's safe operation.

#### 3.1.1 MECHANICAL ASSEMBLY

The assembled experimental thermolysis reactor is seen in Figure 10. The design was centered around a previously fabricated crucible made of 316L stainless steel, which was utilized as the thermolysis reactor. A MiniTec modular support frame was assembled for all components of the reactor

system, because it allowed for quick frame modification, and versatile mounting of sensors and equipment.

The thermolysis reactor was mounted on a pivoting frame, which allowed the crucible to be adjusted to keep the tip of the spout in alignment with the tilting axis during pouring. A hydraulic cylinder was attached below this assembly and attached to a reaction beam on the stationary support structure. The apparatus shown in Figure 10 was assembled in a Plexiglas® enclosure to contain and vent all fumes generated whilst conducting experiments.

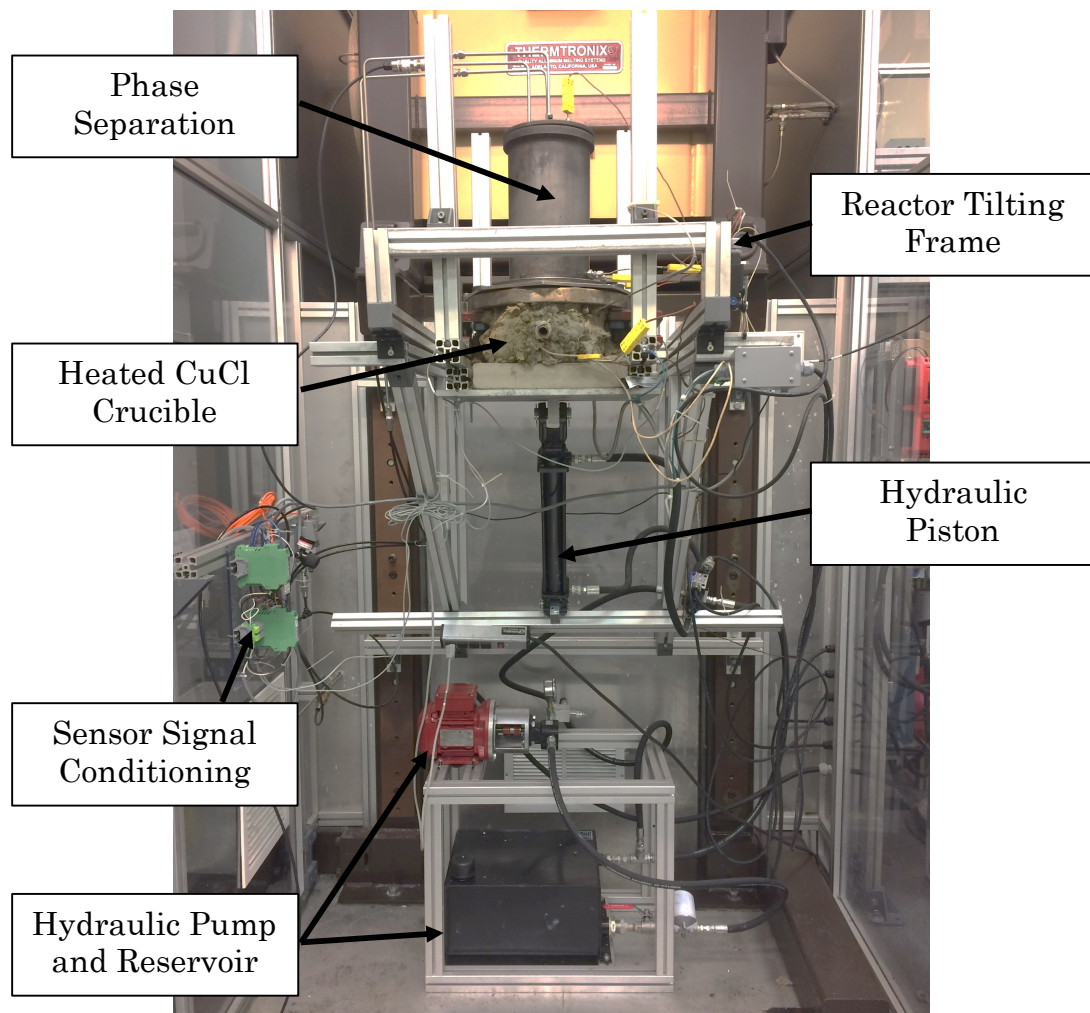


Figure 10: Thermolysis reactor experimental setup.

The vertical position of the apparatus was adjusted to place a quench vessel under the spout of the thermolysis reactor in order to examine pouring dynamics, heat transfer of the molten droplets falling through the air and phase interactions as the droplets hit the water surface. These topics, however, are beyond the scope of this work.

### 3.1.2 USER INTERFACE AND CONTROL SYSTEMS

An accessible user interface was constructed to control and automate the reactor subsystems. The panel included vapor control, thermal control and transfer hydraulics (i.e. tilting assembly) control subsystems. A system diagram for the thermolysis reactor is shown in Figure 11.

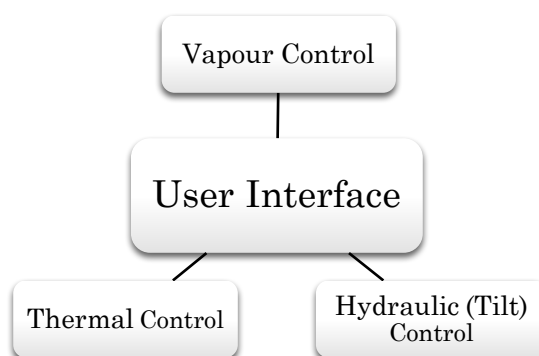


Figure 11: Thermolysis reactor controls system diagram.

The assembled user interface and distribution panel is shown in Figure 12, which was located outside of the thermolysis reactor enclosure. The reactor could then be easily operated from a safe location.

An electrical distribution panel provided the necessary protection to operate the thermolysis reactor. From this panel, the hydraulic pump speed was set on the variable frequency drive, the crucible temperature set-point was modified and the tilting mechanics was activated manually. The electrical distribution provided additional safety, and relay logic to prevent concurrent failures. The panel allowed the system to be controlled manually by default or proceed to automatic control.

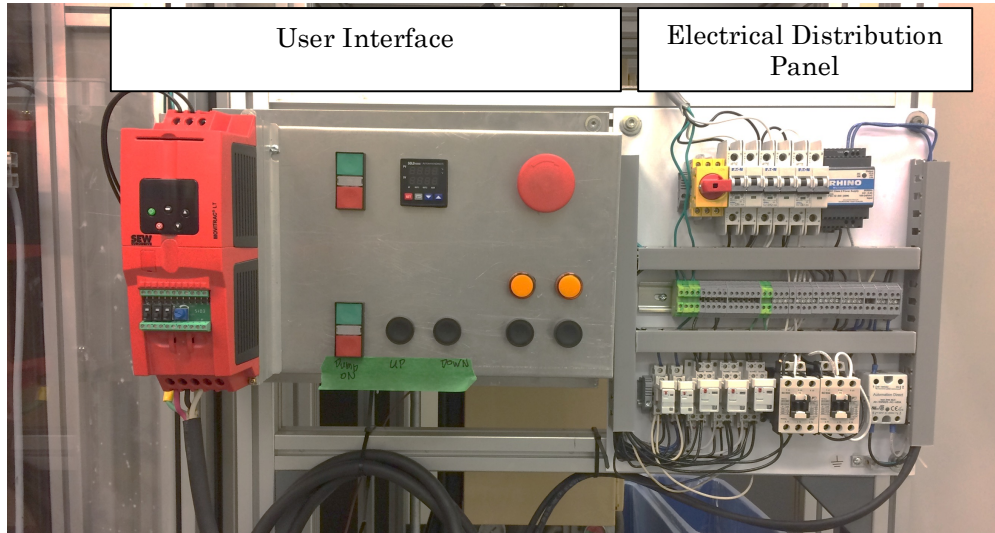


Figure 12: Assembled thermolysis control panel: VFD (Right), User Interface (Center), and Fusing and Switching Panel (Right).

A combined electrical and hydraulic schematic is shown in Figure 13-15. Each subsystem was fused individually to maintain power to the user interface or remote monitoring system in the event of a failure. The most likely components to fail were the band and tape heater due to the high operating temperatures of the heating wires. A failed heater may either become an open-circuit or short-circuit to the housing. Failing open circuit is the safe failure mode of the device and will be identified by a declining reactor temperature even though the temperature controller is requesting heat. In this case, the operator or monitoring software would notice this event and turn off the supply power to the heater.

On the other hand, a short-circuit failure will activate the thermal-magnetic overload in the circuit breakers upon reaching the threshold current. The mounting frame closest to the heaters is grounded for this reason. Without the grounded frame the entire apparatus may become energized.

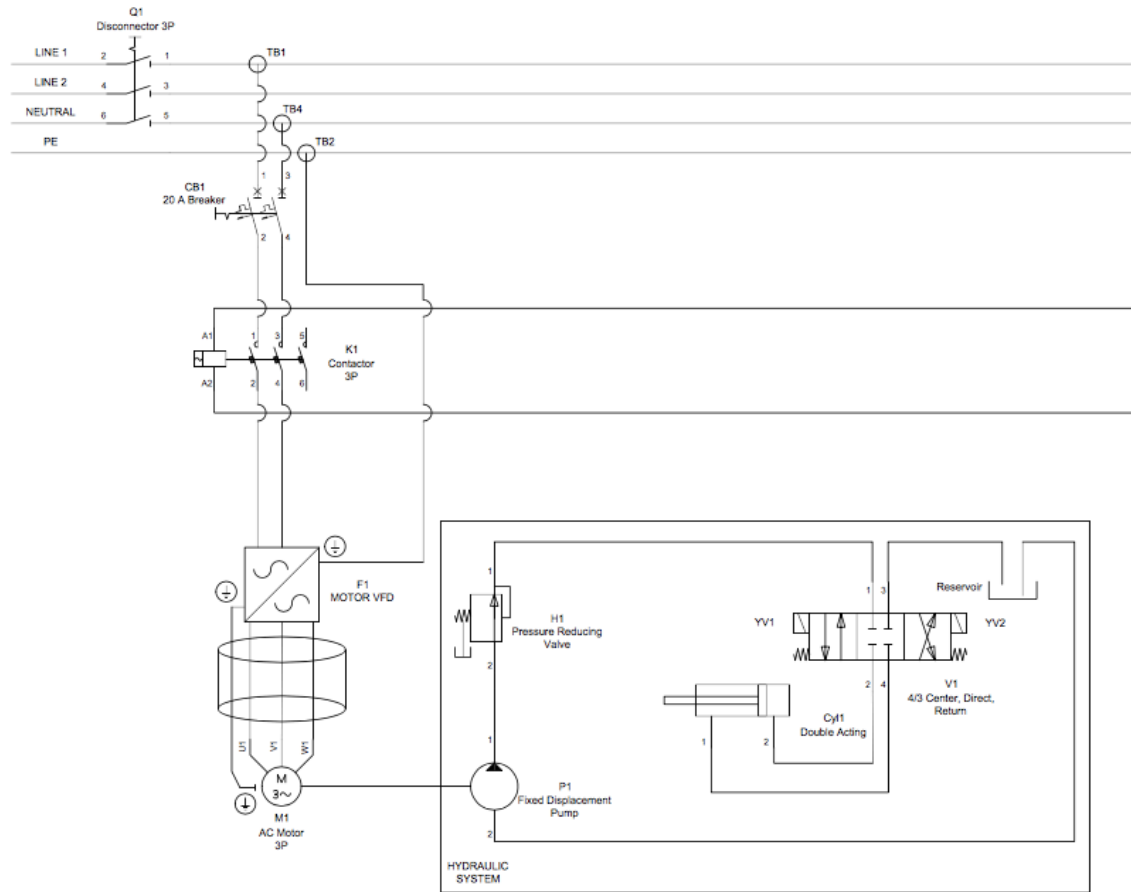


Figure 13: Hydraulic control system: electric and fluidic interface.

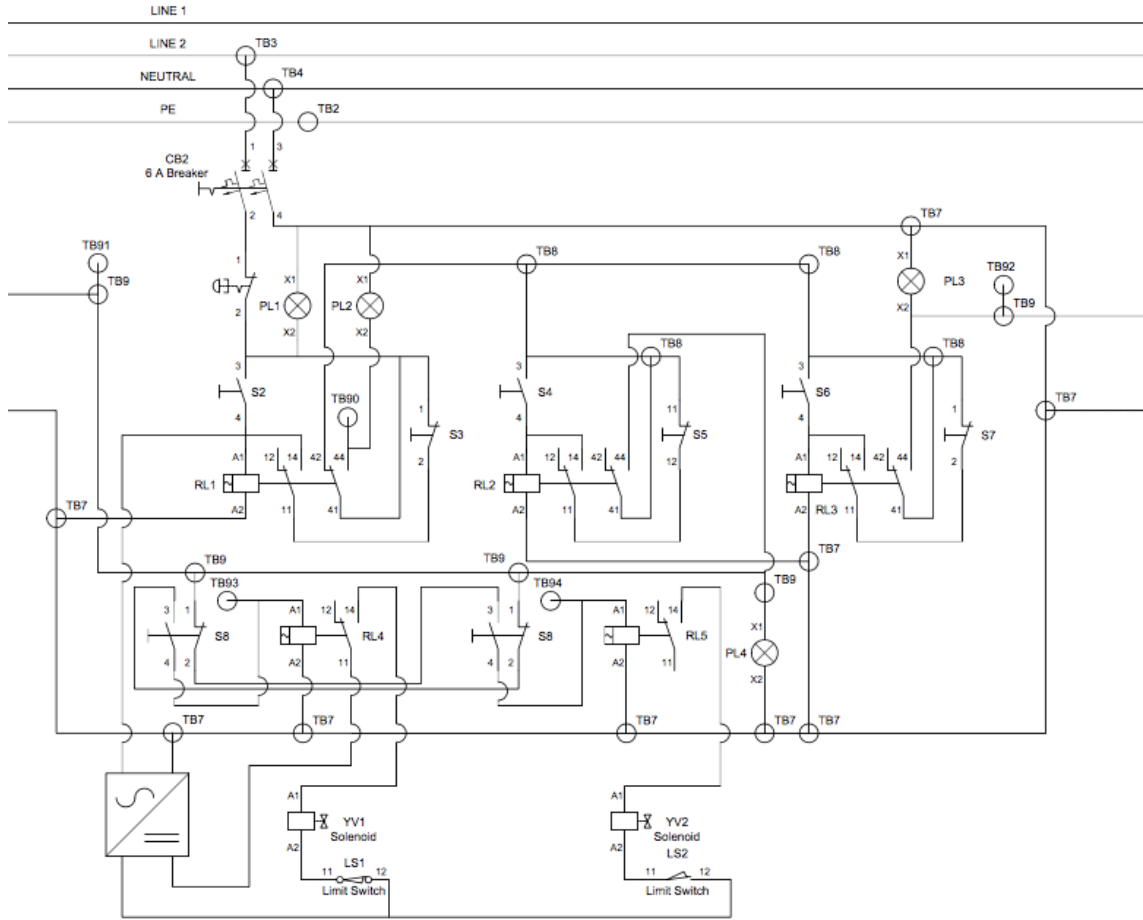


Figure 14: User interface control schematic.

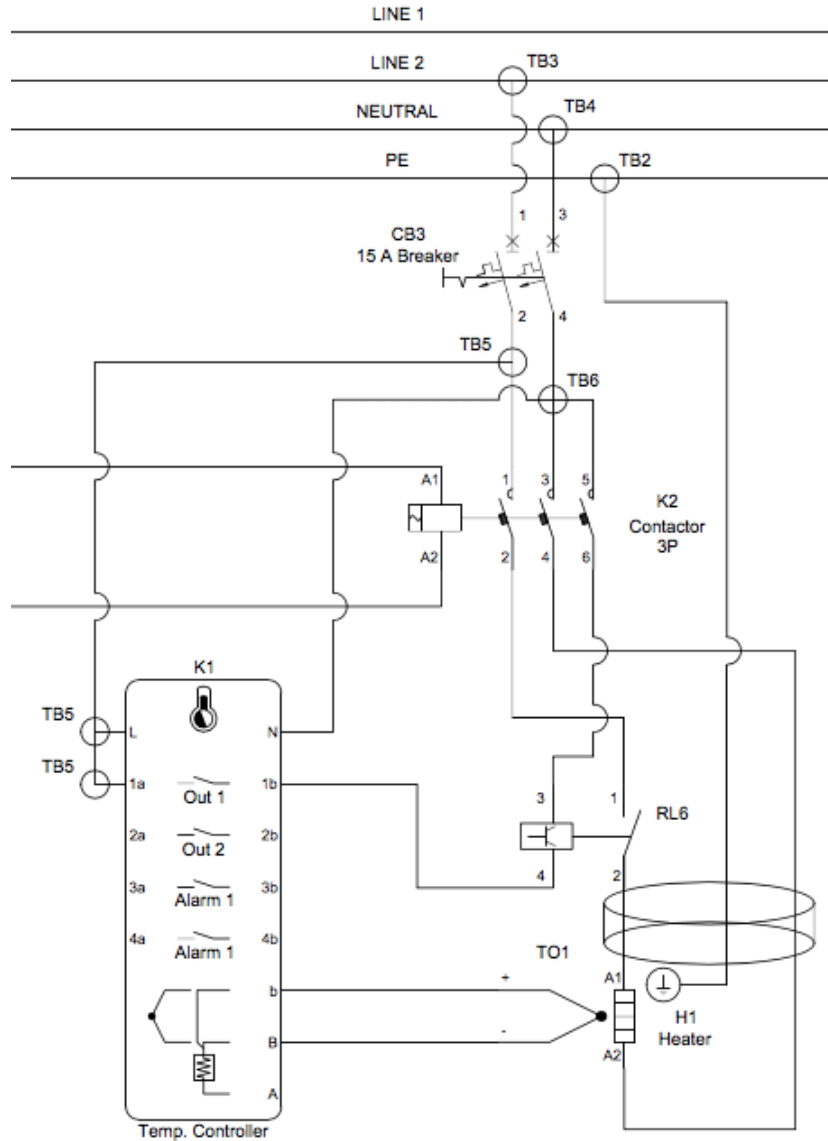


Figure 15: Thermal control electrical schematic.

A computer interface to the user interface was developed with a Universal Serial Bus (USB) connection. This enabled data logging and expansion for future centralized control of the thermal, tilt and vapor control systems. During the operation of the apparatus, all sensors were monitored by a National Instruments data acquisition (National Instruments CompactDAQ) with NI9203, NI9211 and NI9215 inserts. Data was captured and recorded at one minute intervals. A USB to RS485 bridge was used to monitor the state of

the thermal controller. This interface was logged by a Python script, that also recorded temperature data every minute. The temperature controller used a MODBUS/RTU communication layer to handle all data requests to read and write to individual registers. A timestamp at each reading synchronized the collected set point temperature and process temperatures from the DAQ and Python script.

Provisions for automated control from a central location were included in the electrical design. A remote system could modify all parameters on the thermal control unit, dispense the contents into the quench cell and vary the internal thermolysis reactor pressure. This feature will be important when expanding the hydrogen production cycle beyond the lab-scale, since material must be autonomously conveyed between stages. Replacing the current data logging system with a programmable logic controller (PLC) will complete the transition to a fully automated thermolysis process.

### 3.1.3 VAPOR AND PRESSURE CONTROL

The vapor system removes all gases from the reactor by utilizing a nozzle vacuum-injector (McMaster-Carr 41605K14). This device can produce a vacuum of 685.8 Torr, with a maximum flow rate of  $3.74 \text{ m}^3\text{h}^{-1}$ . Using this device adds two benefits to the thermolysis reactor. First, the operating principle of a vacuum-injector relies on a flow of gas through a nozzle to create a vacuum at a port near the diverging side of the nozzle, which in turn allows the supply gas stream and vacuum stream to mix internally. Experimental operation of the thermolysis reactor when  $\text{O}_{2(\text{gas})}$  is not being collected is a concern due to high concentrations of the gas and its oxidative properties at elevated concentrations. Utilizing an injector will reduce the overall  $\text{O}_{2(\text{g})}$  concentration downstream of the injector. The device is also not sensitive to vapors, if it is constructed of corrosion resistant materials, and if particulates are filtered out. Second, using a nozzle vacuum-injector pressurizes the mixed

output stream to overcome scrubber pressures or any additional filtering devices without the use of an inline compressor. Therefore, cost and system complexity is reduced with this device.

A vacuum-injector was selected to collect all gases from within the reactor and prevent the reaction products from escaping to the atmosphere. The amount of vacuum generated is proportionate to the incoming air flow rate from an external pressurized supply. Therefore, the internal pressure of the thermolysis reactor may be monitored and adjusted utilizing an electronic proportionate regulator. Although the ideal pressure for the thermolysis reactor is between 1 and 2 bar, a small negative pressure will not allow volatile gases to escape into the thermolysis reactor enclosure.

#### 3.1.4 LOAD CELLS

The mass of the reactor will be monitored by two load cells (Omega LCM703-150) mounted under the reactor flange. While the hydraulic cylinder is retracted and the thermolysis reactor assembly is horizontal, the load cells capture the combined mass,  $m_{\text{reactor}}$ , of the reactor crucible, phase separator, and the reactor contents. However, as the assembly tilts, the observed mass on the load cell,  $m_{\text{observed}}$ , is affected by the tilt angle,  $\alpha$ , which is related by equation (8).

$$m_{\text{reactor}} = \frac{m_{\text{observed}}}{\cos \alpha} \quad (8)$$

The longitudinal forces generated during the tilt cannot be translated through the load cells. Therefore, the load cells were installed in linear guide assemblies to isolate forces normal to the load cells. The guides had a pair of industrial grade die pins and bushings to allow linear motion. High temperature grease was used to lubricate the assemblies.

Each load cell was connected to a signal conditioning unit for amplification and noise reduction prior to being connected to the data logger.

Process monitoring may be accomplished with these load cells, and can be used to identify the amount of material entering or leaving the reactor. Volumetric metering of the inlet may be difficult due to aggregation of incoming  $\text{CuO} \cdot \text{CuCl}_2$  granules. Furthermore, it would be very difficult to relate the gas flow rate to a totalized mass of entrained granules. A mass transfer between stages is more accurate and should be utilized for process monitoring. The load cells can also be used to determine the rate of reaction. As the decomposition reaction proceeds, the mass of the contents is reduced proportionate to the mass of  $\text{O}_{2(g)}$  leaving the reactor. An automated system can determine when the reaction is complete by observing the reactor mass: once the mass is stable, the reaction is complete. Subsequently, the molten  $\text{CuCl}$  is poured into the quench vessel, and the mass of salt removed is equivalent to the difference of the masses before and after the transfer.

### 3.1.5 TEMPERATURE CONTROL

Critical components in the thermal system included the PID temperature controller (Automation Direct SL4848-RR), band-heater, and coiled heating tape under the reactor. The temperature controller is equipped with remote access and control via MODBUS/RTU protocol – a feature necessary for preliminary centralized control and automation of the Cu-Cl process.

The crucible is heated with a custom-made 1300W ceramic band heater (MPI Inc.) around the perimeter of the cylindrical section, in conjunction with a 627W heating tape (Omega STH051-080) arranged to heat the center curved crucible during startup (Figure 16). The heating tape was required to decrease the heating time when  $\text{CuCl}$  is in granular form, by delivering heat directly to the center of the crucible.

Combined maximum heating power for the assembly was 1927W. The maximum temperature at each heat source was  $650^\circ\text{C}$ , so that the heating elements can be protected from excessive heating cycles. The process

temperature was observed at two heating combinations: band heater only (single heat source), and band heater combined with the coiled heating tape (dual heat source).

The band heater and base heater were controlled by an industrial proportional, integral and differential (PID) process controller. The process controller utilized a Type-K thermocouple to monitor the temperature of the respective heaters and maintain a safe working temperature. Set point settings were communicated via MODBUS/RTU to the controller, which automated the testing process and facilitated future centralized monitoring of the decomposition reaction. Temperature control utilized the PID routine in the process controllers to maintain optimal temperature. The controller was set to adjust the PID settings based on the system response. With an unknown plant transfer function a step input was applied and used to determine PID parameters, analogous to the Ziegler-Nichols step-response method for obtaining PID coefficients [49]. The auto-tuning feature was used the first time the reactor was operated.



Figure 16: Heating devices for crucible: band heater assembled on inverted crucible (Left) and Heating tape (Right).

### 3.1.6 REACTOR TILT CONTROL

Molten CuCl must be transferred to the quench vessel once the decomposition of  $\text{CuO} \cdot \text{CuCl}_2$  is complete. A hydraulic tilting mechanism was used to pivot the crucible between horizontal and  $75^\circ$ . The tip of the spout was positioned to be coincident with the rotation axis of the tilting assembly in order to keep the spout tip in a fixed location during tilting. An alternative for tilting the crucible to pour the contents into the quench vessel is to implement a dump valve at the base of the crucible.

Hydraulic controls were required to incline the crucible to pour molten salt into the quench vessel. The tilting motion was attained by a single hydraulic cylinder, with a 50.8mm bore, pushing the tilting frame subassembly. When the cylinder was fully retracted the thermolysis reactor was horizontal. As the cylinder was extended the thermolysis reactor was tilted to pour the molten salt through the spout. A small variable frequency drive (Eurodrive MOVITRAC LE) was used to control the hydraulic pump revolution rate at 600 rpm, and thus maintain a constant rate of displacement of the hydraulic cylinder. This ensured smooth and steady tilting of the reactor.

### 3.1.7 OVERVIEW OF THERMOLYSIS REACTOR OPERATION

To initiate a test, first the main breaker was activated to allow all systems to power up. The electronic components were allowed 20 minutes to reach stable operating temperatures. Next, the DAQ was initialized and data recording was started.

The main gas inflow and outflows are located at the top of the reactor; these are the  $\text{N}_2$  purging port and the vacuum port. The spout was sealed for heating experiments to avoid vapor loss. The thermolysis reactor was purged with  $\text{N}_2$  by opening the  $\text{N}_2$  cylinder valve for 10 minutes. Simultaneously, the vacuum injector was activated to remove the air and  $\text{N}_2$  mixture from the reactor. The

N<sub>2</sub> was turned off and the vacuum injector was periodically turned on to maintain an internal pressure of 1.0 bar.

Next, the heating system was activated at the control panel and the temperature set-point was configured through the software interface. A set-point of 650°C was used and monitored with a thermocouple at the heater-crucible interface. The temperature rise for a CuCl sample size of 2.0kg and crucible was monitored through software. Once a steady temperature was reached it was maintained for 60 minutes, after which the heating system was deactivated. The cool-down temperatures were also recorded.

### 3.2 THERMOLYSIS REACTOR MASS FLOW

Conversion of the double salt, CuO • CuCl<sub>2</sub>, to cuprous chloride and oxygen gas occurs as the temperature of the reactor surpasses 480°C. Currently, the thermolysis reactor is intended to be operated as a semi-batch system. That is, reactants will dwell in the reactor until the decomposition reaction is complete. In a continuously operating system the flow of reactants into and products out of the reactor is simultaneous.

Once the thermolysis reaction is completed, most of the molten cuprous chloride is transferred into the quench vessel. The remaining molten CuCl is intended to increase the heat transfer rate into the powdered CuO • CuCl<sub>2</sub> entering the reactor in the next batch.

The physical limitations of the reactor allow up to 2.5 L of contents (i.e. 10.35 kg of CuCl at 25°C). This volumetric limitation is important to note as the density of the molten CuCl varies throughout the process and, therefore, limits the maximum volume of the batch. Additionally, the specific volume increases

Table 4: Species properties in thermolysis reactor during full conversion

| Species               | Molar Mass<br>[g mol <sup>-1</sup> ] | Density<br>[g cm <sup>-3</sup> ]                                 | Reference |
|-----------------------|--------------------------------------|--|-----------|
| CuCl                  | 99.00                                | 3.692 (molten 483°C)<br>4.140 (solid, 25°C)                      | [50]      |
| CuO•CuCl <sub>2</sub> | 214.00                               | 4.853 (solid, 25°C)  | [50]      |
| O <sub>2</sub>        | 32.00                                | 1.308x10 <sup>-3</sup> (25°C)<br>0.504 x10 <sup>-3</sup> (500°C) | Gas Law   |

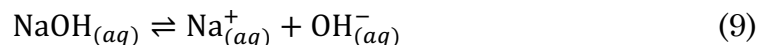
as CuO•CuCl<sub>2</sub> decomposes to CuCl, thereby increasing the volume of molten salt in the reactor. Table 4 shows the material properties for each reactant and product of a complete reaction in the thermolysis stage.

### 3.2.1 REACTOR EFFLUENT GAS SCRUBBER

Molten CuCl in the thermolysis reactor will remain in a stable form if an inert atmosphere is maintained inside the reactor. Degradation of the molten salt will occur when CuCl is oxidized at the surface or when the temperature is excessively high, possibly forming chlorine gas in the reactor. In the experimental setup, the thermolysis reactor is maintained at a slight negative gauge pressure to collect all gases formed within the reactor, which may be removed in a wet scrubber. Gases and vapors will be entrained in the effluent flow from the thermolysis reactor. A packed bubble column filled with an alkali solution will sequester chlorine gas and vapors from the effluent flow prior to venting to the atmosphere.

There are several alkali solutions which may be used to neutralize aqueous chlorine in the scrubber. Among these are sodium hydroxide (i.e. caustic soda) and sodium hydrogen carbonate (i.e. sodium bicarbonate or baking soda). In this section, both substances will be assessed as candidates for the scrubber solution.

Sodium hydroxide is a white granular powder at room temperature, with a molar mass of 39.997 g/mol and a density of 2.13 g/cm<sup>3</sup>. In solution, it hydrolyses to produce sodium and hydroxide ions:



Sodium hydroxide is a strong alkali and is commonly used to neutralize acids. The molar concentration of hydroxide ions in a solution is used to determine the solution pH for a strong base, which is defined as:

$$\text{pH} = 14 - \log [\text{OH}^{-}] \quad (10)$$

Similarly, the pH for an acidic solution requires the hydrogen ion molar concentration:

$$\text{pH} = -\log [\text{H}^{+}] \quad (11)$$

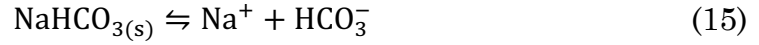
Determining the amount of sequestered chlorine gas requires the examination of how chlorine gas is absorbed in solution, and then how it is neutralized. When chlorine gas is bubbled in a water column, an aqueous solution with dissolved chlorine will be present.



The process of dissolving chlorine gas increases the concentration of hydrogen ions, reducing the solution pH. Adding a base to the solution reduces the hydrogen ions and, therefore, drives the equilibria to the right.

Another option for the base solution is sodium hydrogen carbonate. Sodium hydrogen carbonate has a molar mass of 84.007 g/mol and density of 2.2g/cm<sup>3</sup>.

Unlike sodium hydroxide, sodium hydrogen carbonate is a weak alkali. The hydrolysis equilibria for sodium hydrogen carbonate in water is shown in (15), (16) and (17).



Unlike a strong base, sodium hydrogen carbonate has a second dissociation which contributes another proton to the solution from the carbonic acid molecule,  $\text{HCO}_3$ . Calculating the pH of a weak alkali solution differs from the method used for a strong alkali, because the formation of additional hydrogen ions during dissociation must be considered whilst determining the solution pH. An acid dissociation constant representing the hydrogen ion concentration formed during dissociation is available for common weak alkalis. The acid dissolution constant for sodium hydrogen carbonate is  $K_{a1} = 4.3 \times 10^{-7}$  and  $K_{a2} = 4.8 \times 10^{-11}$ . The pH of a sodium hydrogen carbonation solution is calculated by analyzing the individual contributions of each hydrolysis step.

$$K_{a1} = \frac{[\text{H}^+][\text{HCO}_3^-]}{[\text{NaHCO}_3]} \quad (18)$$

$$K_{a2} = \frac{[\text{H}^+][\text{CO}_3^{2-}]}{[\text{HCO}_3^-]} \quad (19)$$

$$K_w = K_a K_b \quad (20)$$

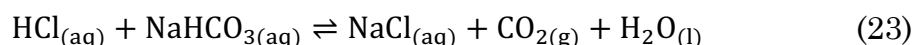
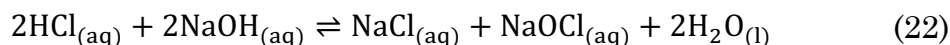
$$\text{pH} = 14 - \frac{1}{2}\text{p}K_b + \frac{1}{2}\log [\text{B}] \quad (21)$$

In equation (21),  $K_b$  is the base ionization constant, and B is the base concentration (i.e. concentration of  $\text{OH}^-$ ). Gas scrubber solution molarities and theoretical chlorine sequestering limits are noted in Table 5.

Table 5: Cl<sub>2</sub> gas removed from gas stream.

| Base               | Molarity<br>[mol L <sup>-1</sup> ] | Solution pH at<br>25°C | Cl <sub>2</sub> Sequestered<br>[mol L <sup>-1</sup> ] |
|--------------------|------------------------------------|------------------------|---|
| NaOH               | 0.5                                | 9.9                    | 0.25  |
| NaHCO <sub>3</sub> | 1.0                                | 8.5                    | 0.5   |

The net reaction when Cl<sub>2</sub> is scrubbed with NaOH is shown in equation (22) and equation (23) with NaHCO<sub>3</sub>.



The use of either sodium hydrogen carbonate or sodium hydroxide is acceptable as a neutralizing solution for a chlorine scrubber. Sodium hydrogen carbonate is safer to handle compared to a sodium hydroxide solution. Therefore, the scrubber solution will be sodium hydrogen carbonate. Increasing the molarity of sodium hydrogen carbonate beyond this limit will not significantly improve the capture Cl<sub>2</sub>. In previous experiments at CERL, a 1M solution was used. However, NaOH is a better if only HCl<sub>(g)</sub> and CO<sub>2(g)</sub> are expected to be directly vented into the atmosphere [38]. Furthermore, it should be noted that the sodium hydrogen carbonate solution is saturated with chlorine gas once precipitate appears in solution.

### 3.2.2 GAS ENTRAINMENT

Above the molten CuCl, rising effluent gases can entrain solid or liquid particles. This may lead to an accumulation of solidified CuCl in the tubing leaving the reactor, and a reduction of reactor performance. Consideration of phase separation techniques is, therefore, required to reduce the risk of these events.

Phase separators may be configured in one of two orientations: vertical and horizontal. Vertically orientated reactors are more suited for low to medium

gas to liquid ratios, which is appropriate for the low vapor flow rate of the thermolysis reactor [51].

There are four regions of a vertical separator: the inlet, the liquid collection, gravity settling section and the mist extractor. At the inlet, the incoming mixture of liquid and gas goes through a gross phase separation. This is achieved by an abrupt change in direction due to the inlet diverter allowing solids and liquids to dissipate kinetic energy and remain in the reactor. Inlet velocity and incoming mixture properties are used to select a diverter design. For the experimental thermolysis reactor,  $\text{CuO} \cdot \text{CuCl}_2$  is expected to be slowly fed into the reactor. Some air or purging gas may enter the separator with the granules. However, the inlet velocity is not expected to be very high and, therefore, a specific design for an inlet will not be required.

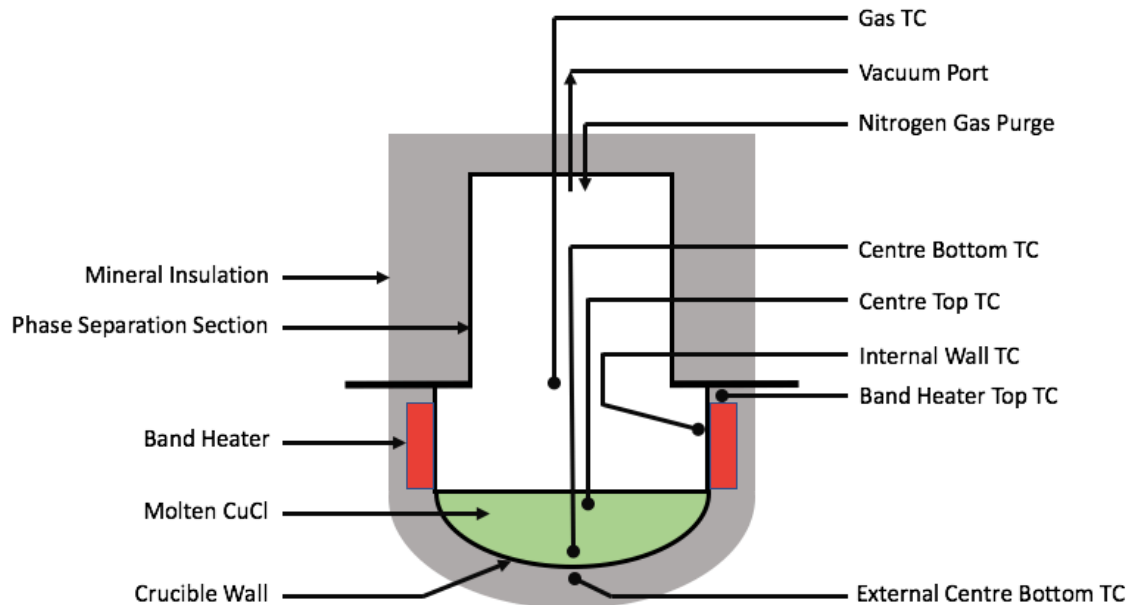


Figure 17: Key features of the thermolysis reactor.

The collection area must be large enough to contain the molten  $\text{CuCl}$  and  $\text{CuO} \cdot \text{CuCl}_2$  mixture. To automate the process a fluid level controller may be implemented to open and close a valve once a predetermined level has been reached. A drain valve on the base should also be included to allow the separator to be completely emptied. If a settling particulate is being processed

(either incoming with the mixture or precipitating during the reaction), the base of the separator may be constructed with a conical section with an opening angle ranging between  $45^\circ$  to  $60^\circ$  to allow all the particulates to be cleared from the chamber when the drain is opened. The reactor utilized in the experiment used a spout to pour the molten contents out to reduce valve complexity and overall apparatus expense.

In the gravity settling section, suspended particles in the diameter range of 100 to 140  $\mu\text{m}$  are expected to fall back to the surface of the molten  $\text{CuCl}$ . Assuming the particles are spherical there are two main forces at work: the force of gravity and the drag force, which is dependent on the particle speed. The sum of these two forces determines the direction of travel on the particle. Stewart and Arnold present a method for calculating the nominal sizes of a vertical reactor [51]. First, the operating conditions of the reactor are determined: minimum and maximum flow rates, operating pressure, operating temperature, and droplet size to be separated. Based on these parameters, the minimum required separator internal diameter [mm],  $d$ , is calculated using equation (24).

$$d = \sqrt{344444 \left[ \frac{TZQ_g}{P} \right] \left[ \left( \frac{\rho_g}{\rho_l - \rho_g} \right) \frac{C_D}{d_m} \right]^{1/2}} \quad (24)$$

Where  $T$  is the operating temperature [K],  $Z$  is the gas compressibility,  $Q_g$  is the gas flow rate [standard cubic meters per hour],  $P$  is the operating pressure [kPa],  $\rho_g$  is the gas density [ $\text{kg}/\text{m}^3$ ],  $\rho_l$  is the liquid density [ $\text{kg}/\text{m}^3$ ],  $C_D$  is the drag coefficient, and  $d_m$  is the liquid droplet diameter [ $\mu\text{m}$ ].

The settling height of the chamber was estimated by analyzing the forces on suspended droplets. The terminal velocity,  $V_t$ , the droplet was determined by using the iterative Souders-Brown procedure (where  $d_m$  is in  $\mu\text{m}$ ) [51] [52].

1. An initial value for a droplet terminal velocity was calculated with an initial  $C_D$  equal to 0.34.

$$V_t = 0.0062 \left[ \frac{(\rho_l - \rho_g)d_m}{\rho_g} \right]^{1/2} \quad (25)$$

2. Next, the Reynolds's number was determined.

$$Re = 0.001 \frac{\rho_g d_m V}{\mu} \quad (26)$$

3. The drag coefficient for a spherical particle,  $C_D$ , was recalculated.

$$C_D = \frac{24}{Re} + \frac{3}{Re^{1/2}} + 0.34 \quad (27)$$

4. A new terminal velocity with the new drag coefficient was obtained.

$$V_t = 0.0036 \left[ \frac{(\rho_l - \rho_g)d_m}{\rho_g C_D} \right]^{1/2} \quad (28)$$

5. Steps 2 through 4 were repeated until the terminal velocity converged.

A relationship between the Reynolds number, particle geometry and the drag coefficient is shown in Figure 18. The theoretical drag coefficient is a linear relationship according to Stokes Law. However, the droplets behave in a different manner.

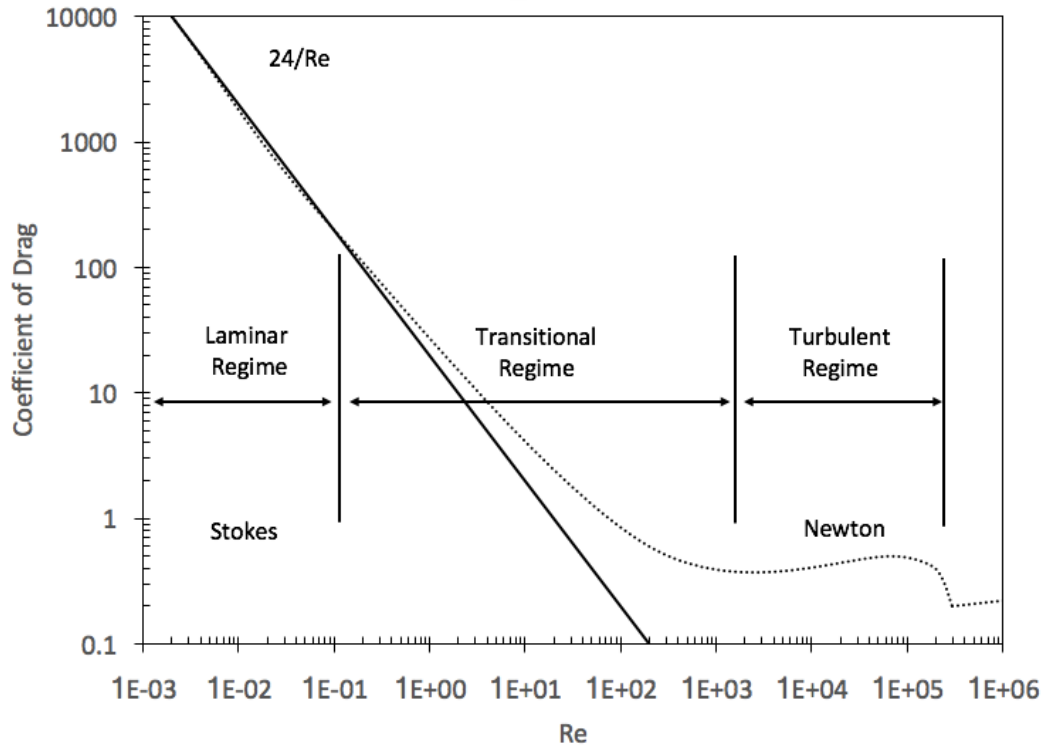


Figure 18: Drag coefficient for droplets, observed and theoretical [53].

As the Reynolds number moves beyond a value of 4, the drag coefficient diverges from the theoretical line. Furthermore, disk and cylindrically shaped droplets have a different drag coefficient relationship, where disks have a higher coefficient of drag.

The terminal velocity and minimum phase separation diameter were calculated for particle sizes ranging from 10 to 200  $\mu\text{m}$  and are shown in Figure 19.

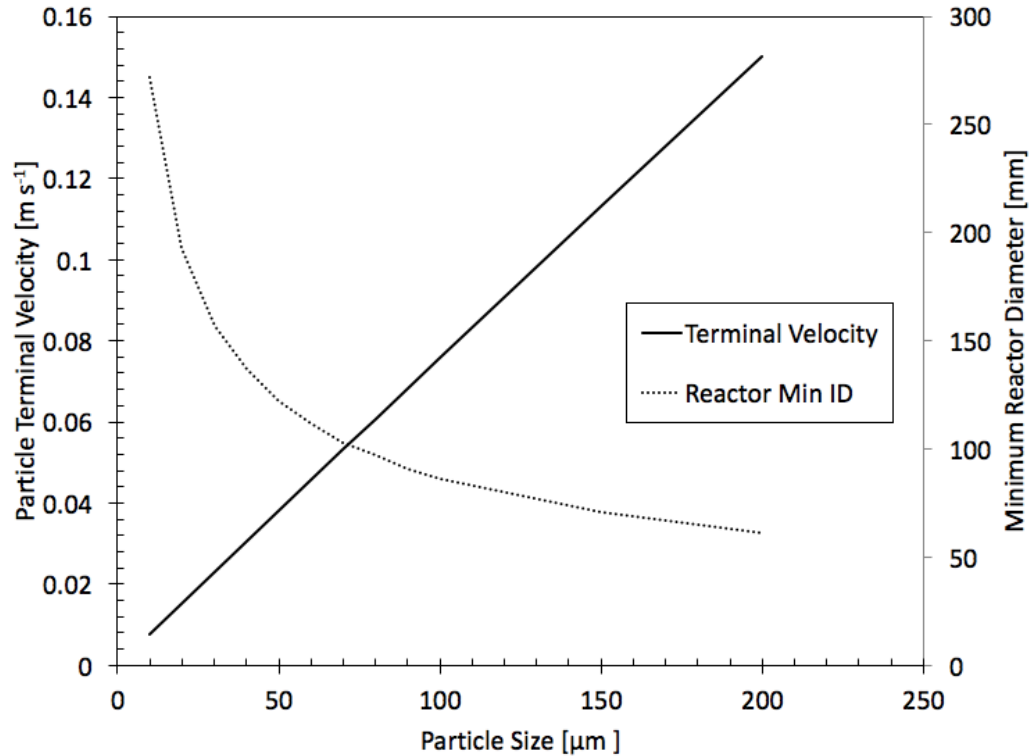


Figure 19: Terminal velocity and minimum phase separator diameter as a function of particle size, gas flow  $0.6\text{m}^3\text{ h}^{-1}$ , liquid flow  $0.002\text{m}^3\text{ h}^{-1}$ ,  $101.3\text{ Pa}$ ,  $773\text{K}$ .

Any remaining particles entrained in the effluent gas are trapped in the mist extractor. The mist extractor is designed to use inertial impaction, direct interception or Brownian diffusion to collect the particles on the surface of the extractor, as seen in Figure 20. Common materials for the extractor include wire meshes for low to medium flows, baffles for medium to high flows or diffusion membranes for low flows. Particle sizes ranging from  $1\text{-}10\ \mu\text{m}$  are most effectively removed by inertial impaction, sizes  $0.3\text{-}1\ \mu\text{m}$  require direct interception and particles less than  $0.3\ \mu\text{m}$  in diameter randomly move about and collect on the extractor surface (Brownian motion). Wire meshes allow the gas to pass through with minimal back pressure. Baffles on the other hand are designed to take advantage of the higher gas velocities. That is, the quickly moving low density gas can move around the baffle but the entrained particle collides with the surface and coalesces with other captured particles.

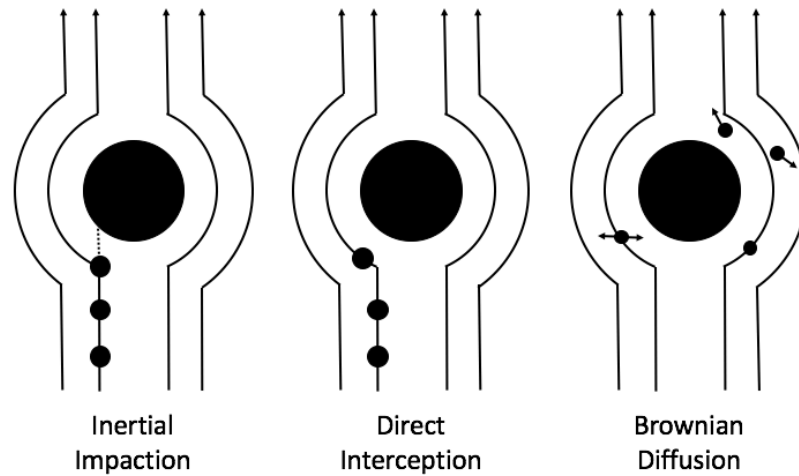


Figure 20: Three methods for extraction of mist entrained in a gas flow [51].

In terms of the oxygen reactor design, phase separation must be addressed to produce a viable and expandable design. A method of mist extraction will be determined once the diameter of the entrained particles is known, but because the gas velocity is expected to be low, the wire mesh mist extractor is the most likely choice for the reactor due to cost and applicability given the low effluent gas velocity.

### 3.2.3 REACTOR CORROSION

Stainless steels are versatile materials for numerous applications. Their availability, chemical resistance, and low cost are key reasons why they are usually selected for many harsh environments. For the thermolysis reactor, the environment created by the molten salt, small amounts of corrosion will accumulate impurities over time, because the salts are reused in the cycle. The rate of accumulation is dependent on the rate of corrosion. However, a 304-stainless-steel crucible was used during experimentation because the duration of use was limited.

Other materials like titanium and Hastelloy C-series metals are also feasible selections for the oxygen reactor body. Figure 21 shows the range of corrosion resistance for various metals in oxidizing and reducing environments. Here the

effective usability of stainless steels (types 316 and 304) versus other material selections can be easily determined. The molten compounds in the oxygen reactor are chloride bearing and, therefore, only the upper portion of the chart lists usable materials, which excludes stainless steels for long duration usage.

Unalloyed titanium has a reasonable effective resistance to oxidizing compounds. This is also apparent with respect to alloyed titanium, of which Ti-STa and Ti-0.15Pd have a slightly better performance range. Hastelloy C is another valid candidate; however, the relative cost of the material is significantly higher than stainless steels and titanium [54]. It may still be a good candidate for locations where material conductivity for is needed such as the heating coil.

Studies at CERL have shown that some types of coatings are potentially acceptable for usage in direct contact with molten CuCl. Azarbayjani studied ceramic and metallic coatings and concluded that metallic coatings were more likely to withstand the harsh environment [55]. YSZ coatings were not suitable and corroded quickly – within 5 hours. Azarbayjani argued that there may be some thermal expansion mismatch and/or lack of adhesion between the ceramic coatings and base materials and this was the cause for the fractured coating. On the other hand, the metallic coatings – Diamalloy 4006 and SHS 9172 – performed much better and showed little corrosion after 100 hours of partial submersion in CuCl.

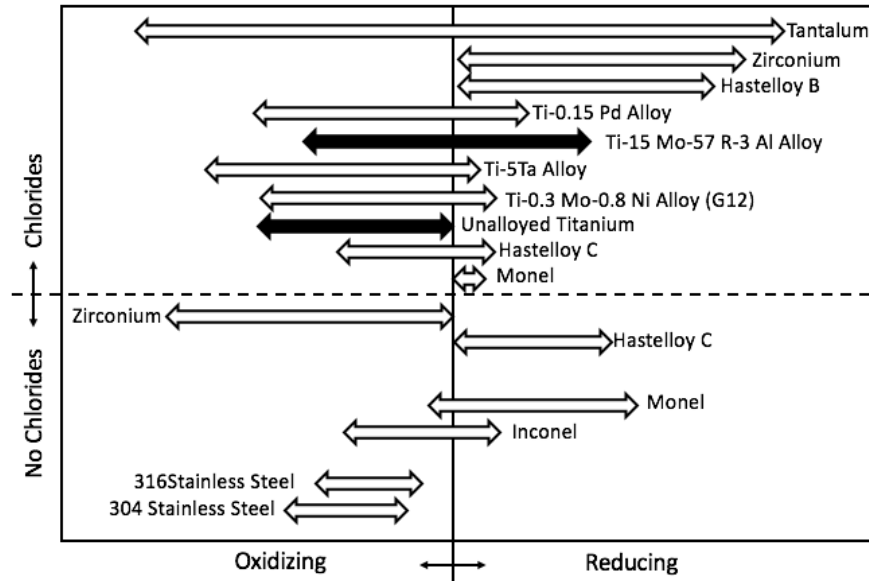


Figure 21: Material corrosion resistance ranges dependent on presence of chlorides, and oxidizing or reducing compounds [56].

Examining the formulation of Diamalloy 4006 showed a similarity to C-series Hastelloy, mainly through the large content of nickel and chromium. SHS 9172 is mainly composed of iron, chromium and tungsten.

Hastelloy C276 has a corrosion rate of less than 0.05 mm/year in cuprous chloride at 235°C [57]. Commercially pure titanium has a corrosion rate of <0.003 mm/year at a 50% concentration of cuprous chloride at 90°C [56]. But noting the ranges of oxidation resistance in Figure 21, some titanium alloys should be capable of similar or better performance when compared to Hastelloy C-series materials.

### 3.3 PROCEDURE FOR ANSYS THERMAL SIMULATIONS

A transient thermal simulation was used to examine the heat flow through the thermolysis reactor. The simulations calculated the temperature profile in the molten CuCl given a fixed forced convection rate at the molten surface, and heat input from a single heating source (band heater only heating) or dual heating sources (band heater and contoured heating tape). The 2-dimensional

(2D) models consisted of a stainless-steel crucible, 1300W band heater, 150W lower band heater and a mass of CuCl.

### 3.3.1 SIMULATION MODEL AND SOLVER SETUP

The thermolysis reactor components were created in CAD. Figure 22 shows a 3-dimensional (3D) view of the thermal model and the main components. For the 2D simplification, the thermolysis reactor was assumed to be axis symmetric. That is, the fact that the band heater was not continuous around the crucible near the spout was not included in the scope of the simulation.

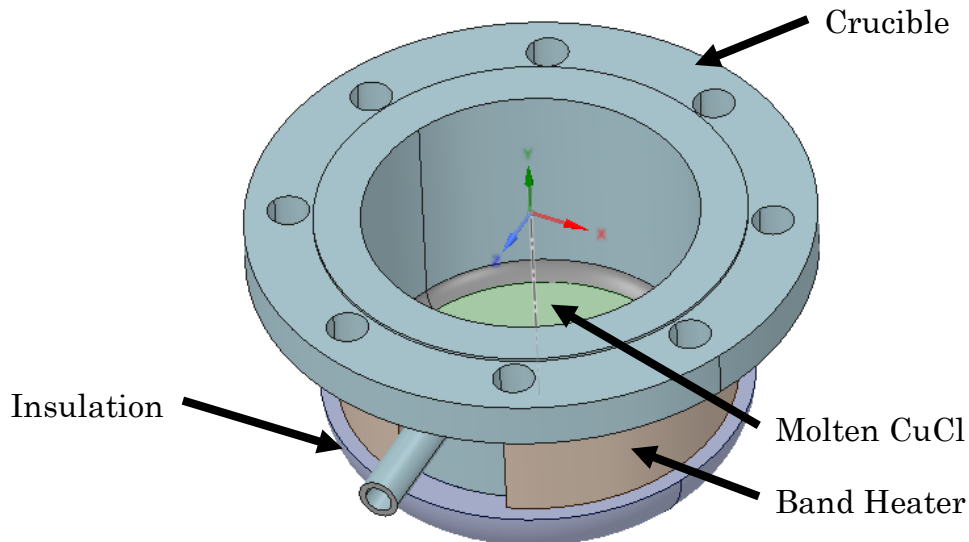


Figure 22: Key components in ANSYS transient thermal simulation.

Additionally, only half of a cross-section through the center of the crucible was analyzed due to symmetry. In this model, the crucible material was set to stainless steel, and the insulation below the crucible was mineral wool 25.4mm thick. These components are labelled in Figure 23. The boundary conditions applied to the model duplicated the physical setup. The temperature ramp-up on the band heater increased from 22°C to 650°C over a time of 3600 seconds, and was applied to the exterior of the band heater. When the simulation included the secondary heating surface on the base of the crucible, the same temperature limits were used, however, they ramp-up occurred over an 1800

second duration, as was demonstrated in the actual heat-up time of the physical element. The insulated surface on the base had a constant temperature of 22°C on the exterior. At the flange of the crucible a radiation boundary condition and a  $10\text{Wm}^{-2}\text{K}^{-1}$  convective boundary condition was applied. A convection boundary condition was also applied to the surface of the CuCl. Estimated surface convection rates of free convection were utilized to acquire more insight into the temperature distribution in the CuCl. The values used in the simulation were 1.0, 2.0 and  $4.0\text{W/m}^2\text{K}^{-1}$ . Depending on the temperature distribution in the vapor separation section the contribution of convection heat loss may be significant. Based on the proposed integrated system design, it is expected for the incoming solid-gas mixture into the thermolysis reactor (i.e.  $\text{CuO}\cdot\text{CuCl}_2$  and  $\text{N}_2$ ) to be above 400°C, which keeps the surface convection coefficients low.

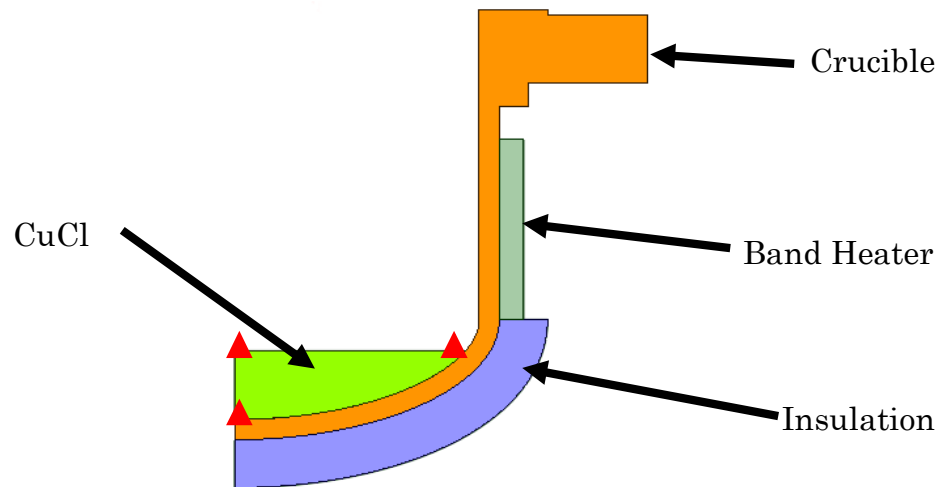


Figure 23: 2D model of thermolysis reactor used in 2.0kg ANSYS transient thermal simulation. Red triangles indicate simulation temperature probe locations.

Thermal properties of CuCl utilized for this analysis are listed in Table 6. Simulation masses included 2.0 kg and 10.35 kg of CuCl. These masses were selected to examine low and high volumes of CuCl in the existing thermolysis reactor. The 2.0 kg simulations were conducted to match the experimental setup and to provide a comparison of start-up performance.

Table 6: CuCl thermal properties used in thermal simulations.

| Property             | Value  | Reference |
|----------------------|--|-----------|
| Density              | 4140 – 3692 kg m <sup>-3</sup>                 | [58] [38] |
| Thermal Conductivity | 0.8 to 0.313 W m <sup>-1</sup> K <sup>-1</sup> | [58] [36] |
| Thermal Capacity     | 525 – 800 J kg <sup>-1</sup> K <sup>-1</sup>   | [58]      |

The band heater was set to apply a heat flux of 100W until a temperature of 650°C was achieved and then the flux was reduced to maintain the temperature. This simulated the PID controlled temperature controller utilized in the experiments. The auxiliary heater was configured to the same maximum temperature as the band heater, and also to a maximum power of 150W, which is approximately 25% duty cycle of the full power.

A transient thermal solver was selected to observe the heat transfer throughout the CuCl. In addition, the transient model will provide estimates for start-up duration of the thermolysis reactor. Solver settings for the analysis are shown in Table 7.

Table 7: ANSYS solver and model settings.

| Setting                   | Parameter                                      | Value            |
|---------------------------|--|------------------|
| Solver                    | Thermal Transient (MADPL)                      |                  |
| Solver Type               |  | Direct/Iterative |
| Time Step                 | Minimum  | 1 s              |
|                           | Maximum  | 3600 s           |
| Step End Time             | 2.0kg CuCl                                     | 50000 s          |
|                           | 10.35kg CuCl                                   | 100000 s         |
| Convergence Criteria      | Heat Flux Convergence                          | 0.5%             |
|                           | Temperature Convergence                        | 0.5%             |
| Initial Model Temperature |  | 22°C             |
| Materials                 | Stainless Steel, CuCl, Mineral Wool Insulation |                  |

Each time step was completed with the analysis of convergence criteria for temperature. If the residuals are below the configuration threshold, then the time step was incremented, and the iteration commences again with updated temperature values throughout the model.

The maximum analysis time for the transient model was determined by examining the resultant temperature stability between successive iterations. The solver was configured to automatically adjust the step time based on the stability of the solution. The minimum time step was 1 second and the maximum was 3600 seconds. In the initial stages of the analysis the minimum time step was applied, and as the system stabilized the time interval began to increase approaching the maximum time step setting.

Convergence of the model was determined by the stability of the minimum, maximum and probe temperatures in the model. The simulation was terminated at the step end time. Three probe temperatures were added at key locations of the CuCl: top surface center, bottom surface center and top surface CuCl-crucible interface, as seen in Figure 23.

### 3.3.2 MESH SENSITIVITY ANALYSIS

The 2D representation of the thermolysis reactor must be discretized prior analysis into nodes and elements. Elements are lines (or groups of lines) between neighboring nodes, which form a mesh to represent the geometry to be analyzed. The shape functions between nodes are then evaluated to produce the thermal gradient throughout the model. These shape functions can be linear or quadratic, and applied to 2-dimensional and 3-dimensional elements [59]. For simple rectilinear geometries, it is common to use quadrilateral elements. However, irregular geometries are best approximated by triangular elements. Additionally, the size and quantity of the element must be appropriate to accurately represent the geometry to be analyzed. For this reason, a mesh independence analysis was conducted.

The temperature on the top surface of the CuCl was of interest and was utilized to assess the mesh independence in the thermal simulation. The 2D geometry presented in previous section was discretized (i.e. meshed) at varying element sizes. Table 8 shows the resultant number of nodes and elements at 1.5, 2.0, 5.0, 7.0 and 10mm maximum element sizes. As the element size was reduced, the number of nodes and elements increased. Consequently, the temperature variation between consecutive studies was decreased.

Table 8: Details of mesh independence study for 1.5mm, 2.0mm, 5.0mm, 7.0mm and 10.0mm maximum element sizes.

| <b>Max Element Length [mm]</b> | <b>Nodes</b> | <b>Elements</b> | <b>Temperature [°C]</b> |
|--------------------------------|--------------|-----------------|-------------------------|
| 1.5                            | 10325        | 15011           | 389.6                   |
| 2                              | 5733         | 7734            | 389.9                   |
| 5                              | 1163         | 1402            | 391.5                   |
| 7                              | 701          | 783             | 392.9                   |
| 10                             | 389          | 377             | 398.0                   |

Selected discretized models are shown in Figure 24. The figures show a 1.5, 2.0 and 5.0mm element size. Discretization methods included quadrilateral and triangular profiles. The triangular element configuration, however, was predominantly used throughout the model where a gradual curvature present. These locations were not easily discretized with quadrilateral elements. The inset image in Figure 24 shows a close-up of the fine mesh at the CuCl and crucible wall and exterior insulation. The 5.0mm discretization on the right of Figure 24 shows a varying number of elements through the crucible along the curved base. This variation in elements may produce larger errors compared to locations where there are more elements. Therefore, reducing the maximum element size allows for an even distribution of elements through constant-thickness sections, and, ultimately, a reduced simulation error.

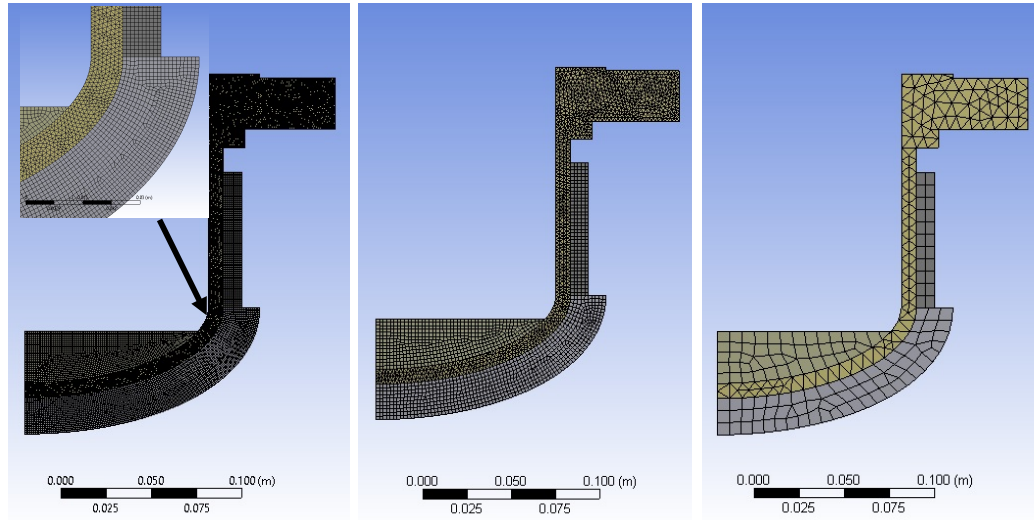


Figure 24: Simulation model mesh configurations at 1.5mm, 2.0mm and 5.0mm element sizes.

A mesh size of 2.0mm was selected for the study, since increasing the quantity of nodes did not introduce significant changes in the final surface temperature.

### 3.4 PROCEDURE FOR HEATING A SAMPLE OF ISO HEAT 493

Initial testing of the thermolysis reactor was conducted using an industrial quenching salt, ISO-HEAT 493 (Park Thermal International Corp.) The salt melts at 493°C, and boils at 927°C.

A sample of ISO HEAT 493 weighing 2.0 kg was collected and transferred into the thermolysis reactor. The thermolysis reactor was insulated and thermocouples were inserted into the salt near the top surface at the center and 75mm offset.

Heating began with a configuring the temperature controller to a set point of 650°C. During the initial startup, the temperature controller was enabled to perform PID auto-tuning. PID is a control loop feedback structure that allows the thermal controller to continuously adjust the output heating flux based on the set point and current process temperature. Subsequent tests utilized a set point of 650°C and the same PID coefficients. Once the temperature settled, the reactor was allowed to dwell at the temperature for approximately 1 hour

to melt the contents of the reactor. Finally, the reactor was turned off and the contents were cooled through natural convection.

A data acquisition system was utilized throughout the testing to record the temperature variations in the thermolysis reactor. This procedure was repeated with an initial set point of 650°C to produce the fastest ramp-up to a melting temperature in the center of the crucible.

### 3.5 PROCEDURE FOR HEATING A SAMPLE OF CUCL

Upon completion of the industrial salt tests, the thermolysis reactor was cleaned and reassembled with CuCl. A sample weighing 2.0 kg was added to the thermolysis reactor. Thermocouples were inserted into the powder at the top center and bottom center location to monitor the temperature gradient in the sample.

To reduce thermal losses, all exposed surfaces were covered with 25.4mm of Roxul mineral-wool insulation. The thermal barrier assisted in eliminating convective losses from the surface of the crucible, heaters and vapor settling cap. Thermal resistance of the insulation is  $0.71\text{m}^2 \text{K W}^{-1}$  at a thickness of 25.4mm.

Prior to operating the heating system, the reactor was purged with  $\text{N}_{2(\text{gas})}$  for 10 minutes to displace all atmospheric air. The excess  $\text{N}_{2(\text{gas})}$  was removed using the vapor removal ports (i.e. the vacuum injector) and vented into the gas scrubber.

Two heating scenarios were tested: single and dual heating sources. With a single heating source, the band heater was sent to 650°C set point. In the dual heat source tests, both the band heater and coiled heater were set to a temperature of 650°C.

Upon disconnecting the heating system,  $N_{2(gas)}$  was again pumped into the thermolysis reactor for a duration of 10 minutes. The assembly was allowed to cool overnight and opened for inspection.

### 3.6 SUMMARY

The design of the thermolysis reactor relies on numerous subsystems being present for consistent and safe operation. A user interface was designed and constructed to control the heaters, tilting and vapor handling.

Transient thermal simulations were proposed with a 2.0 kg and 10.35 kg mass of CuCl, using a single band heater on the perimeter of the crucible, and then with a band heater and contoured heater on the base. The experimental procedure would observe the temperature at the center of the molten surface and the temperature at each heat source inside the crucible. Finally, a comparison of the simulated and recorded temperature rise at the top surface will be made.

# RESULTS AND DISCUSSION

# 4

## 4.1 THERMAL SIMULATIONS

Thermal simulations of the reactor were completed to visualize the heat flow through the assembly and into the CuCl. The first set of simulations examined a single heating source around the cylindrical perimeter of the crucible (i.e. the band heater) and the temperature distribution into the center of the CuCl mass. The center top of the CuCl is an area of interest due to its distance relative to the heating surfaces. That is, the thermal resistance is the greatest from any heated surface. The mass of CuCl in the crucible was 2.0 kg, which is a volume of 483 ml at 25°C with a solid density of 4.14 g/cm<sup>3</sup>. This mass of CuCl was selected to simulate a startup condition after the crucible has been emptied. A second set of simulations incorporated a secondary heated surface on the ellipsoid section on the base of the crucible. A third set of simulations was processed for a full reactor with a CuCl mass of 10.35kg and two heaters.

Heating rates are highest directly adjacent to the band heater or contoured base heater, as these are the locations with the lowest thermal resistance and, therefore, the highest thermal flux into the reactor. In a full reactor, these regions will also be the first to melt and reach the decomposition temperature.

Heat loss through forced convection on the molten surface is estimated to be minimal for two reasons. First, the hot effluent O<sub>2</sub> gas will be moving upward to the exit gas port, reducing or even fully eliminating downward gas currents. Second, the heated perimeter above the surface of the molten salt will keep the

volume of gas at an elevated temperature. Incoming  $\text{CuO} \cdot \text{CuCl}_2$ , however, will enter the reactor at a lower temperature with a carrier gas (e.g.  $\text{N}_2$  gas) at a temperature between  $340^\circ\text{C}$  and  $400^\circ\text{C}$  from the hydrolysis stage, which will increase surface convection rates. Therefore, simulating moderate forced convection rates on the surface of the molten salt will aid in quantifying the effects on surface temperatures.

#### 4.1.1 TEMPERATURE DISTRIBUTION WITH 2.0KG $\text{CuCl}$

The convection rates applied to the top surface were set to 0.5, 1.0, 2.0 and 4.0  $\text{Wm}^{-2} \text{K}^{-1}$  (N.B. 0.5 applied to single-heater configuration only). Diagrams of temperature distributions with a single heater and 2.0kg of  $\text{CuCl}$  are seen in Figure 26-24. These figures show that the temperature drop through the wall of stainless steel crucible is minimal. However, the heat flow through the stainless steel crucible in the downward axial direction limits the temperature at the bottom center. This results in a  $\text{CuCl}$  surface temperature that is below the minimal  $480^\circ\text{C}$ , a critical requirement for decomposition, in all cases with a single heated surface.

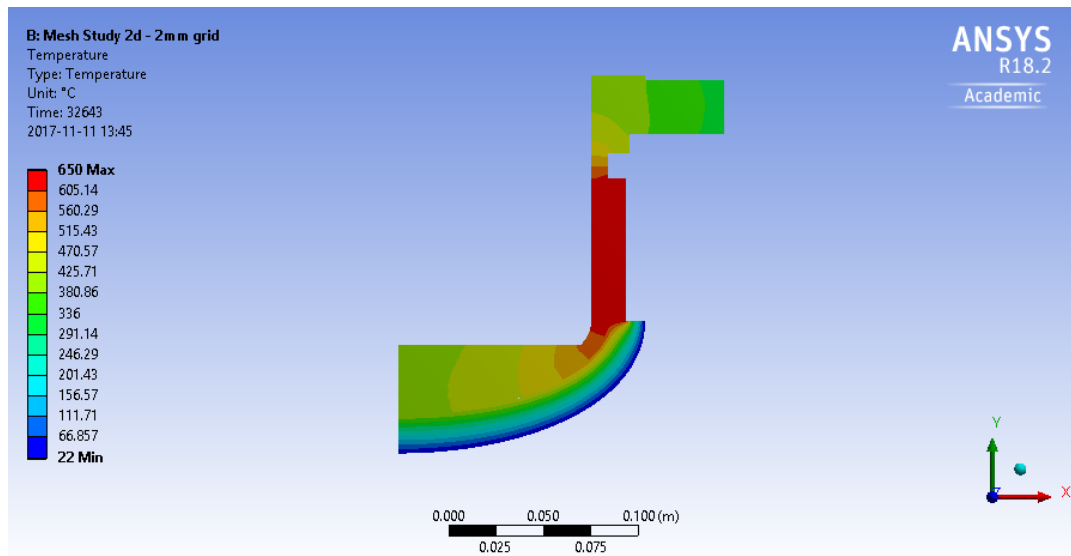


Figure 25: Temperature distribution inside the crucible with a band heater and 2.0 kg  $\text{CuCl}$ ,  $0.5 \text{ W m}^{-2}\text{K}^{-1}$  surface convection coefficient.

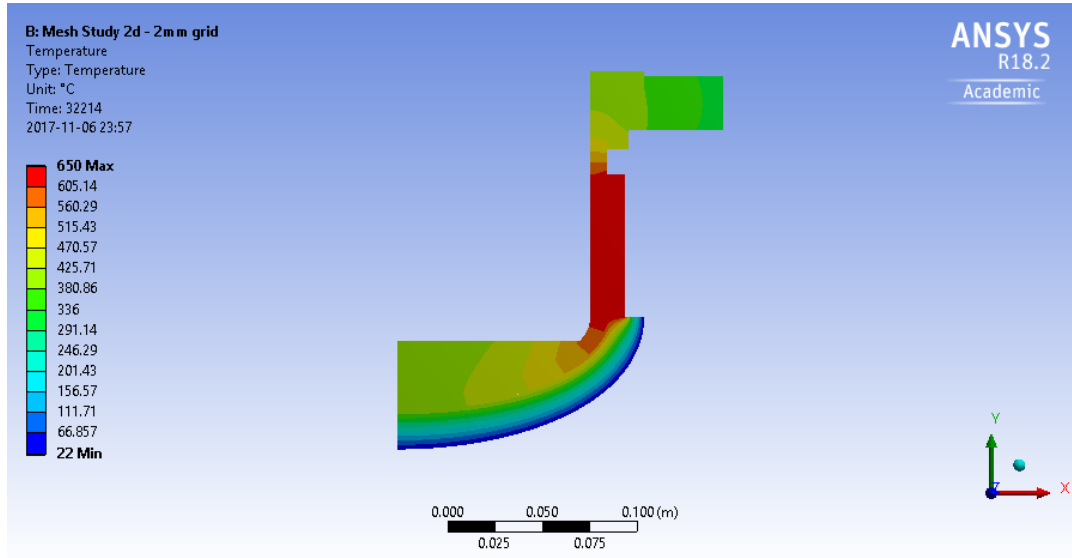


Figure 26: Temperature distribution inside the crucible with a band heater and 2.0 kg CuCl,  $1 \text{ W m}^{-2}\text{K}^{-1}$  surface convection coefficient.

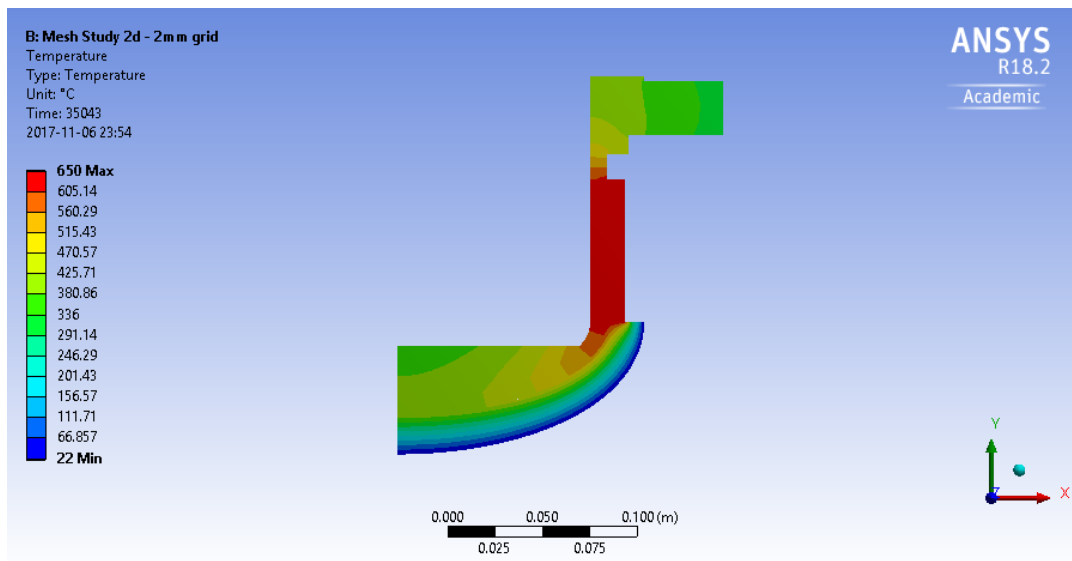


Figure 27: Temperature distribution inside the crucible with a band heater and 2.0 kg CuCl,  $2 \text{ W m}^{-2}\text{K}^{-1}$  surface convection coefficient.

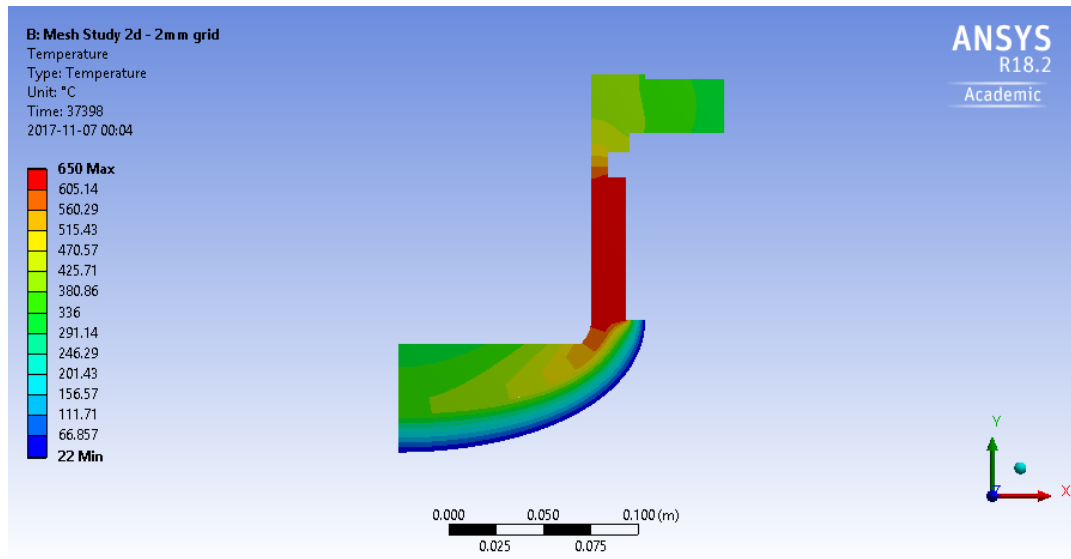


Figure 28: Temperature distribution inside the crucible with a band heater and 2.0 kg CuCl,  $4 \text{ W m}^{-2}\text{K}^{-1}$  surface convection coefficient.

A second set of thermal simulations was completed with the addition of an evenly distributed 150W heating surface under the crucible and a temperature set point of  $650^{\circ}\text{C}$ . These temperature distributions are shown in Figure 29-27. The addition of a heating surface at the base improved the heating performance by increasing the CuCl surface temperature of the molten salt to satisfy decomposition, and by reducing the time to obtain a stable top surface temperature.

At the lowest simulated convection rate of  $1.0 \text{ Wm}^{-2}\text{K}^{-1}$  with two heating sources set to  $650^{\circ}\text{C}$ , the lowest surface temperature in the CuCl was  $599^{\circ}\text{C}$ . Temperatures in excess of  $530^{\circ}\text{C}$  will produce CuCl vapor quickly, which must be minimized. Measuring the temperature in the center and at the wall can allow a precise control of the CuCl temperatures by allowing the two heating surfaces to operate at independent set points. Reducing the set point temperatures will help satisfy the preferred decomposition temperatures.

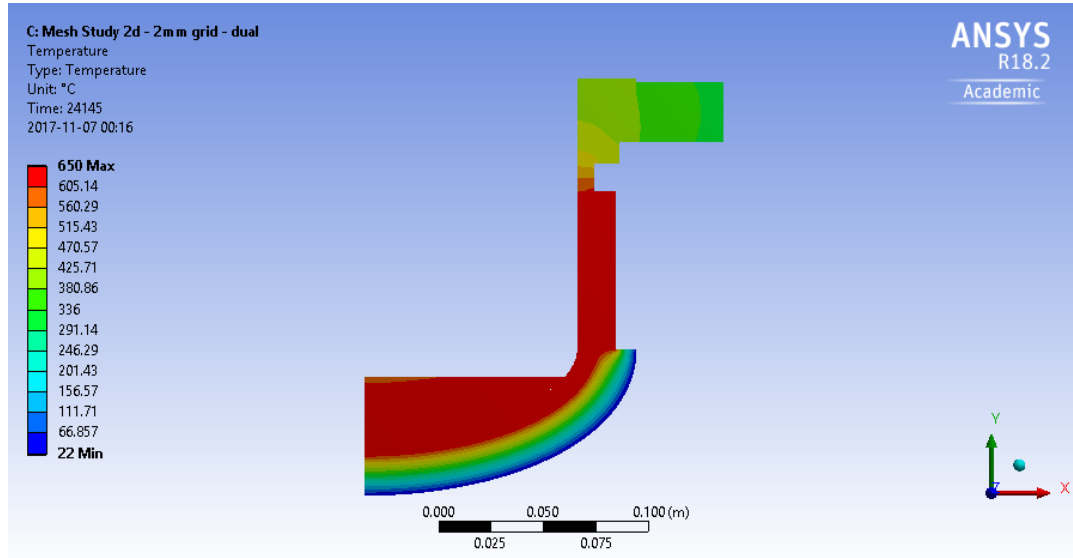


Figure 29: Temperature distribution inside the crucible with dual heaters and 2.0 kg CuCl,  $1 \text{ W m}^{-2}\text{K}^{-1}$  surface convection coefficient.

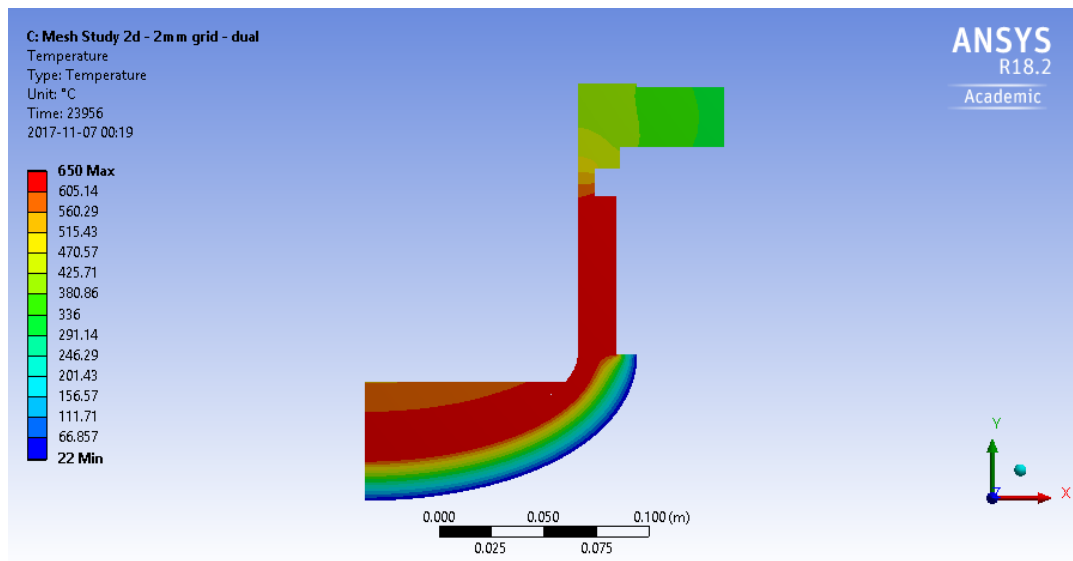


Figure 30: Temperature distribution inside the crucible with dual heaters and 2.0 kg CuCl,  $2 \text{ W m}^{-2}\text{K}^{-1}$  surface convection coefficient.

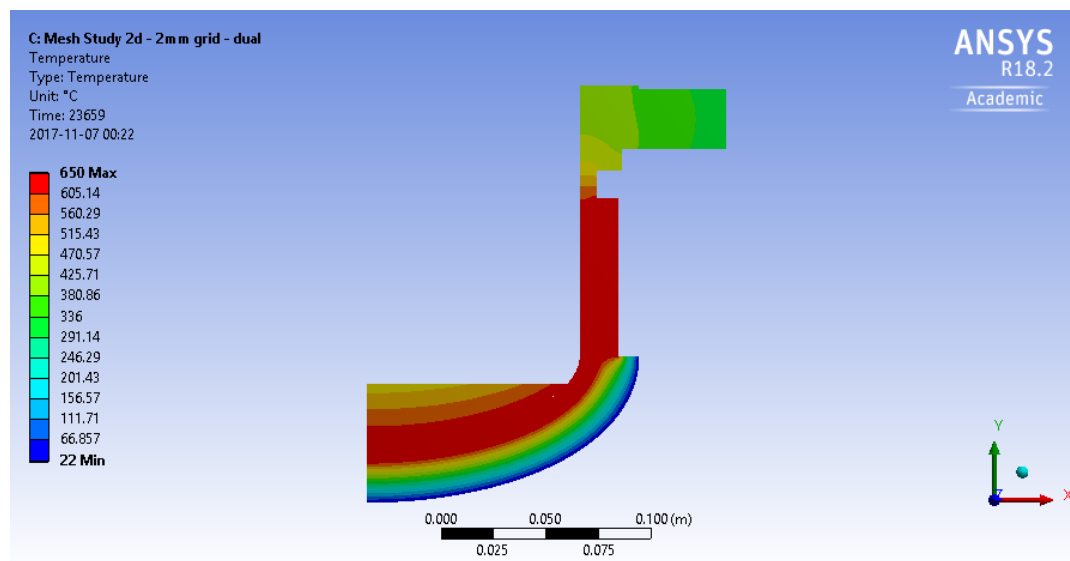


Figure 31: Temperature distribution inside the crucible with dual heaters and 2.0 kg CuCl,  $4 \text{ W m}^{-2}\text{K}^{-1}$  surface convection coefficient.

In these simulations, as the convection coefficient was increased the surface temperature at the center of molten salt decreased. The dual heating configuration is preferred, however, because thermolysis reactor can attain the required temperature for  $\text{CuO} \cdot \text{CuCl}_2$  decomposition.

Additionally, both sets of simulations confirmed that the thermal conductivity through CuCl is poor. The addition of a heating source to the base greatly improved the rate of heat transfer into the CuCl center. The resistance path from the base heater to the top surface was shortened, compared to the path along the surface, thereby increasing the average temperature in the CuCl.

The minimal surface temperatures and time to a steady state are summarized in Table 9 for each simulated case. The surface temperature must be kept above the melting point of CuCl at the very least to prevent accumulation of reactants on the surface. Table 9 shows that the time to a stable temperature decreases with increased convection rates. This occurs because the equilibrium of energy flow to and from the thermolysis reactor is attained sooner.

Table 9: Simulation convection coefficients and surface temperatures, 2.0kg CuCl, single (1-4) and dual heating (5-7) zones.

| <b>Simulation Case</b> | <b>Convection Rate<br/>[Wm<sup>-2</sup>K<sup>-1</sup>]</b> | <b>Time to Stabilize<br/>[s]</b> | <b>Centre Top<br/>Temperature [C]</b> |
|------------------------|--|----------------------------------|---------------------------------------|
| 1                      | 0.5  | 32643                            | 411                                   |
| 2                      | 1  | 32214                            | 390                                   |
| 3                      | 2  | 31443                            | 354                                   |
| 4                      | 4  | 30198                            | 303                                   |
| 5                      | 1  | 24154                            | 599                                   |
| 6                      | 2  | 23956                            | 557                                   |
| 7                      | 4  | 23695                            | 487                                   |

Plots showing the temperature rise at the wall and bottom of the CuCl with only a band heater are shown in Figure 32 and Figure 33. Because of the poor conduction path through the stainless steel in the axial direction, the temperature at the base is very close to the surface temperature for each corresponding case, but the difference increases as the convection rate is increased, up to 22°C between 0.5 and 4.0 Wm<sup>-2</sup>K<sup>-1</sup> surface convection rates.

At the wall, the stabilized temperature between varying convection rates only varied by 6°C. Due to the short thermal path, this temperature was observed to be a lot more stable than at the base of the crucible. In the simulations with dual heaters at 2.0kg and 10.35kg, the interior wall temperature adjacent to the heaters attained the set points of 650°C within 3600 seconds.

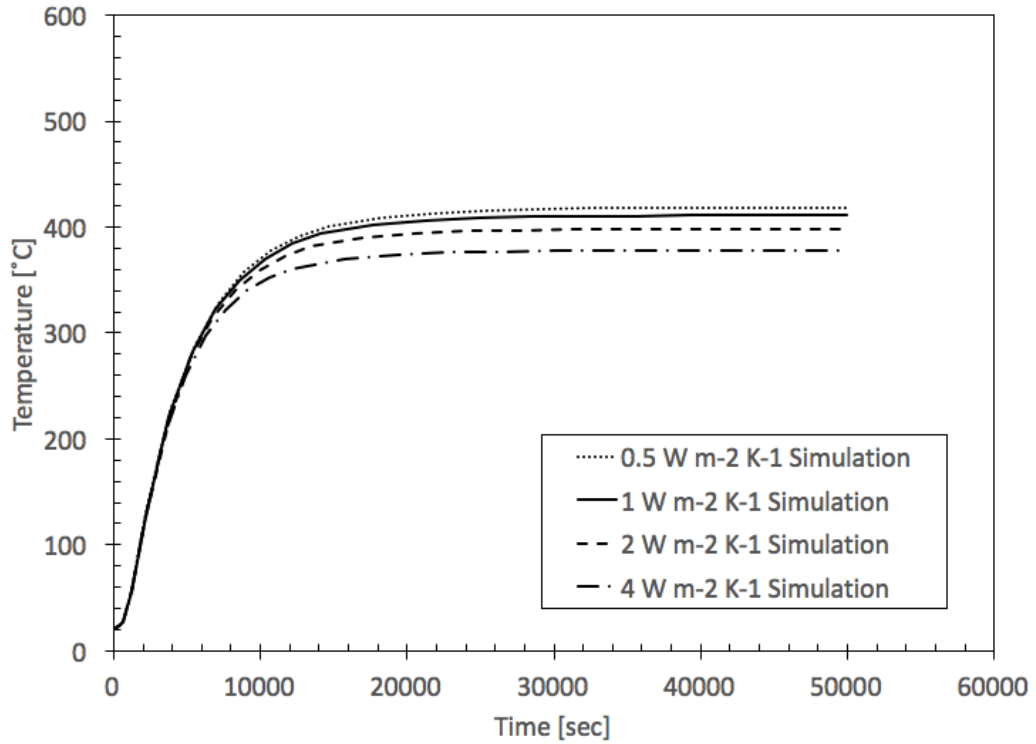


Figure 32: Bottom-center temperature at 2.0kg CuCl at 0.5, 1.0, 2.0 and 4.0 Wm<sup>-2</sup>K<sup>-1</sup>.

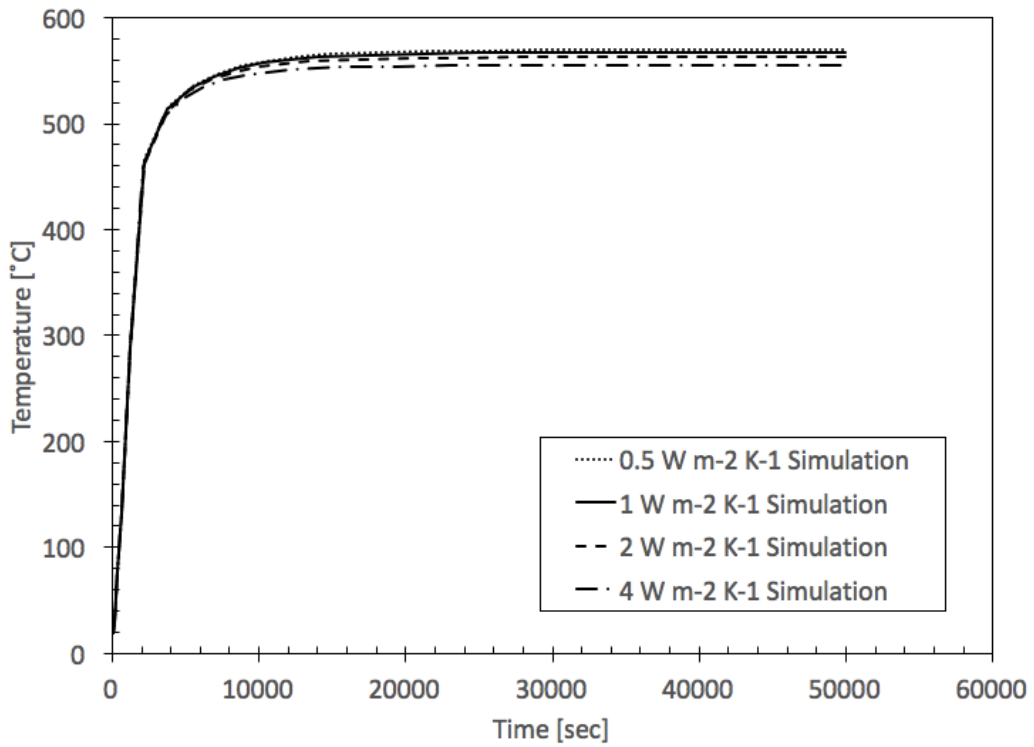


Figure 33: Wall-CuCl top surface interface temperatures with 2.0kg CuCl at 0.5, 1.0, 2.0 and 4.0 Wm<sup>-2</sup>K<sup>-1</sup>.

Temperature distributions with a CuCl mass of 10.35kg are presented in Figure 34, Figure 35 and Figure 36. These figures show that the configuration was able to reach the critical temperature range for decomposition in the scenario with a convection coefficient of  $1.0 \text{ Wm}^{-2}\text{K}^{-1}$ . The surface temperature at the center was  $538^\circ\text{C}$ . In the remaining two cases, the surface temperatures were below  $480^\circ\text{C}$  at the center.

#### 4.1.2 TEMPERATURE DISTRIBUTION WITH 10.35KG

With the larger mass, the heating time increased as surface convection rates increased. The temperature distribution throughout the reactor is shown in Figure 34, Figure 35 and Figure 36 at each convection rate. Unlike the simulations with 2.0kg, here only the low convection rate of  $1.0\text{Wm}^{-2}\text{K}^{-1}$  allows the decomposition reaction to occur throughout. Similar to the previous simulations, an increase in surface convection rates reduced the top-center temperatures, which are summarized in

Table 10 along with the duration, in seconds, to attain a stable temperature at the surface.

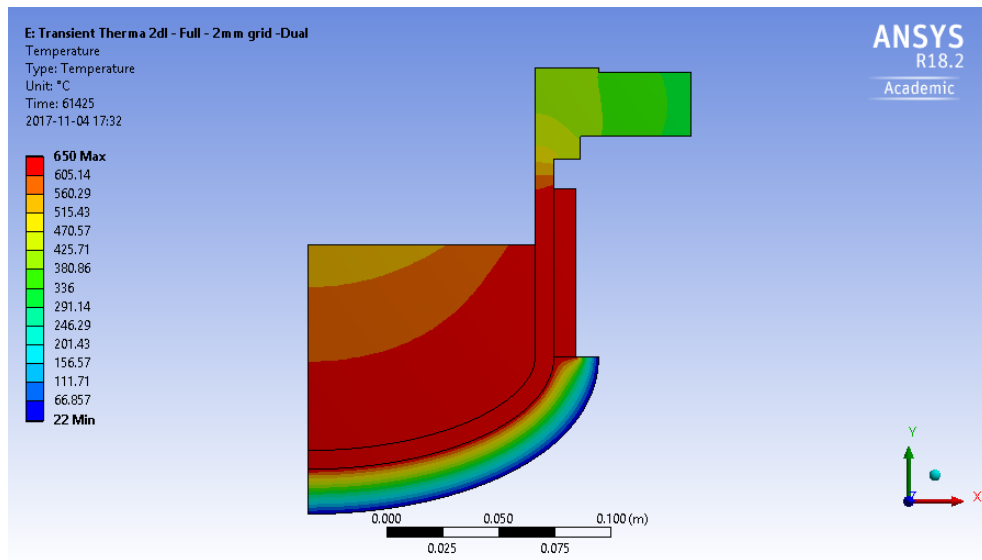


Figure 34: Temperature distribution inside the crucible with dual heaters and 10.35 kg CuCl,  $1 \text{ W m}^{-2}\text{K}^{-1}$  surface convection coefficient.

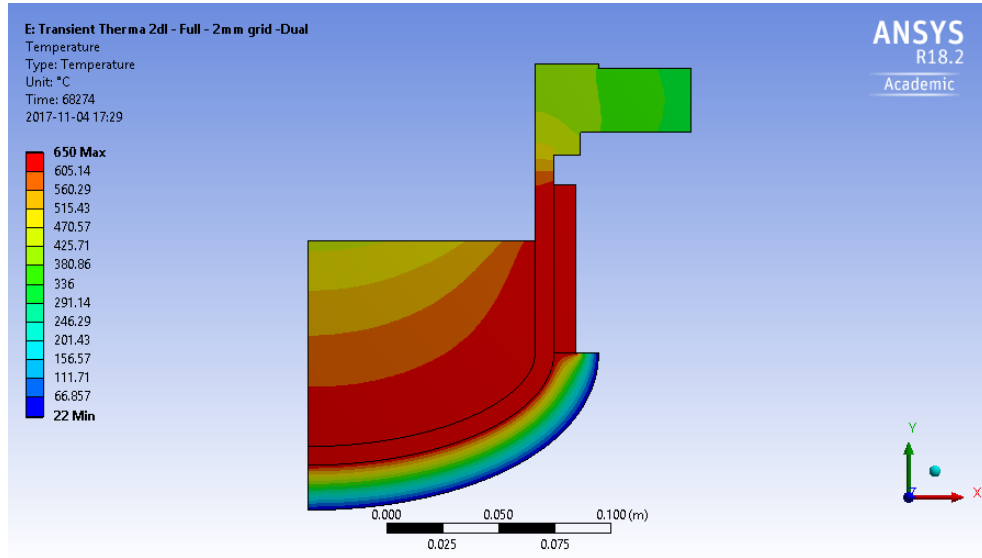


Figure 35: Temperature distribution inside the crucible with dual heaters and 10.35 kg CuCl,  $2 \text{ W m}^{-2}\text{K}^{-1}$  surface convection coefficient.

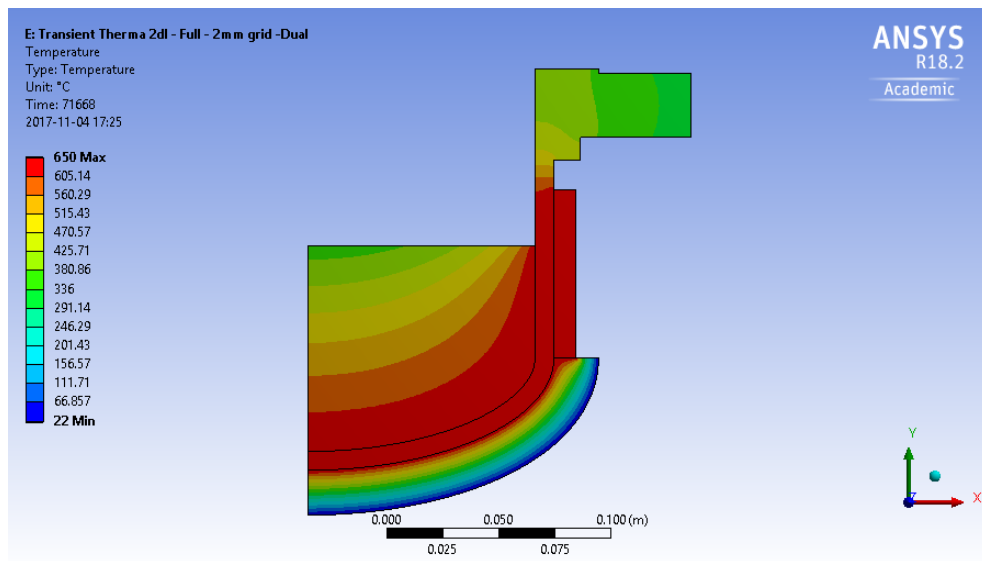


Figure 36: Temperature distribution inside the crucible with dual heaters and 10.35 kg CuCl,  $4 \text{ W m}^{-2}\text{K}^{-1}$  surface convection coefficient.

Table 10: Simulation convection coefficients and surface temperatures, 10.35 kg CuCl, dual heaters (8-10).

| Simulation Case | Convection Rate<br>[Wm <sup>-2</sup> K <sup>-1</sup> ] | Time to Stabilize<br>[s] | Centre Top<br>Temperature [C] |
|-----------------|--|--------------------------|-------------------------------|
| 8               | 1  | 61425                    | 538                           |
| 9               | 2  | 68274                    | 459                           |
| 10              | 4  | 71668                    | 359                           |

Simulated temperature rise curves are presented in Figure 37 to Figure 39. Each graph depicts the temperature at the CuCl surface as a function of time. The single and dual heat source curves have similar start-up profiles; however, the dual heat source is faster and plateaus at a higher temperature. In the case of a full reactor with 10.35 kg of CuCl, the start-up process is beyond 50000 seconds – approximately 2.5 times longer than a reactor with 2.0 kg of CuCl.

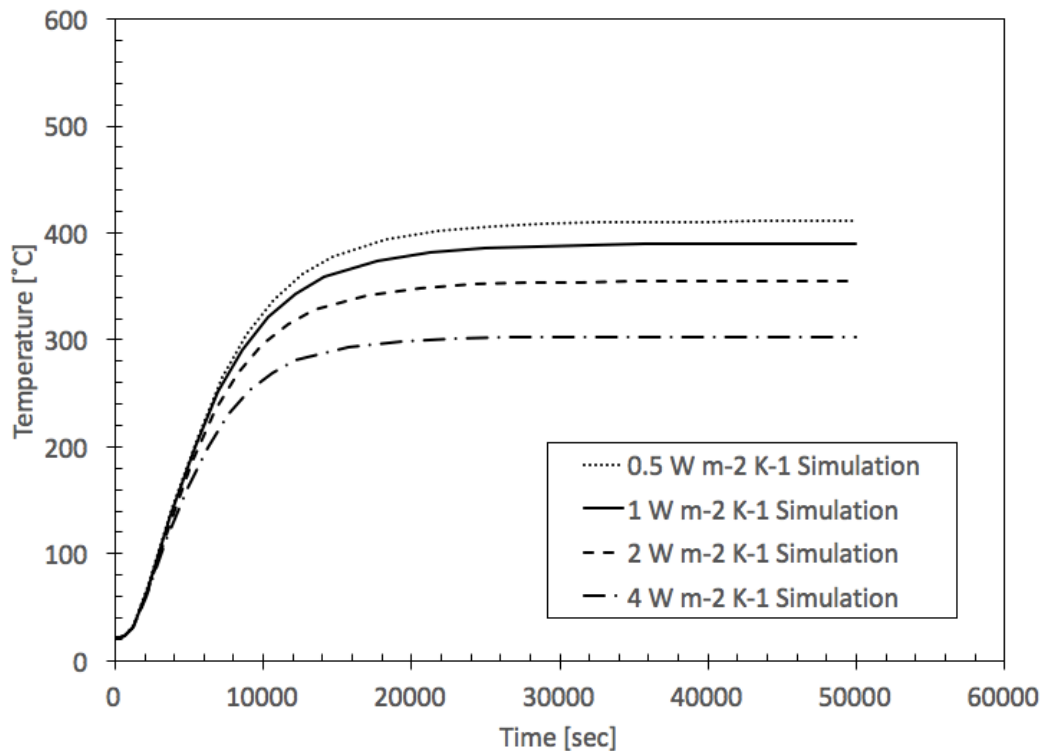


Figure 37: Single heater temperature rise, 2.0 kg CuCl.

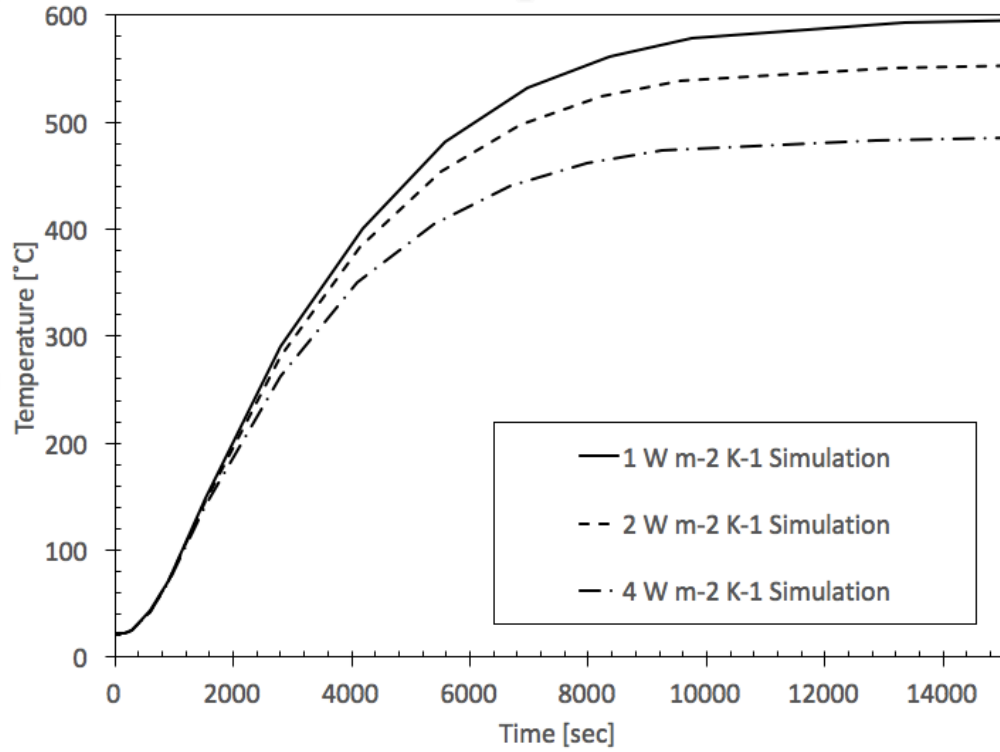


Figure 38: Dual heater temperature rise, 2.0 kg CuCl.

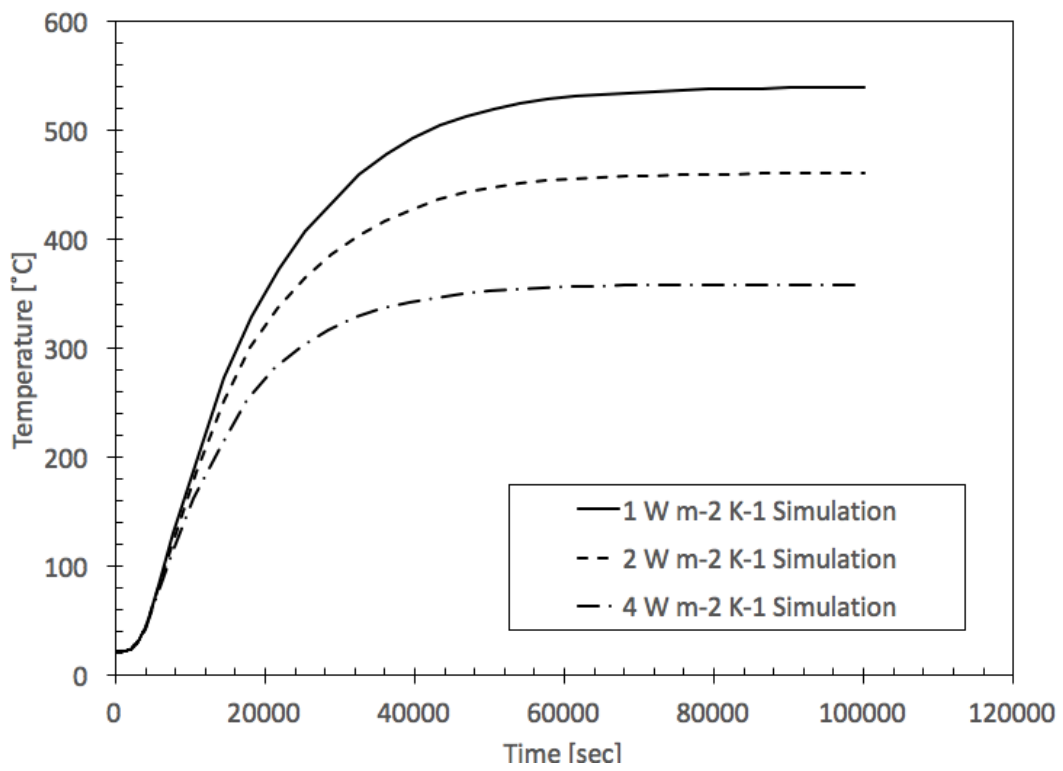


Figure 39: Dual heater temperature rise, 10.35 kg CuCl.

Heat flow along the top surface produces a significant thermal gradient. Unfortunately, the temperature at the wall is beyond the stable temperature of CuCl. That is, the temperature is beyond  $600^{\circ}\text{C}$  in cases with low surface convection. Elevated temperatures of molten CuCl produce a high vapor pressure, which is unfavorable to downstream equipment. Minimizing the temperature drop from the wall to the center of the vessel requires a reduction in crucible diameter.

#### 4.1.3 REDUCED TEMPERATURE SET-POINT WITH 2.0KG CUCL

The 2.0kg thermal model with dual heaters was modified by setting the heater set point temperature to  $530^{\circ}\text{C}$  to verify that the temperature at the center of the surface would sustain decomposition. With the reduced temperature setting, the time to a stabilized temperature is reduced to 17001 seconds. The temperature at the center of the surface is  $489^{\circ}\text{C}$ , satisfying the thermal conditions for decomposition. Additionally, the temperature increases quickly below the surface: 10 mm below the surface the CuCl temperature is  $498^{\circ}\text{C}$ .

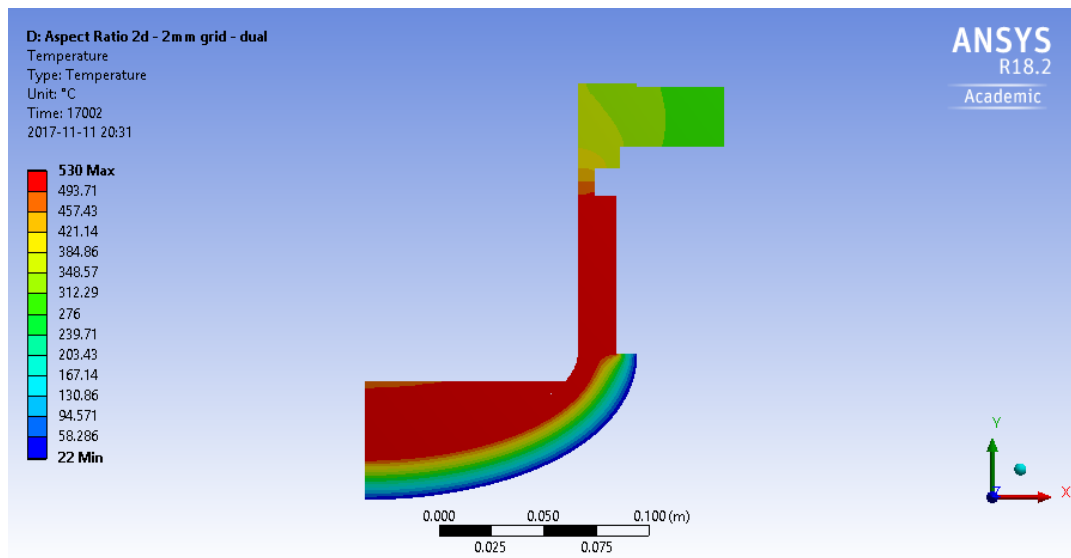


Figure 40: Modified dual heater with  $530^{\circ}\text{C}$  set point, 2.0kg CuCl  $1.0 \text{ Wm}^{-2}\text{K}^{-1}$ .

## 4.1.4 SURFACE TEMPERATURE DISTRIBUTIONS AND REDUCED REACTOR SIZE

Surface temperature plots were created from each study to compare the rate of temperature change from the center of the reactor to the wall. The data was collected from simulations with  $650^{\circ}\text{C}$  heater set points.

Figure 41 displays surface temperature data for 2.0kg of CuCl in the thermolysis reactor. It shows a smooth decrease in temperature from the wall towards the center of the reactor. As the convection rate increases, the rate of change is increased. The temperature at the wall was  $649^{\circ}\text{C}$  for all three cases, which is nearly the heater set point. The variance between temperatures at the center ranges between  $480^{\circ}\text{C}$  and almost  $600^{\circ}\text{C}$ .

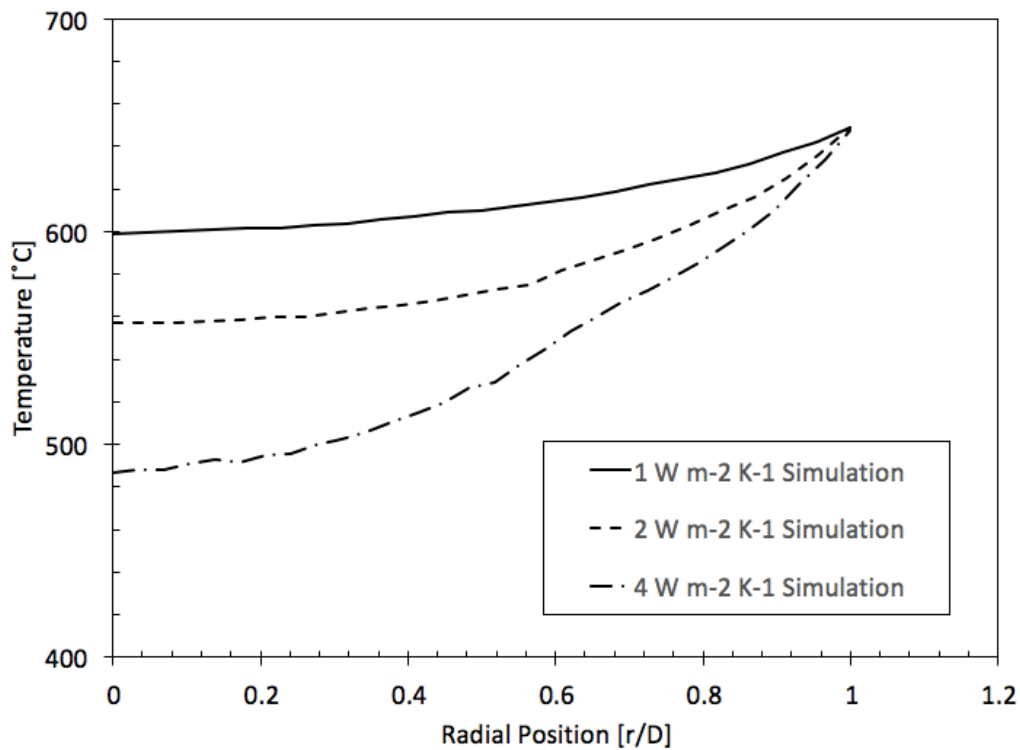


Figure 41: CuCl top surface temperature distribution with 2.0kg.

In Figure 42, the surface temperature with a 10.35kg mass of the CuCl is shown. It has a larger temperature change from the wall to the center of the reactor. The temperature at the wall is 649°C like in the previous surface distribution. However, the variance is much larger: the temperature ranges from 380°C to 525°C, which occur at 4 and 1  $\text{Wm}^{-2}\text{K}^{-1}$ , respectively. The increased distance from the heated surfaces is the cause of the increased thermal losses at the surface.

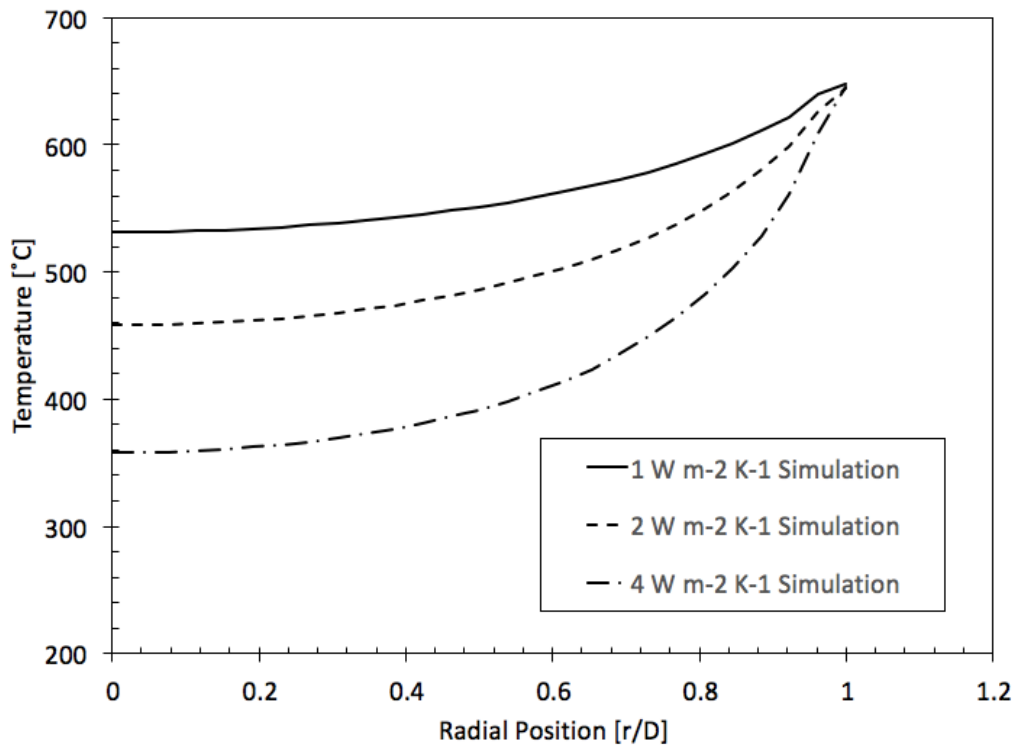


Figure 42: CuCl top surface temperature distribution with 10.35kg.

#### 4.1.5 SUMMARY

Heater locations are crucial to maintaining a stable operating point within the thermolysis reactor. These simulations have shown that a dual heater configuration will be sufficient to raise the temperature within the reactor, and will keep the CuCl below 530°C at the interior wall if the heater set points are modified.

One limitation of these simulations is the lack of fluid mixing in the molten salt. The salt will melt from the crucible wall inward to the center, and during this time there will be internal movement of the salt. The model, however, is not configured to include a phase change from the solid to liquid phase: the CuCl is considered as a solid with variable properties to account for transition to a molten phase. For this reason, it is likely that mixing of the CuCl during melting will decrease the startup time of the reactor.

#### 4.2 THERMOLYSIS REACTOR EXPERIMENTS- ISO-HEAT 493

Prior to operation of the thermolysis reactor with CuCl, the thermolysis reactor was tested with a stable industrial quenching salt. The selected salt compound was ISO HEAT 493 obtained from Park Thermal Industrial Corporation. The salt is a proprietary mixture of calcium, barium, potassium and sodium chloride. It is commonly used for quenching, annealing or hot working of tool steels. The main reason for using this salt mixture was that it has a very low vapor pressure compared to CuCl. The mixture is, however, hygroscopic and a gradual heating profile was required to slowly evaporate all moisture.

While the salt is in granular form, water vapor can pass around the particles and leave the reactor as the reactor is heated. However, if the salt was previously heated beyond the melting point and cooled in a humid environment, the hygroscopic quality of the salt mixture may draw the moisture deep into the solidified salt. Should a subsequent heating profile be too aggressive, moisture trapped in the interior may cause the solidified salt to

fracture explosively. In the constructed apparatus, the wall thickness of the crucible will keep the operator safe if an even like this occurs. In addition, the heating system is not capable of generating an aggressive heating profile which would lead to fractures. Therefore, the probability associated with this occurrence is very low.

Properties of ISO HEAT 493 are moderately different from CuCl. The melting point of the mixture is 493°C, the specific heat is 0.27 kJ kg<sup>-1</sup>, and the molten density of 2.40 g cm<sup>-3</sup> is reported at 871°C. However, a more detailed description of thermodynamic properties was not provided by the supplier. This limitation does not allow for extensive thermal study in the thermolysis reactor with ISO HEAT 493.

Heating profiles are shown in Figure 43 and Figure 44 of granular and solid initial states, respectively. In both tests, a smooth temperature rise was observed. Heating a solidified salt was faster than heating granular salt.

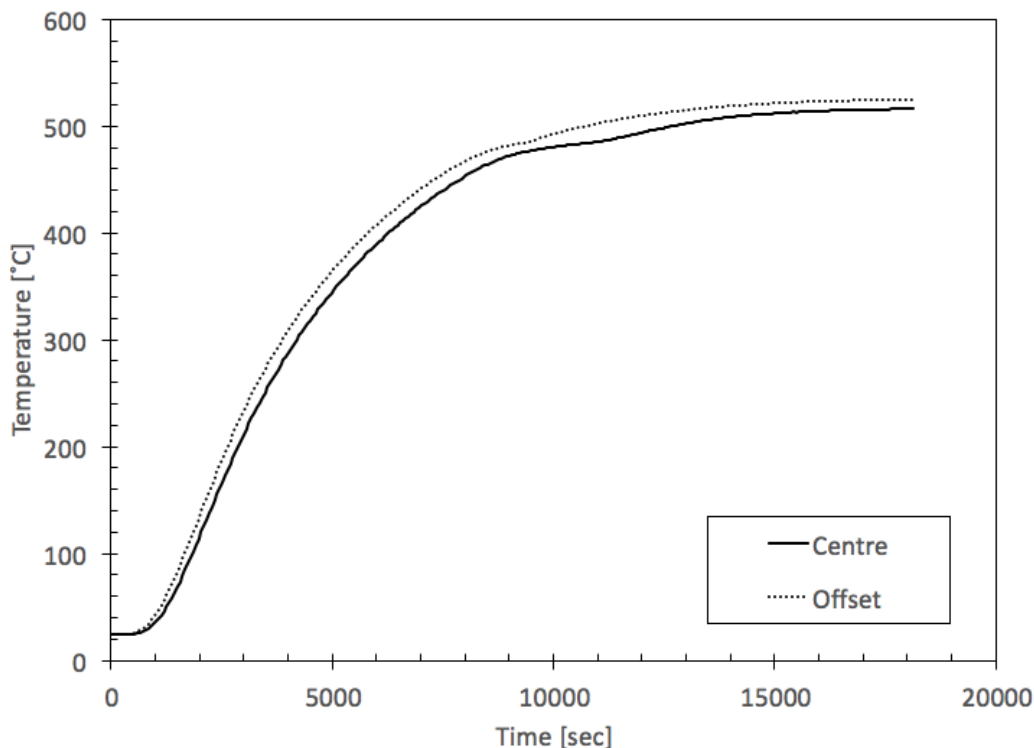


Figure 43: Single heater temperature rise, 2.0 kg granular ISO HEAT 493.

Thermocouples were located at the bottom center of the salt and 50mm offset from center. The heat conduction path from the band heater to the center of the thermolysis reactor is longer compared to the offset thermocouple location. Two thermal conductivity paths to the center are available in the thermolysis reactor: through the stainless-steel crucible and through the CuCl. The conductivity path of least resistance is through the stainless-steel due to the higher thermal conductivity of the material. A small temperature drop is seen between the center and offset thermocouples, which is accounted by the associated thermal resistance.

In the design of a full-scale reactor, heat must be readily distributed within the reactor and CuCl to prevent prolonged heat-up times. Integration of the cycle with nuclear reactors has been previously proposed by Naterer *et al.* [8]. Thermal energy from the nuclear process may be transferred to the thermolysis reactor via a hot gas, such as helium. However, a jacketed baffled heat exchanger on the exterior of the thermolysis reactor may not be sufficient

to effectively heat the CuCl, as indicated by the initial testing. Available heat in the high temperature gas will require a more direct heat transfer path into the molten salt. This may be accomplished with the use of internal coiled tubes to improve heat transfer directly into the CuCl.

Thermal insulation placed around the crucible and band heater prevented unnecessary heat loss from the apparatus during testing. Without this insulation, the apparatus would not be able to reach the desired temperature.

Differences in final temperature between the two tests were attributed convective heat loss on the exterior of the thermolysis reactor. The first test had thicker insulation on the top of the reactor, which reduced thermal losses.

Upon completion of the tests, the internal surfaces of the reactor were examined, and no deposition of material was observed on the side walls. This is explained by the very low vapor pressure of ISO HEAT 493 salt.

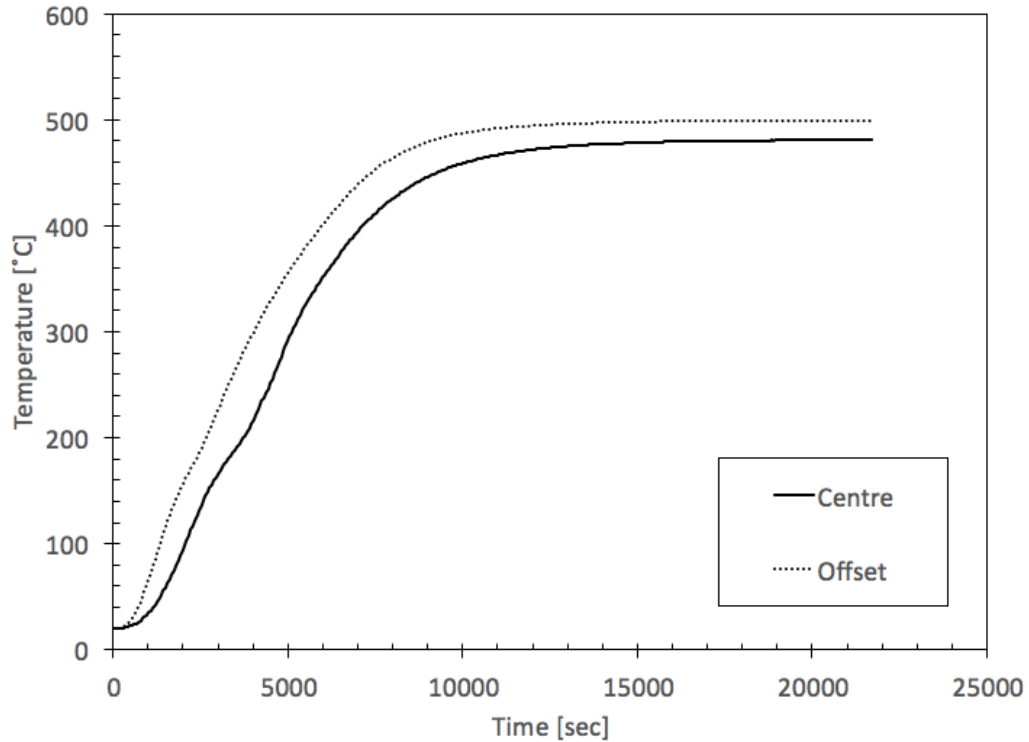


Figure 44: Single heater temperature rise, 2.0 kg solid ISO HEAT 493.

### 4.3 THERMOLYSIS REACTOR EXPERIMENTS - $\text{CuCl}$

Experimental work with  $\text{CuCl}$  was conducted using a procedure similar to the experimentation with ISO HEAT 493. A comparison of simulated and experimental data with a single heat source configuration is plotted in Figure 45. There were two start-up conditions examined: first with granular salt and later with a solidified salt. The solidified salt experiment had a smooth temperature rise compared to the granular salt. On the other hand, the powdered  $\text{CuCl}$  had two steps before a smooth temperature rise was observed. The difference is attributed to shifting material within the reactor during heating of powder  $\text{CuCl}$ . The last step in the powdered  $\text{CuCl}$  experiment coincides with the melting point of  $\text{CuCl}$ , which is where material around the thermocouple sank and was replaced with molten  $\text{CuCl}$ .

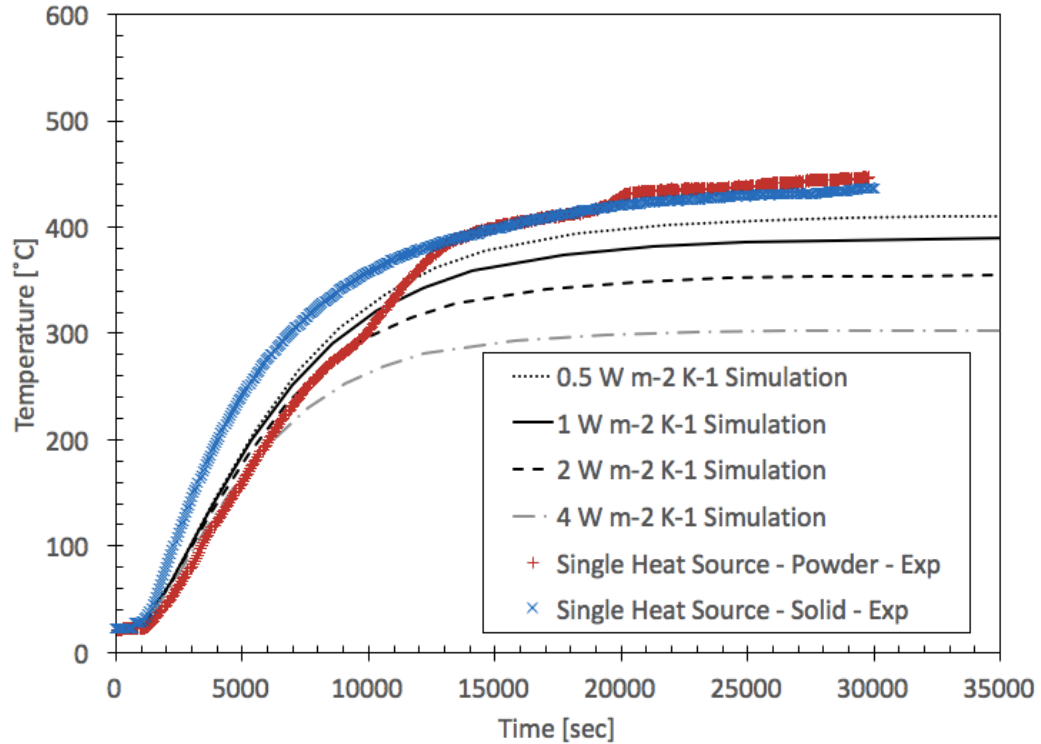


Figure 45: Comparison of surface temperatures between simulations and experimental data, single heat source at surface center, 2.0 kg CuCl.

Simulated and experimental data for a dual heat source configuration is shown in Figure 46. Here, the heat up rate is slower up to 430°C, which is where the CuCl becomes a liquid. Then it corresponds to a simulated surface convection rate between 2 and 4  $\text{Wm}^{-2}\text{K}^{-1}$ .

In the experimental setup, gas temperature above the surface of the molten salt was recorded to measure the temperature gradient between the molten salt and gas. The gas temperature was 70°C to 90°C lower than the top surface temperature. This means that even with an insulated reactor, heat losses in the phase separator section were observed. As a result, convective currents were present.

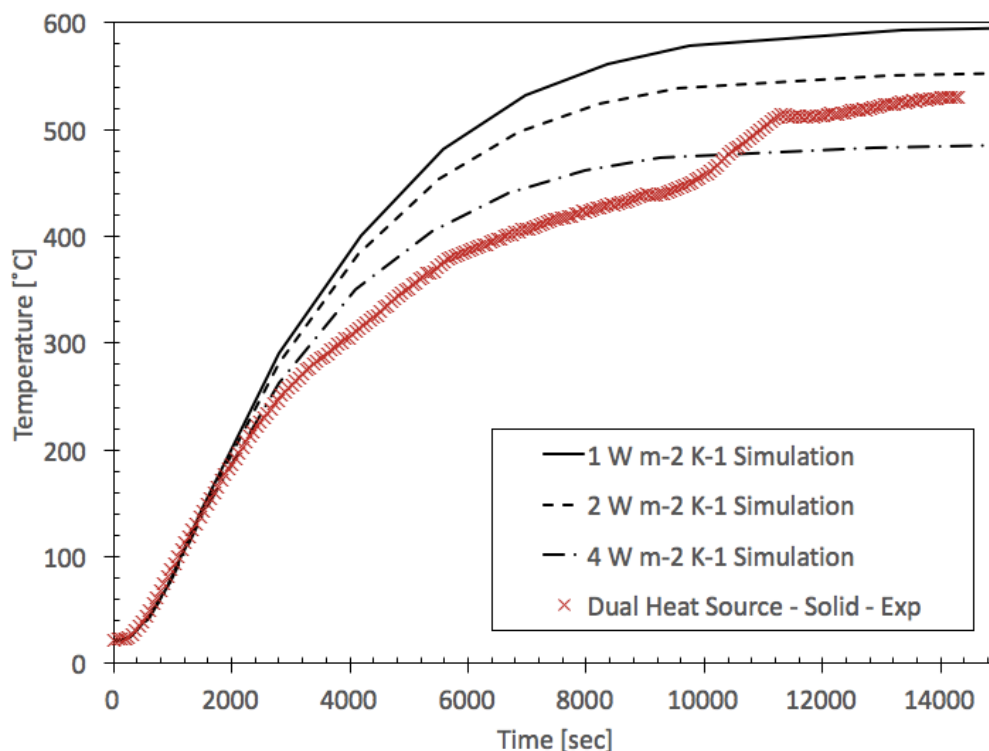


Figure 46: Comparison of heat up temperature between simulation and experimental data, dual heat source, 2.0 kg CuCl.

From the experiments with CuCl, it was concluded that a dual heat source system is preferred at start-up to reduce heating time to obtain a fully molten CuCl. The dual heater configuration will provide the necessary thermal conditions for decomposition to occur. Additionally, the use of a powdered or solidified CuCl has minimal consequence on start-up performance. Using powdered CuCl allows the solid material to mix and reduces heat up time slightly.

#### 4.4 SCRUBBER PH ANALYSIS

A sample from the scrubber solution was collected at the beginning and end of all testing with CuCl to determine if chlorine was recovered from the effluent gas. If  $\text{Cl}_2$  gas was present in the scrubber, it would be neutralized by basic solution. A starting pH 8.5 was recorded prior to operating the reactor with CuCl, and the final pH was 8.5. Therefore, no sequestering of  $\text{Cl}_2$  was observed during testing.

## 4.5 XRD ANALYSIS OF CRYSTALLINE FORMATION IN PHASE SEPARATOR

XRD analysis of crystalline structures was used to identify the species of salts which formed on the phase separator walls. XRD is a process by which the crystalline structure of a substance may be used to identify it. A collected sample is placed on a platform and a focused X-ray pulse is emitted at the sample. A detector will then rotate around the sample and record the cumulative pulses obtained at each angle,  $2\theta$  (Figure 47).

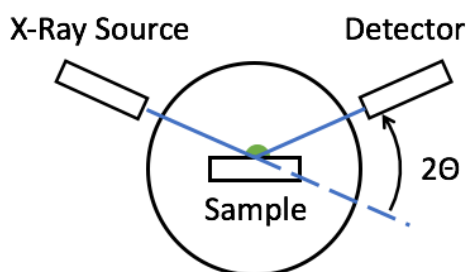


Figure 47: Orientation of X-ray source, sample and detector during XRD analysis.

Identifying the substance is accomplished by comparing the sample's diffraction profile with a database of known crystalline structure profiles. If the intensity peaks at specific angles match those of a material in the database, then the material may be identified.

If two or more crystalline structures are present, overlaying multiple database entries is necessary to identify the substances. The resultant diffraction graph is a sum of all diffraction patterns. Therefore, identification becomes more difficult as the number of structures increases and peaks may overlap or be lost in background noise.

Phases may also be identified using this process. A crystalline substance will generate sharp peaks at specific angles. An amorphous phase will appear as a wide band across a range of  $2\theta$ .

XRD was conducted using the Rigaku Ultima 4 with a  $3.00^\circ$  per minute scan speed and a scan step of  $0.02^\circ$ . The diffraction was recorded between  $10^\circ$  and  $90^\circ$ . Samples were ground prior to conducting the analysis.

A sample of the crystalline formation collected from the sidewall of the phase separation section (Figure 51) was analyzed using XRD and the results are seen in Figure 48. The peak locations coincide with a profile for CuCl. However, the relative intensity of the largest peak is much higher than in the reference diffraction profile. This is most likely a result of internal crystalline stresses or a preferred orientation of the ground sample.

The crystalline formation on the side wall is indicative of a condensing CuCl vapor, which is present near the surface of the molten CuCl. Even though the reactor is purged with  $N_2$  gas at the beginning of the reactor, the heavier CuCl vapor fills the reactor. In addition, the separator walls were not heated, but only insulated on the exterior. The reduced temperature of the phase separator walls provoked the formation of crystals.

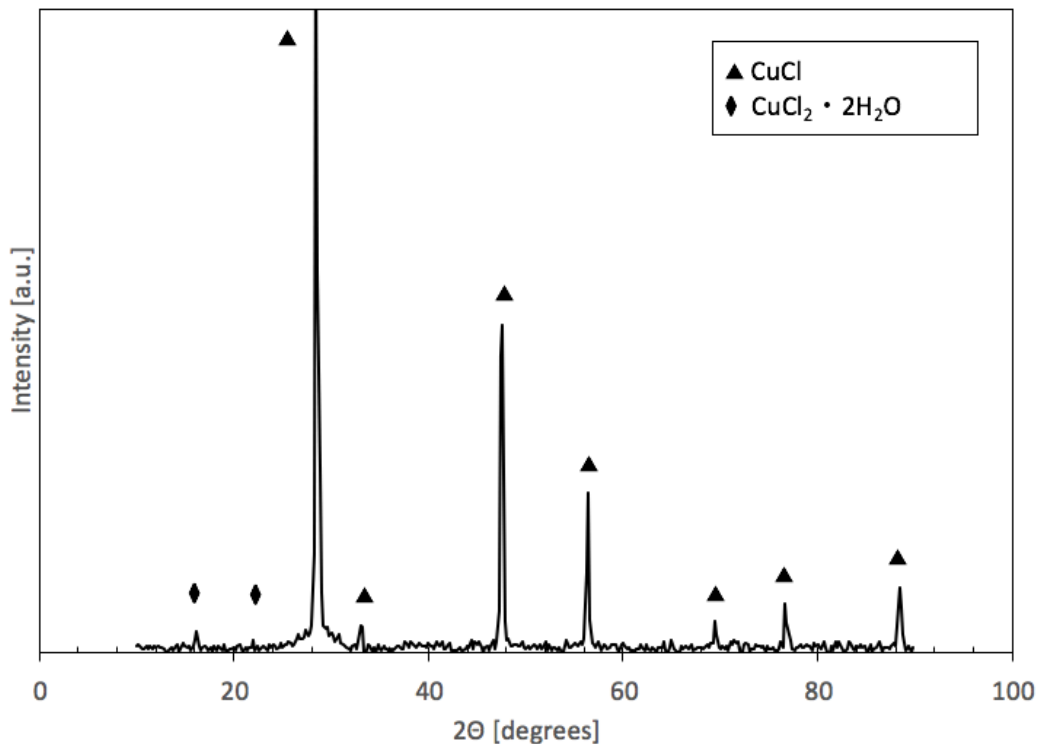


Figure 48: XRD analysis of sample from phase separator side wall.

Another sample from the phase separator top wall was also analyzed using XRD. This diffraction profile is seen in Figure 49. On the top surface the structure and physical appearance of the vapor deposits were significantly different. Rather than an off-white rough and serrated crystalline formation, a pale-blue and smooth deposit was observed. Based on the different physical appearance alone, two or more crystalline species were expected. The diffraction pattern was composed of peaks representing CuCl and CuCl<sub>2</sub> dihydrate. It is probable that the hydration of CuCl<sub>2</sub> occurred from the atmospheric water vapor or after the sample was collected since the salt is known to be highly hygroscopic.

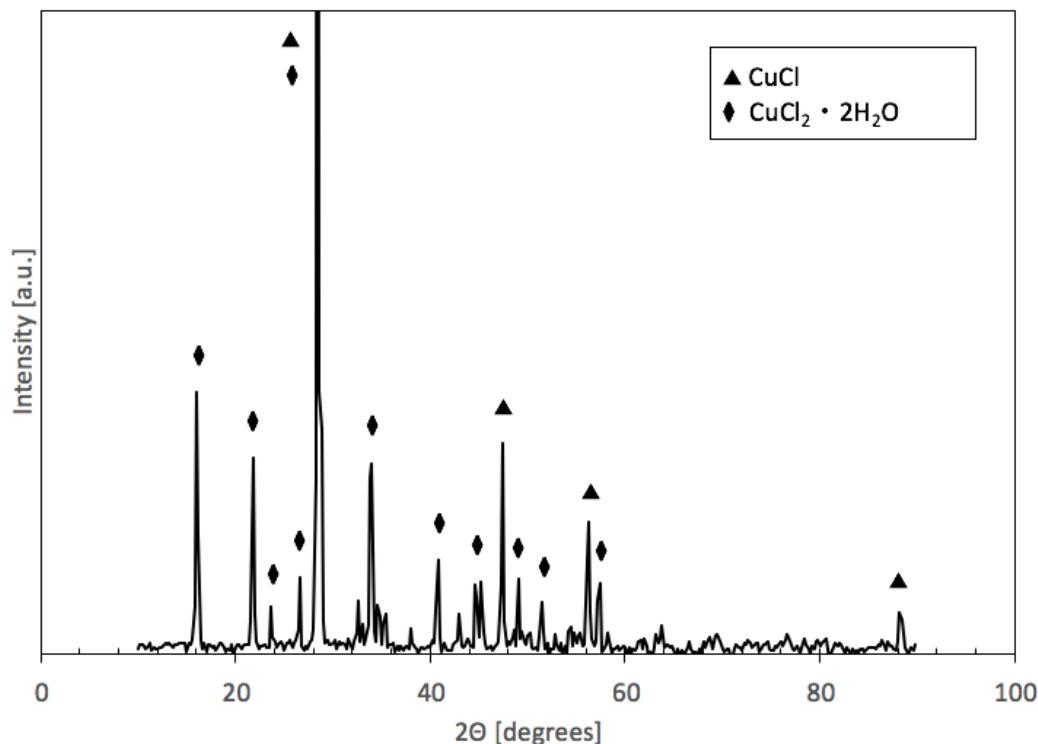


Figure 49: XRD analysis of sample from phases separator top cover.

To avoid formation of crystals above the crucible, the surface temperature of the entire reactor must be kept above  $430^{\circ}\text{C}$ . However, the removal of  $\text{CuCl}$  vapors from the effluent flow will have to be accomplished downstream of the reactor to ensure high purity  $\text{O}_2$  gas. A condenser maintained below the melting point of  $\text{CuCl}$  should be used with single or multiple mesh filters. This will avoid scaling of the gas transfer piping.

#### 4.6 UNCERTAINTY ANALYSIS IN EXPERIMENTAL MEASUREMENTS

Evaluating the uncertainty of experimental observations is required to maintain a high level of confidence in derived relationships and allow meaningful repetitions of the experiment. Using the method outlined by Kline and McClintock [60], the uncertainty associated with each sensor and digitizing element was evaluated.

The uncertainty,  $U$ , of an experimental observation is a combination of precision limit,  $P$ , and bias limit,  $B$ , and is expressed using a root-sum-square (RSS):

$$U = \sqrt{P^2 + B^2} \quad (29)$$

Precision limits are evaluated as twice the standard deviation of collected data from each sensor at an operational steady state. Bias limit is obtained from the manufacturer of the device and represents a fixed error. For the data acquisition system components, the bias is determined by taking the RSS of the gain error, offset error, and any other error associated with the operation of the device (e.g. calibration error). Precision for the data acquisition modules is assumed to be negligible compared to the magnitude of the combined gain and offset error.

In a custom-built data acquisition system, it is common for the sensor and digitizing device to have discrete errors. These errors must be merged to evaluate a combined uncertainty prior to utilizing the values in equations by using the RSS method. The combined uncertainty for data acquisition components (i.e. the last three items in Table 11) represent the sensor error in unison with the analog to digital conversion error.

When function,  $R$ , calculates a result using all or a subset of the values in Table 11, a propagation analysis must be performed on  $R$  to obtain the uncertainty, where  $R$  is a function of  $n$  variables,  $v$ :

$$R = f(v_1, v_2, v_3, \dots, v_n) \quad (30)$$

Table 11: Instrument Precision and Bias limits for sensors, ADC modules, and combined sensor and modules.

| <b>Instrument</b>                 | <b>Operational Range</b> | <b>Instrument Precision</b> | <b>Instrument Bias</b> | <b>Combined Uncertainty</b> |
|-----------------------------------|--------------------------|-----------------------------|------------------------|-----------------------------|
| Pressure Sensor<br>Current Output | ± 103.4kPa               | 1.19%                       | 1.00%                  | 1.55%<br>Sensor Only        |
| Thermocouple<br>Type K            | 0-800°C                  | 0.13%                       | 0.75%                  | 0.76%<br>Sensor Only        |
| Load Cell<br>Voltage Output       | 150kgF                   | 0.02%                       | 0.14%                  | 0.14%<br>Sensor Only        |
| NI 9203<br>Current ADC            | 0-20mA                   | -                           | 0.85%                  | 1.77%                       |
| NI 9211<br>TC ADC                 | 0-800°C<br>(Type K)      | -                           | 0.38%                  | 0.85%                       |
| NI 9215<br>Voltage ADC            | ±10V                     | -                           | 1.33%                  | 1.34%                       |
| PHH-103A<br>pH Meter              | pH 0-14                  | 0.41%                       | 0.14%                  | 0.43%                       |

In this case, the sensitivity of the result relative to each variable will influence the combined uncertainty. If  $R$  is linear with  $i$  variables that are independent and normally distributed, the precision uncertainty and bias uncertainty of function  $R$  are defined as:

$$P = \sqrt{\sum \left(\frac{\partial R}{\partial v_i}\right)^2 P_i^2} \quad (31)$$

$$B = \sqrt{\sum \left(\frac{\partial R}{\partial v_i}\right)^2 B_i^2} \quad (32)$$

Once the partial derivatives are calculated for precision and bias, the values are summed using RSS to produce the equation uncertainty. Verifying the uncertainty *in situ* through baseline sensor measurement is recommended to

ensure all aspects of error analysis have been considered. It also further validates sensor functionality and correct placement.

Position error estimates for thermocouples were also calculated based on variance in the simulations in the lateral and vertical directions. A close-up of the top surface is shown in Figure 50. The temperature difference along the horizontal surface was  $1.13^{\circ}\text{C}$  at 10mm from center, whereas in the downward direction the temperature difference was  $7.82^{\circ}\text{C}$  at 10mm below the surface at the center. This indicates that the vertical position was a lot more sensitive to error due to incorrect placement of the thermocouple. The relative error for these positional errors are 0.2% and 2.0%, respectively. The larger value attributed to the error in depth measurement was used to determine the final thermocouple error.

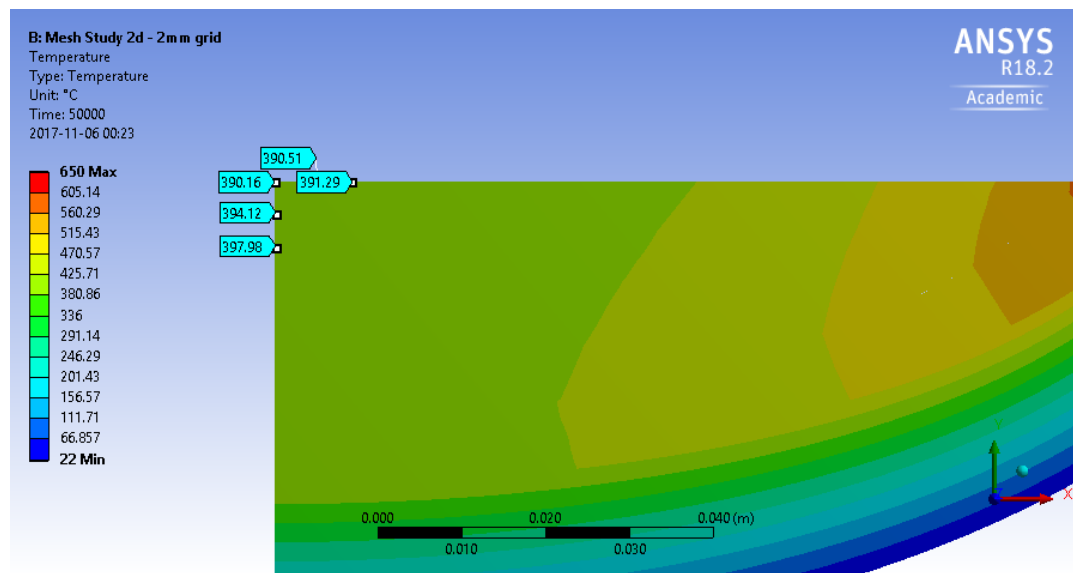


Figure 50: Surface and depth temperature gradient used for positional error estimate for thermocouples, from simulated temperature distribution.

Deterioration due to corrosion of the thermocouple during use also introduces a source of error during transient measurements since a layer of corrosion increases the thermal resistance to the thermopile junction. The error associated with this process was estimated to be 1.5%. The combined temperature error was calculated to be 2.64% or 17.1°C when measuring a true temperature of 650°C.

#### 4.7 RECOMMENDATIONS FOR THERMOLYSIS REACTOR DESIGN

Based on the simulations and experiments, there are several notable features of the reactor which should be considered during a scaled-up design of the apparatus. The presented thermolysis reactor takes a long time to heat-up. This was seen in the thermal simulation and in the experimental data. The thermal conductivity of CuCl is approximately two orders of magnitude smaller than stainless steel. One approach to decrease heat up time is to increase the contact area of the heating surfaces relative to the volume of CuCl by incorporating heating coils internal to the reactor or modifying the aspect ratio to reduce the thermal resistance of the CuCl.

Maintaining the hydrolysis temperature of  $\text{CuO} \cdot \text{CuCl}_2$  whilst it is in transit may also help. This reduces the overall thermal load on the system and improves system efficiency. Some heating of the  $\text{CuO} \cdot \text{CuCl}_2$  will occur as it falls through the reactor and passes through the hot vapor.

The formation of crystals on the interior surface of the phase separation section indicates a need to heat the internal surfaces. Otherwise, a vapor convection current will continuously condense on the walls. The effect of vapor scaling is seen in Figure 51. Surfaces within the vapor separation section and the gas thermocouple had a crystalline deposit 1 to 4 mm thick.



Figure 51: Phase separator interior scaling.

Tubing and other devices downstream of the reactor needed to transport gas species to other filtration devices will also require heating to avoid scaling and clogging. Scaling within tubing is more troublesome than in the reactor because clogging can have catastrophic effects. However, scaling in the reactor can be managed by utilizing mechanical arms to break the surface growths and knock them back into the crucible.

An accumulation of  $\text{CuCl}$  in the reactor during normal operation is expected as  $\text{CuO} \cdot \text{CuCl}_2$  decomposes. For this set of tests, a tilting mechanism was used to transfer  $\text{CuCl}$  into the quench sell. However, during the transfer it was noted that the lateral speed of the molten stream was too high. A vertical pouring trajectory is needed to transfer material into the quench vessel. Therefore, a bottom dumping design should be implemented.

Finally, due to the temperature along the surface of the  $\text{CuCl}$  from the wall to the center of the reactor,  $\text{CuOCuCl}_2$  should settle near the perimeter to take

advantage of the higher heat. This effect was observed in simulations and experimental data.

#### 4.8 SUMMARY

Simulations showed that the thermolysis reactor had improved temperature rise with two heaters. Experiments with 2 types of salts were conducted and verified the simulations. Analysis of the crystalline buildup on the interior of the reactor showed nearly pure CuCl in a majority of the phase separator. The top lid of the phase separator, however, had a mixture of CuCl and  $\text{CuCl}_2 \cdot 2\text{H}_2\text{O}$ . Therefore, condensing the effluent vapors would be required in future operation to prevent fouling and clogging of tubing.

# CONCLUSION AND FUTURE

# 5

## WORK

### 5.1 CONCLUSION

Thermal simulations and experiments for the heat up of a thermolysis reactor were presented in this thesis. The data can be utilized to improve the design of the thermolysis reactor for pilot plant operation. The study of temperature distribution in the thermolysis reactor provided information regarding heater power requirements, and discussed the limitations in the heat-up rate of CuCl due to the surface convection rates.

Both experimental and simulated temperature data for a single heat source with CuCl showed that profiles had similar rates of temperature rise. In the simulations, it was shown that the surface temperatures were not adequate to sustain the decomposition of  $\text{CuO} \cdot \text{CuCl}_2$  for all rates of surface convection. This was confirmed by experiments, where the surface temperature was a maximum of  $446^\circ\text{C}$ . However, with dual heating sources and low surface convection rates (i.e. 1 and  $2 \text{ Wm}^{-2}\text{K}^{-1}$ ) the decomposition reaction will occur, because a surface temperature of  $538^\circ\text{C}$  was attained during experimentation.

Because  $\text{CuO} \cdot \text{CuCl}_2$  has a higher density compared to molten CuCl, granules are expected to sink into the molten bath and approach the heated surfaces. The temperature near the interior wall was also shown to be near the band

heater set point of 650°C. Therefore, depositing  $\text{CuO} \cdot \text{CuCl}_2$  near the walls rather than the center of the thermolysis reactor will supply the necessary thermal energy and minimize the heat conduction path. In this case, the centre of the crucible must remain above 430°C to keep the  $\text{CuCl}$  in a molten state. Reducing the heater set point temperature to 530°C prevents high rates of  $\text{CuCl}$  vapor from forming during heat up. The highest temperature of  $\text{CuCl}$  was observed at the salt-crucible wall. Simulations showed that the surface temperatures in the entire reactor would be adequate for decomposition once the set point was modified to 530°C with a low surface convection rate of  $1 \text{ Wm}^{-2}\text{K}^{-1}$ .

In the experiments, variations in the rate of temperature rise between solid and powdered  $\text{CuCl}$  were observed. The powdered  $\text{CuCl}$  had a faster heating rate, which was likely due to mixing of solids and liquids during the heating process. Solidified  $\text{CuCl}$ , on the other hand, melted at a slower rate. Ultimately, both approached a temperature of approximately 440°C. The simulations did not take into account phase change and, therefore, produced smooth heating curves.

The dual heater simulations and experiments showed that the experimental thermolysis reactor can decompose  $\text{CuO} \cdot \text{CuCl}_2$  at all simulated convection rates. The minimal temperature of 480°C was achieved after 175 minutes. The experimental data suggests that a surface convection rate between 2 and 4  $\text{Wm}^{-2}\text{K}^{-1}$  was present in the reactor.

Additional simulations were conducted with an increased mass of  $\text{CuCl}$ . They showed that the thermolysis reactor can sustain a production rate of 100 g of  $\text{H}_2$  per day, having 10.6 kg of solid reactants processed in 1 cycle with the utilized heater configuration.

The construction of the thermolysis reactor requires simplification, such that the tilting mechanism is replaced by a bottom dumping valve. The transfer into

the quench vessel would then be a downward transfer without imposing a longitudinal velocity on the falling CuCl.

To improve the efficiency of the reactor a phase separation section should be incorporated to prevent fouling of downstream piping and equipment. There were two domains of material present: CuCl crystals at the bottom and a mixture of predominantly CuCl<sub>2</sub> dihydrate and CuCl at the top. To reduce this accumulation of material the phase separator section should be heated to the melting point of CuCl, 430°C.

## 5.2 FUTURE WORK

Future work should examine sustainable rates of decomposition in this reactor with various capacities of CuCl. The obtained data showed that for small masses of CuO • CuCl<sub>2</sub> a molten salt bath ranging between 2.0 kg and 10.35 kg with dual heating source ensure decomposition to occur.

A slurry bubble column is capable of simulating the effects of gas released at the source. Common slurry bubble columns rely on a gas sparger nested at the base of the column and releasing a gas at a constant rate. A sparger at several depths in the slurry bubble column increases the gas volumetric flow rate as the bubbles travel upward. Additionally, a study of the inlet rate of CuO • CuCl<sub>2</sub> into the reactor will provide details regarding the depth at which the decomposition occurs.

Alternative thermolysis reactor designs should be studied to maximize thermal conduction into the salt and simultaneously minimizing the heat-up duration. Internal heating rods may be added to accelerate heating, while simultaneously reducing the temperature gradient between the heating sources and CuCl, which reduces vapor formation.

## APPENDIX 1 – PYTHON SOURCE CODE FOR TEMPERATURE CONTROLLER

The following excerpt Python script was written to interface with the RS-485 port on the SL4848-RR temperature controller, purchased at Automation Direct. The script will log the control temperature at the band heater and crucible interface and send commands for set point temperatures. The communication protocol relies on an RS-485 hardware layer and MODBUS-RTU software layer. Utilizing this scheme for data logging and set point modification is necessary for pilot-scale centralized controls. Ultimately, each stage of the process should operate autonomously without direct user interaction.

```

#####

This Python script locates devices connected to USB ports on host PC.

Tomasz Wajda
December 2016

#####

import sys
import glob
import minimalmodbus
# https://minimalmodbus.readthedocs.io/en/master/index.html

class ModbusCOMM():

    # initialize class
    def __init__(self):
        pass

    # find all usb devices connected to the computer
    def findPorts(self,slave, debug):
        # code snippet from
        # http://stackoverflow.com/questions/12090503/listing-available-com-ports-with-python

        if sys.platform.startswith('win'):
            ports = ['COM%s' % (i + 1) for i in range(256)]

        elif sys.platform.startswith('linux') or sys.platform.startswith('cygwin'):
            ports = glob.glob('/dev/tty[A-Za-z]*')

        elif sys.platform.startswith('darwin'):
            ports = glob.glob('/dev/tty.*')

        else:

```

```
raise EnvironmentError('Unsupported platform')

# print a list of all found ports
print('Ports Found:')
count = 1
for port in ports:
    print(count, port)
    count = count + 1

# determine which port to connect to
selectedPort = int(input('Connect to Port >> '))

# create serial port handle on selected port
# port setting are configured to default values on SL4848-R.R
try:
    self.instrument = minimalmodbus.Instrument(ports[selectedPort-1],slave)
    self.instrument.serial.baudrate = 9600
    self.instrument.serial.bytesize = 8
    self.instrument.serial.stopbits = 1
    self.instrument.serial.parity = minimalmodbus.serial.PARITY_EVEN
    self.instrument.serial.timeout = 1
    self.instrument.debug = debug

    print('\nConnected to:')
    print('Device: ' + ports[selectedPort-1])
    print('Slave: ', slave)

    if debug:
        print(self.instrument)

except OSError:
    print('\nCould not open port')
    exit()

# read register
def readRegister(self, register, decimals, disp):
    try:
        readValue = self.instrument.read_register(register,decimals)

        if disp == True:
            print(readValue)

        return readValue

    except IOError:
        readValue = -1000

        if disp == True:
            print('Cannot connect to slave')

        return readValue

# write to register
def writeRegister(self,register, value, decimals):
    self.instrument.write_register(register, value, decimals)
```

---

## REFERENCES

- [1] A. Ozbilen, I. Dincer and M. A. Rosen, "A comparative life cycle analysis of hydrogen production via thermochemical water splitting using a Cu-Cl cycle," *International Journal of Hydrogen Energy*, vol. 36, no. 17, pp. 11321-11327, 2011.
- [2] A. Odukoya and G. F. Naterer, "Upgrading waste heat from a cement plant for thermochemical hydrogen production," *International Journal of Hydrogen Energy*, vol. 39, no. 36, pp. 20898-20906, 2014.
- [3] M. A. Rosen, "Advances in hydrogen production by thermochemical water decomposition: A review," *Energy*, vol. 35, no. 2, pp. 1068-1076, 2010.
- [4] J. E. Sharpe and et al, "Modelling the potential of adsorbed hydrogen for use in aviation," *Microporous and Mesoporous Materials*, vol. 209, pp. 135-140, 2015.
- [5] S. Belz, "A synergetic use of hydrogen and fuel cells in human spaceflight power systems," *Acta Astronautica*, vol. 121, pp. 323-331, 2016.
- [6] "International Energy Outlook 2016," U.S. Energy Information Administration, Washington, DC, 2016.
- [7] O. A. Jianu, Z. Wang, M. A. Rosen and G. F. Naterer, "Experimental investigation of particle dissolution rates in aqueous solutions for hydrogen production," *Heat Mass Transfer*, vol. 52, no. 11, p. 2067–2073, 2015.
- [8] G. F. Naterer, S. Suppiah, L. Stolberg and et al., "Canada's program on nuclear hydrogen production and the thermochemical Cu-Cl cycle,"

- 
- International Journal of Hydrogen Energy*, vol. 35, no. 20, pp. 10905-10926, 2010.
- [9] G. F. Naterer, "Recent Canadian Advances in the Thermochemical Cu-Cl Cycle for Nuclear Hydrogen Production," in *Nuclear Production of Hydrogen*, Oakbrook, 2009.
- [10] S. Yalcin, "A Review of Nuclear Hydrogen Production," *International Association of Hydrogen Energy*, vol. 14, no. 8, pp. 551-561, 1989.
- [11] M. A. Lewis and J. G. Masin, "The evaluation of alternative thermochemical cycles – Part II: The down-selection process," *International Journal of Hydrogen Energy*, vol. 34, no. 9, pp. 4125-4135, 2009.
- [12] M. S. Ferrandon, M. A. Lewis and et al, "The Hybrid Cu-Cl Cycle: I. Conceptual Process Design and H<sub>2</sub>A Cost Analysis. II. Limiting the Formation of CuCl During Hydrolysis," in *NHA Annual Hydrogen Conference*, Sacramento, 2008.
- [13] F. Suleman, I. Dincer and M. Agelin-Chaab, "Environmental impact assessment and comparison of some hydrogen production options," *International Journal of Hydrogen Energy*, vol. 40, no. 21, pp. 6976-6987, 2015.
- [14] C. Acar and I. Dincer, "Impact assessment and efficiency evaluation of hydrogen production methods," *International Journal of Energy Research*, vol. 39, no. 13, pp. 1757-1768, 2015.
- [15] Z. Wang, "Thermal design of a solar hydrogen plant with a copper-chlorine cycle and molten salt energy storage," *international journal of hydrogen energy*, vol. 36, pp. 11258-11272, 2011.
-

- 
- [16] S. A. Grigoriev, V. I. Porembsky and V. N. Fateev, "Pure hydrogen production by PEM electrolysis for hydrogen energy," *International Journal of Hydrogen Energy*, vol. 31, no. 2, pp. 171-175, 2006.
- [17] V. N. Balshov and et al., "CuCl Electrolysis for Hydrogen Production in the Cu–Cl Thermochemical Cycle," *Journal of the Electrochemical Society*, vol. 158, no. 3, pp. 266-277, 2011.
- [18] D. D. Ebbing and S. D. Gammon, General Chemistry, 7th Edition ed., Boston: Houghton Mifflin Company, 2002.
- [19] M. S. Ferrandon, M. A. Lewis, F. Alvarex and E. Shafirovich, "Hydrolysis of CuCl<sub>2</sub> in the Cu–Cl thermochemical cycle for hydrogen production: Experimental studies using a spray reactor with an ultrasonic atomizer," *International Journal of Hydrogen Energy*, vol. 35, no. 5, p. 1895–1904, 2010.
- [20] M. S. Ferrandon, M. A. Lewis and et al, "Hydrogen production by the Cu–Cl thermochemical cycle: Investigation of the key step of hydrolysing CuCl<sub>2</sub> to Cu<sub>2</sub>OCl<sub>2</sub> and HCl using a spray reactor," *International Journal of Hydrogen Energy*, vol. 35, no. 3, pp. 992-1000, 2010.
- [21] A. F. Dalebrook, W. Gan, M. Grasemann, S. Moret and G. Laurency, "Hydrogen storage: beyond conventional methods," *Chemical Communication*, vol. 49, no. 78, pp. 8735-8751, 2013.
- [22] D. S. Pyle, E. Gray and C. J. Webb, "Hydrogen storage in carbon nanostructures via spillover," *International Journal of Hydrogen Energy*, vol. 41, no. 42, pp. 19098-19113, 2016.
- [23] J. Germain, J. M. Frechet and F. Svec, "Nanoporous Polymers for Hydrogen Storage," *Small*, vol. 5, no. 10, pp. 1098-1111, 2009.

- 
- [24] E. Masika and R. Mokaya, "Exceptional gravimetric and volumetric hydrogen storage for densified zeolite templated carbons with high mechanical stability," *Energy and Environmental Science*, vol. 7, no. 1, pp. 427-434, 2014.
- [25] J. Graetz, "New approaches to hydrogen storage," *Chemical Society Review*, vol. 38, no. 1, pp. 73-82, 2008.
- [26] M. Yaday and C. Xu, "Liquid-phase chemical hydrogen storage materials," *Energy and Environmental Science*, vol. 5, no. 12, pp. 9698-9725, 2012.
- [27] D. Mellmann, P. Sponholz, H. Junge and M. Beller, "Formic acid as a hydrogen storage material – development of homogeneous catalysts for selective hydrogen release," *Chemical Society Reviews*, vol. 45, no. 14, pp. 3954-3988, 2016.
- [28] G. D. Marin, "Kinetics and Transport Phenomena in the Chemical Decomposition of Copper Oxychloride in the Thermochemical Cu-Cl Cycle," University of Ontario Institute of Technology, Oshawa, 2012.
- [29] G. D. Marin, Z. Wang, G. F. Naterer and K. Gabriel, "X-ray diffraction study of multiphase reverse reaction with molten CuCl and oxygen," *Thermochimica Acta*, vol. 524, no. 102, pp. 109-116, 2011.
- [30] M. A. Lewis, M. S. Ferrandon, D. F. Tatterson and P. Mathias, "Evaluation of alternative thermochemical cycles – Part III further development of the Cu-Cl cycle," *International Journal of Hydrogen Energy*, vol. 34, pp. 4136-4145, 2009.
- [31] M. Serban, M. A. Lewis and J. K. Bosco, "Kinetic Study of the Hydrogen and Oxygen Production Reactions in the Copper-Chloride

- 
- Thermochemical Cycle," in *American Institute of Chemical Engineering*, New Orleans, 2004.
- [32] M. A. Lewis, J. G. Masin and R. B. Vilim, "Development of the Low Temperature Cu-Cl Thermochemical Cycle," in *International Congress on Advances in Nuclear Power Plants*, Seoul, 2005.
- [33] M. Abdulrahman, Z. Wang and G. Naterer, "Scale-up analysis of three-phase oxygen reactor in the Cu-Cl thermochemical cycle of hydrogen production," in *EIC Climate Change Technology Conference 2013*, 2013.
- [34] S. Ghandehariun, M. Talimi, M. Rosen and G. Naterer, "Analysis of the hazards for the molten cuprous chloride pouring operation in an industrial hydrogen production facility," *International Journal of Energy Research*, no. 37, pp. 358-369, 2013.
- [35] V. N. Daggupati, G. F. Naterer, K. S. Gabriel, R. J. Gravelsins and Z. L. Wang, "Equilibrium Conversion in Cu-Cl Cycle Multiphase Processes of Hydrogen Production," *Thermochimica Acta*, vol. 496, no. 1-2, pp. 117-123, 2009.
- [36] G. A. Slack and P. Andersson, "Pressure and temperature effects on the thermal conductivity of CuCl," *Physical Review B*, vol. 26, no. 4, pp. 1873-1884, 1982.
- [37] "Copper Chloride," Department of Chemistry, Moscow State University, 27 May 1996. [Online]. Available: <http://www.chem.msu.su/rus/tsiv/Cu/ivtan0018.html>. [Accessed 14 June 2017].

- 
- [38] Z. Wang, K. Gabriel and G. F. Naterer, "Multiphase reactor scale-up for Cu–Cl thermochemical hydrogen production," *International Journal of Hydrogen Energy*, vol. 33, no. 23, pp. 6934-6946, 2008.
- [39] G. Naterer, K. Gabriel, Z. Wang, V. Daggupati and R. Gravelins, "Thermochemical hydrogen production with a copper–chlorine cycle. I: oxygen release from copper oxychloride decomposition," *International Journal of Hydrogen Energy*, vol. 33, no. 20, p. 5439–5450, 2008.
- [40] G. F. Naterer, S. Suppiah and et al, "Clean hydrogen production with the Cu-Cl cycle - Progress of international consortium, I: Experimental unit operations," *International Journal of Hydrogen Energy*, vol. 36, no. 24, pp. 15472-15485, 2011.
- [41] M. Abdulrahman, Z. Wang, G. F. Naterer and M. Agelin-Chaab, "Thermohydraulics of a Thermolysis Reactor and Heat Exchangers in the Cu-Cl Cycle of Nuclear Hydrogen Production," 2013.
- [42] M. Abdulrahman, "Heat Transfer Analysis of a Multiphase Oxygen Reactor Heated by a Helical Tube in the Cu-Cl Cycle of a Hydrogen Production," *International Journal of Mechanical, Aerospace, Industrial, Mechatronic and Manufacturing Engineering*, vol. 10, no. 6, pp. 1018-1023, 2016.
- [43] S. Mostafa Ghiaasiaan, *Two-Phase Flow, Boiling and Condensation in Conventional and Miniature Systems*, Cambridge: Cambridge University Press, 2008.
- [44] H. A. Jakobsen, *Chemical Reactory Modeling: Multiphase Reactive Flows*, 2nd Edition ed., New York: Springer International Publishing, 2014.

- 
- [45] M. Abdulrahman, "Experimental Studies of the Transition Velocity in a Slurry Bubble Column at High Gas Temperature of a Helium-Water-Alumina System," *Experimental Thermal and Fluid Science*, vol. 74, pp. 404-410, 2016.
- [46] M. Abdulrahman, "Experimental Studies of Direct Contact Heat Transfer in a Slurry Bubble Column at High Gas Temperature of a Helium-Water-Alumina System," *Applied Thermal Engineering*, vol. 91, pp. 515-524, 2015.
- [47] C. Wu, M. H. Al-Dahhan and A. Prakash, "Heat Transfer Coefficients in a High-Pressure Bubble Column," *Chemical Science Engineering*, vol. 62, no. 1-2, pp. 140-147, 2007.
- [48] C. Wu and M. Al-Dahhan, "Heat Transfer Coefficients in Mimicked Fischer-Tropsch Slurry Bubble Columns," *Industrial and Engineering Chemistry Research*, vol. 51, no. 4, pp. 1543-1548, 2012.
- [49] D. Valerio and J. Sa da Costa, "Tuning of Fractional PID Controllers with Ziegler–Nichols-Type Rules," *Signal Processing*, vol. 86, no. 10, pp. 2771-2784, 2006.
- [50] Z. Wang and et al., "Multiphase reactor scale-up for Cu–Cl thermochemical hydrogen production," *International Journal of Hydrogen Energy*, vol. 33, no. 23, pp. 6934-6946, 2008.
- [51] M. Stewart and K. Arnold, *Gas-Liquid and Liquid-Liquid Separators*, Oxford: Gulf Professional Publishing, 2009.
- [52] J. M. Campbell, "Gas-Liquid Separators Sizing Parameters," 1 September 2015. [Online]. Available: <http://www.jmcampbell.com/tip-of-the>
-

- 
- month/2015/09/gas-liquid-separators-sizing-parameter/. [Accessed 26 June 2016].
- [53] V. M. Boiko, A. A. Pivovarov and S. V. Poplavski, " Measurement of Gas Velocity in a High-Gradient Flow, Based on Velocity of Tracer Particles," *Combustion, Explosion, and Shock Waves*, vol. 49, no. 5, pp. 548-554, 2013.
- [54] S. Chawla, "Materials Selection for Corrosion Control," ASM International, 1993.
- [55] K. Azarbayjani, "System for evaluating effects of immersion in molten copper chloride salts on corrosion resistant coatings.=", UOIT, Oshawa, 2014.
- [56] M. Donachie, Titanium: A Technical Guide, 2nd Edition ed., ASM International, 2000.
- [57] Cabot Corporation, "Corrosion Resistance of Hastelloy Alloys," Cabot Corporation, 1984.
- [58] O. Jaber, "Heat and Fluid Flow Analysis in a Molten CuCl Heat Exchanger," UOIT, Oshawa, 2009.
- [59] R. W. Lewis, P. Nithiarasu and K. N. Seetharamu, Fundamentals of the Finite Element Method for Heat and Fluid Flow, Chichester: John Wiley and Sons, 2004.
- [60] S. J. Kline and F. A. McClintock, "Describing Uncertainties in Single-Sample Experiments," *Mechanical Engineering*, vol. 75, pp. 3-8, Jan. 1953.

- 
- [61] J. G. Mason and M. A. Lewis, "Development of the Low Temperature Hybrid Cu-Cl Thermochemical Cycle," in *International Congress on Advances in Nuclear Power Plants*, Seoul, 2005.
- [62] K. Pope, Z. Wang and G. F. Naterer, "Process integration of material flows of copper chlorides in the thermochemical Cu-Cl cycle," *Chemical Engineering Research and Design*, vol. 109, pp. 273-281, 2016.
- [63] A. J. Magistro and J. A. Cowfer, "Oxychlorination of Ethylene," *Journal of Chemical Education*, vol. 63, no. 12, pp. 1056-1058, 1986.
- [64] M. W. Hisham and S. W. Benson, "Thermochemistry of the Deacon Process," *Journ of Physics Chemistry*, vol. 99, no. 16, pp. 6194-6198, 1995.
- [65] O. Jaber, G. F. Naterer and I. Dincer, "Heat recovery from molten CuCl in the Cu-Cl cycle of hydrogen production," *International Journal of Hydrogen Energy*, vol. 35, no. 12, pp. 6140-6151, 2010.